Radio measurements for determining the energy scale of cosmic rays

Zur Erlangung des akademischen Grades eines

Doktors der Naturwissenschaften

an der KIT-Fakultät für Physik des
Karlsruher Instituts für Technologie (KIT)

genehmigte

Dissertation

von

Dipl.-Phys. Roman Hiller

aus Moskau

Tag der mündlichen Prüfung: 05.02.2016

Referent: Prof. Dr. J. Blümer

Korreferent: Prof. Dr. M. Feindt

Betreuer: Dr. F. G. Schröder

Abstract

Radio measurements for determining the energy scale of cosmic rays

To this day, the energy of cosmic rays by far surpasses that achieved by human-made particle accelerators. Since the discovery of cosmic rays in the beginning of the 20th century, research in this field lead to the understanding of many processes in the universe as well as particle physics in general. However, their origin is still largely unknown, especially at the highest energies. Above 10^{14} eV, the cosmic-ray flux is too low to be measured directly, and instead must be reconstructed from air showers induced in the atmosphere, using large, ground based detectors.

A comparatively new detection method for air showers is the radio technique: mainly due to geomagnetic deflection, charged particles emit a radio pulse, which can be detected with an antenna array. Arrival direction, energy and primary particle type of the air shower can be reconstructed from radio measurements. In particular, the energy can be measured straightforwardly via the radio pulse height. The radio signal in principle provides an absolute scale for the energy measurement, but so far the understanding and measurement of the signal has limited the practical application of this feature. This work resolves these limitations in the context of the Tunka Radio Extension (Tunka-Rex).

Tunka-Rex is an array of 25 antennas with a spacing of roughly 200 m close to Lake Baikal, Russia. Together with its host experiment, the air-Cherenkov detector Tunka-133, it measures air showers from cosmic rays with an energy of around 10^{17} eV.

Within the present work, an absolute calibration of Tunka-Rex for the reconstruction of the radio amplitude was performed, combining laboratory measurements of the electronics in the signal chain, a calibration of the full antenna station with a reference source, and detailed simulations of the antenna response. In a collaborative effort, the antenna stations of the radio experiments LOPES and LOFAR were also calibrated using a similar method. This was done using the same reference source, which resulted in a consistent and absolute amplitude scale for all three experiments.

Exploiting the absolute calibration and developing methods to use the radio detection method more efficiently, the following main results were obtained:

- A reconstruction method for the air-shower energy with a single antenna station was developed. With a precision of at least 25%, it maximizes the detector efficiency, and thereby triples the event statistics.
- Measured radio-signal amplitudes were compared with model calculations of the CoREAS simulation code. Agreement was found within uncertainties of 17%, which confirms the amplitude scale of CoREAS.
- With results from Tunka-Rex and LOPES, it was shown that the energy scales of the host experiments, Tunka-133 and KASCADE-Grande, respectively, are consistent to an accuracy of 10%. Thus, it was demonstrated that calibrated radio measurements can be used to compare energy scales of air-shower experiments.

Zusammenfassung

Bestimmung der Energieskala kosmischer Strahlung durch Radiomessungen

Bis zum heutigen Tag überragt die Energie der Teilchen kosmischer Strahlung die von Teilchenbeschleunigern bei weitem, und ihre Erforschung hat das Verständnis des Universums und der Teilchenphysik stets vorangetrieben. Ihr Ursprung ist jedoch vor allem bei den höchsten Energien unbekannt. Über 10^{14} eV ist ihr Fluss so niedrig, dass eine Messung nur noch durch großflächige Detektoren auf der Erdoberfläche möglich ist. Diese weisen Luftschauer nach, Kaskaden von Sekundärteilchen in der Atmosphäre.

Eine neue Methode zur Messung von Luftschauern ist der Radionachweis: Hauptsächlich durch die Ablenkung geladener Teilchen des Luftschauers im Erdmagnetfeld werden Radiopulse emittiert, die mit Antennen nachgewiesen werden können. Richtung, Energie und Art des Primärteilchens, das den Luftschauer ausgelöst hat, können durch Radiomessungen rekonstruiert werden. Insbesondere die Energie kann direkt über die Pulshöhe bestimmt werden. Das Radiosignal bietet dafür eine absolute Energieskala, was durch Defizite in Verständnis und Messung des Signals bisher allerdings nicht ausgenutzt werden konnte. Die vorliegende Arbeit löst dieses Problem mit Hilfe von Tunka-Rex.

Tunka-Rex ist ein Radiodetektor für Luftschauer nahe des Baikalsees in Russland, der aus 25 Antennen im Abstand von 200 m besteht. Als Erweiterung von Tunka-133, einem Luft-Cherenkov-Detektor, ergänzt es diesen im Energiebereich ab 10^{17} eV.

In der vorliegenden Arbeit wird Tunka-Rex kalibriert und damit die Rekonstruktion des Radiosignals ermöglicht. Dazu wurden Labormessungen der Elektronik mit einer Antennenkalibration und Simulationen der genauen Richtcharakteristik kombiniert. In Zusammenarbeit mit den LOPES- und LOFAR-Experimenten wurden auch diese mit einer ähnlichen Methode und der gleichen Referenzquelle kalibriert, weshalb die Amplitudenskalen der Experimente nun konsistent sind. Die Kalibration und die Entwicklung von Methoden zur effizienten Nutzung der Radiomethode ermöglichte folgende Hauptresultate:

- Es wurde eine neue Methode zur Rekonstruktion der Luftschauerenergie aus Einzel-Antennen-Messungen entwickelt. Mit dieser wird eine Genauigkeit von mindestens 25% erreicht und die Effizienz maximiert, wodurch die Ereignisstatistik verdreifacht wurde.

- Gemessene Radioamplituden wurden mit Modellrechnungen des Simulationsprogramms CoREAS verglichen. Sie stimmen innerhalb der Unsicherheiten von 17% überein, was die Amplitudenskala von CoREAS bestätigt.

- Durch Vergleich der Messungen der Radioerweiterungen Tunka-Rex und LOPES wurde mit einer Genauigkeit von 10% festgestellt, dass die Energieskalen der Hauptexperimente, Tunka-133 und KASCADE-Grande, übereinstimmen. Somit wurde demonstriert, dass sich kalibrierte Radiomessungen zum Vergleich der Energieskalen von Luftschauerexperimenten eignen.

Contents

1 Introduction

Cosmic rays are energetic particles from space, which have fascinated scientists from all over the world for over a century. The discovery of cosmic rays at the beginning of the 20th century suddenly pushed the high-energy frontier of particle physics forward by orders of magnitude, leading to the discovery of many elementary particles. Simultaneously, it raised the question: what process is able to accelerate particles to the tremendous energies observed in cosmic rays? And for the highest energies, which extend up to 10^{20} eV, this questions remains open.

Measurements bearing the answer to this question are challenging. The low cosmic-ray flux above about 10^{14} eV makes direct measurements with particle detectors practically impossible. However, at these energies, cosmic rays induce air showers in the atmosphere. These cascades of secondary particles can extend to ground level where they may be measured using huge, sparse arrays of detectors.

There are multiple techniques of how to detect an air shower, which can be categorized into two classes: detectors for secondary particles and detectors for different types of light, such as fluorescence or air-Cherenkov. Measurements with particle detectors are usually limited by systematic uncertainties, often due to model dependence, and light detectors are limited in their duty cycle, because they can only operate during clear, moonless nights. Contemporary cosmic-ray observatories often combine multiple detector types to capitalize on their respective advantages.

An alternative technique is currently increasing in prominence: the radio detection combines advantages from particle and light detectors. Mainly due to the geomagnetic deflection of secondary particles, an electromagnetic signal in the MHz range is emitted in the forward direction of the air shower. This can be measured with an array of antennas, an economic device with full duty cycle. Latest results also exhibit a competitive precision in the measurement of air-shower parameters, i.e., direction, energy and position of the shower maximum. Furthermore, the measurement can, in principle, provide an absolute energy scale, which enables cross-calibration of different experiments. So far, the realization of this possibility has been hindered by lacking theoretical understanding of the radio signal and contradicting measurements. Additionally, air-shower signals are barely above the background close to the threshold of around 10^{17} eV, where all current radio detectors operate. This affects efficiency, which counters many of the advantages. The aim of this work was to resolve these issues in the framework of Tunka-Rex, the Tunka Radio Extension.

Tunka-Rex is a radio detector in Siberia, Russia. It is an array of 25 radio antennas, distributed over 3 km^2. Starting from 2012, it measured the radio signal of cosmic-ray air showers with energies around 10^{17} eV. Tunka-Rex is co-located with Tunka-133, an air-Cherenkov detector for air showers with energies between 10^{15} eV and 10^{18} eV. Tunka-133, as the host experiment of Tunka-Rex, provides a trigger, infrastructure and an independent, established reconstruction of air-shower parameters, which serve as a benchmark for Tunka-Rex. The goal of Tunka-Rex is to demonstrate the practical use of a radio detector and develop methods and concepts for future devices.

In context of this work, Tunka-Rex was deployed and its instrumental properties have been studied. In particular, a calibration was performed for the reconstruction of the absolute signal amplitude with Tunka-Rex. This was done by combining laboratory measurements of electronics, an antenna calibration with a reference source and antenna simulations. In particular, the calibration with the reference source is a very sensitive endeavor and proved to be challenging in the past. For Tunka-Rex, the reference source of the LOPES experiment was used, which lead to an update of the LOPES calibration in the process. This resolved a discrepancy between air-shower simulations of the radio emission and LOPES measurements [1]. Moreover, the same reference source was also used to calibrate the LOFAR experiment [2]. Thus, these three experiments have a consistent calibration scale, which might become a standard for other experiments.

To give a basis for air-shower measurements with Tunka-Rex, a standard reconstruction method was developed. Data of the first two measurement seasons were analyzed, which provided a benchmark for all analysis in this work and for Tunka-Rex in general. Using results of the standard reconstruction, the direction-dependent efficiency and energy threshold were modeled. Besides showing limitations and capabilities of the standard analysis, the model can be used for predictions of performance on other analyses or detector setups.

With these prerequisites three questions have been investigated, which are connected to the amplitude scale of the radio signal:

- Is it possible to reconstruct the air-shower energy with a single antenna station? In its current status, one of the main benefits of a radio detector, the full duty cycle, is almost nullified around 10^{17} eV, due to low efficiency. It is studied, how the efficiency can be increased by releasing the standard requirement for 3 antennas with signal, when using information from the host experiment.

- What is the correct amplitude scale of the radio signal from air showers and how well is it described theoretically? The amplitude scale of the radio signal from model calculations and measurements was ambiguous so far. With measurements from Tunka-Rex, the amplitude scale is determined and compared to air shower simulations. The result is checked by the consistently calibrated LOPES experiment.

- Is it possible to use the radio technique to compare the energy scales of different air-shower experiments? The progressing understanding of theoretical and instrumental aspects of the radio technique enables a precise and accurate measurement of the absolute energy scale for its host experiment. On the example of Tunka-133 and KASCADE-Grande, it is demonstrated, how radio measurements can be used for a direct comparison of independently calibrated energy scales.

The structure of this work is as follows: In chapter 2, an overview about the research field of cosmic rays is given, and in chapter 3, the status of air-shower detection with the radio technique is summarized. After an introduction of the Tunka detector complex in chapter 4, the calibration of the Tunka-Rex antenna and signal chain is described in chapter 5. In chapter 6, the standard reconstruction method of Tunka-Rex is defined and a model for energy thresholds and efficiency is developed. Chapter 7 starts with presenting a method for the reconstruction of the air-shower energy with a single antenna station. Then, amplitudes from air-shower measurements with Tunka-Rex are compared on an absolute scale with CoREAS simulations for the radio emission from air showers. Finally, the energy scales of Tunka-133 and KASCADE-Grande are compared to each other based on measurements of their radio extensions Tunka-Rex and LOPES, respectively. The results are concluded in chapter 8.

2 Cosmic rays

Cosmic rays are highly energetic particles, originating in the depths of space, with energies ranging from 10^9 eV to at least 10^{20} eV. They consist mainly of atomic nuclei, with small contributions from other particles, like electrons and gamma rays. Cosmic rays were discovered by V. Hess in a series of balloon flights in 1911 and 1912 [3]. He was the first to correctly conclude the existence of an extraterrestrial radiation and excluded the sun as the origin. This earned V. Hess a Nobel Price in 1936, acknowledging the importance of the discovery.

Several balloon-borne and satellite-borne experiments were performed to measure the spectrum and mass composition of cosmic rays up to 10^{14} eV [4]. However, beyond this energy the cosmic-ray flux is so low that direct measurements become unfeasible. A solution was found in 1937 [5]. He found coincidences between events of high-energy particles over distances of several 100 m. These were caused by primary cosmic-ray particles, initiating extensive air showers of secondary particles after interacting in the atmosphere. This discovery enabled the extension of measurements up to an energy of at least 10^{20} eV, with huge air-shower detectors on the Earth's surface, observing areas of up to thousands of square kilometers [6].

Still, these air-shower measurements are challenging. Their interpretation is mostly limited by systematic uncertainties of hadronic interaction models, and at the highest energies additionally by low statistics. Thus, many questions, especially regarding the origin of cosmic rays remain unresolved.

In this chapter an overview is given about the most important facts, open problems and the current status in the field of high-energy cosmic rays. The latest results of the two most important characteristics of cosmic rays are summarized: their energy spectrum and mass composition. Then, some basic considerations to cosmic-ray sources are given, followed by an introduction to air-shower physics and measurements.

2.1 Energy spectrum

The energy spectrum of cosmic rays describes the particle flux as a function of energy. In Fig. 2.1, it is shown for high energies above 10^{14} eV. The cosmic-ray spectrum measured at Earth depends on propagation, the sources and acceleration mechanisms. Starting from 10^9 eV, below which solar particles dominate the flux, the energy spectrum reaches up to at least several times 10^{20} eV, where even the biggest detectors currently run out of statistics [9, 10]. Thus, the cosmic-ray energy spectrum covers at least 11 orders of magnitude in energy and 32 orders in flux. Therefore, the full spectrum cannot be

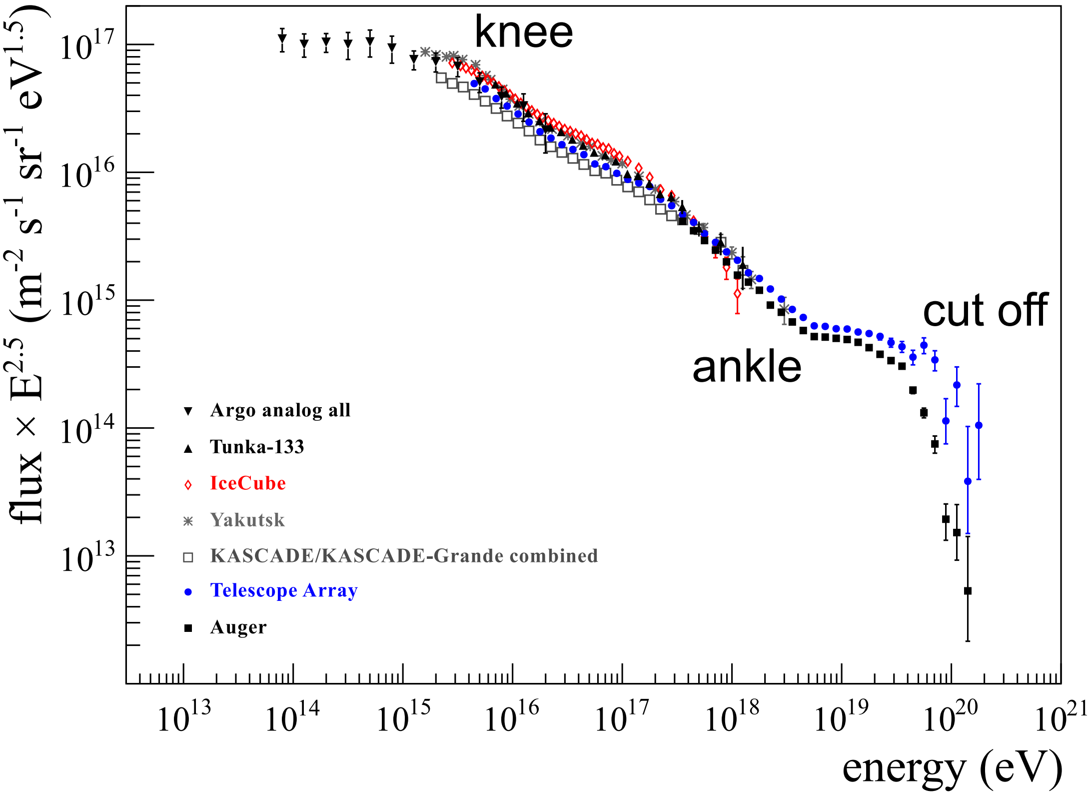

Figure 2.1: Energy spectrum of cosmic rays at energies above 10^{14} eV, measured by different experiments. The flux is multiplied by $E^{2.5}$, to enhance changes in slope. Features like the knee, the ankle and the high-energy cut off are undoubtedly established. Fig. adapted from Ref. [7] and [8].

measured with a single device, but has to be combined from measurements of different experiments, specialized on different energy ranges.

For energies up to about 10^{14} eV, satellite and balloon-borne particle detectors can measure the particle flux directly. Above this energy, it drops below the economical limit of these experiments. The measurements can be extended to higher energies with air-shower detectors on the Earth's surface. The detection techniques are discussed in Sec. 2.5.

Over the whole energy range, the spectrum can be described by a power law with slight brakes at certain points, where the spectral index γ changes slightly. Thus, the particle number N at energy E, in the observed solid angle Ω, area A and time t, is

$$\frac{\mathrm{d}^4 N}{\mathrm{d}E\ \mathrm{d}\Omega\ \mathrm{d}A\ \mathrm{d}t} \propto E^{-\gamma}. \tag{2.1}$$

Up to about $10^{15.5}$ eV the spectral index is $\gamma = 2.7$, and towards higher energies it changes to $\gamma = 3.1$. This feature is known as "the knee" and according to the common paradigm it originates from the maximum energy for light nuclei of the dominant source type in the Milky Way. As expected for an electromagnetic acceleration mechanisms, similar features were found at higher energies for heavier nuclei, when dividing the spectrum in mass groups [11, 12].

Around 10^{17} eV, at least one second slight kink occurs, corresponding to a change in spectral slope from 3.1 to $\gamma = 3.3$. This feature, sometimes called the "second knee", is reported by different experiments in the range of 1 to $3{\cdot}10^{17}$ eV [13, 8, 12]. The KASCADE-Grande collaboration investigated the features of mass groups around 10^{17} eV and found a decline in the heavy cosmic-ray component, the "heavy knee". This causes a steepening of the all-particle spectrum at this energy, and fits to a rigidity dependent threshold of the dominant source type at the knee. Due to the spread in reported energies, it is currently not clear if the "heavy knee" and the "second knee" are two distinct features, or if they are the same and the difference between the experiments originates in different energy scales. A comparison of energy scales with independent measurements could answer this question, e.g., using the radio technique, as performed in Sec. 7.3 for Tunka-133 and KASCADE-Grande.

At about $10^{18.6}$ eV the spectral slope makes another change from 3.3 back to 2.7 [9, 10]. This feature is called "the ankle" and its origin is still uncertain.

Above $10^{19.4}$ eV, the spectrum starts to decline rapidly below the sensitivity of current devices at around 10^{20} eV [9]. On the one hand, the reason for the decline could be a propagation effect: protons above $6 \cdot 10^{19}$ eV interact with photons of the cosmic microwave background, emitting pions via a Δ^{+}-resonance [14, 15]. Thus, the mean free path of the protons declines and far sources are not visible anymore above the threshold energy. For heavier nuclei, photodisintegration causes a similar effect [16]. On the other hand, the cut-off could indicate the maximum energy of the sources [17]. Without a reliable measurement of the mass composition versus energy this question cannot be unambiguously answered. This is one of the biggest challenges of current cosmic-ray experiments.

2.2 Mass composition

The mass composition of cosmic rays is another characteristic parameter, used to distinguish and test models for sources and propagation. For example the time scales of cosmic-ray propagation in the galaxy can be deduced from detailed measurements of the mass composition [21]. The measurement of the mass composition, especially at high energies, turns out to be very challenging and remains a field of active research.

Below 10^{14} eV, where fluxes are still high enough for direct measurements, the mass of the cosmic-ray particles can be determined straight forwardly. In Fig. 2.2, the results of such measurements are shown for several experiments. The distribution of elements roughly follows the one observed in the solar system. The elements H and He dominate the mass composition. With roughly 2-3 orders of magnitude lower abundances,

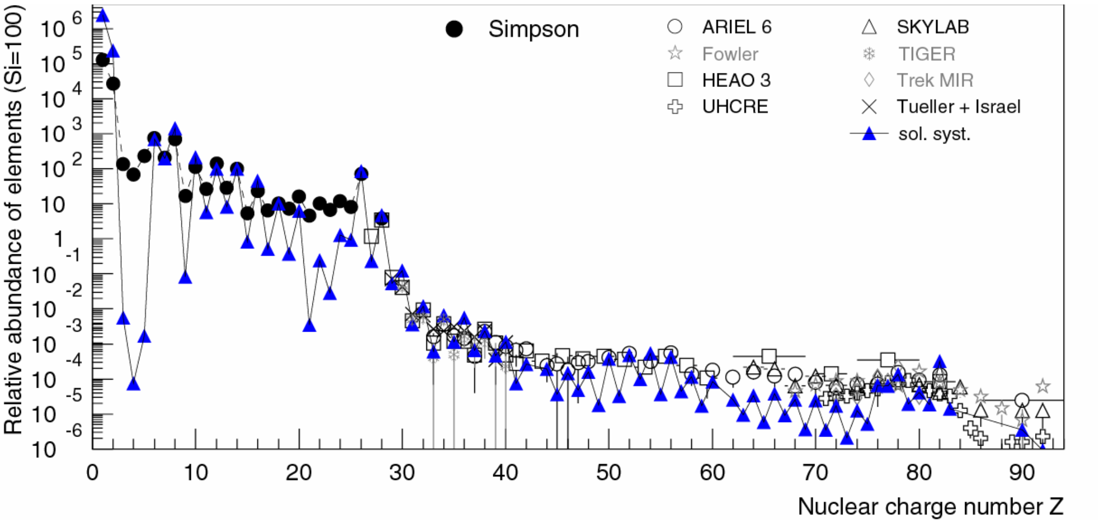

Figure 2.2: Abundances of nuclei in low-energy cosmic rays (around 10 GeV) and abundances in the solar system, normalized to the silicon abundance. As in the solar system, the abundance is dominated by H and He and at high charge numbers, above Si, by Fe. Fig. from Ref. [18]

elements up to nickel, originating from star burning are found. Abundances towards even heavier elements quickly decline by several orders of magnitude. Higher deviations to the solar distribution, e.g. for Li, Be and B can be explained by spallation reactions of the abundant C, O and Fe during propagation [18]. A detailed study of the precise relative abundances indicates a primary distribution, as expected in heavy stars of the OB spectral classes [22]. This suggests a significant contribution to galactic cosmic rays from the frequent supernovae from these short lived stars, and supports supernovae as a substantial contributor to galactic cosmic rays.

Above 10^{14} eV, a direct measurement is no longer feasible, therefore also the primary mass has to be reconstructed from air shower measurements. The most prominent choices of parameters are introduced in Sec. 2.4. The calibration is often performed via Monte Carlo simulations, which generally introduce a model dependence. Especially, if the processes simulated are beyond the limits of particle accelerator experiments, the hadronic interaction model is usually the biggest source of systematic uncertainty and limits the determination of the primary mass.

Furthermore, the separation of different primary masses in air-shower measurements is usually not high enough to determine the primary mass on a shower-to-shower basis. Instead, it is determined statistically, e.g., in terms of a mean mass or mean logarithmic mass. To evaluate these measurements, model calculations for proton and iron primaries are often used for comparison. Iron has the highest binding energy per nucleon of all elements, and therefore dominates abundances among the heavy elements. Thus, proton

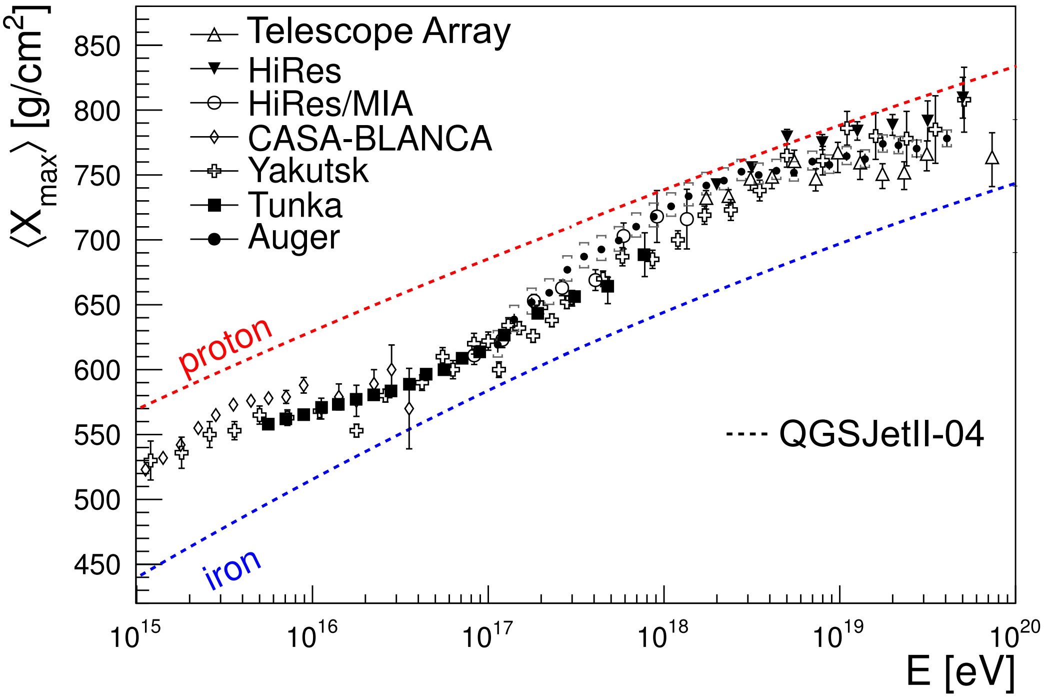

Figure 2.3: Mean depth of the shower maximum $X_{\rm max}$, versus energy E, measured by different air-shower experiments, and in comparison air shower simulations with the hadronic interaction model QGSJetII-04 for proton and iron primaries. Fig. from Ref. [19], with updates from Refs. [7] and [20].

and iron mark the expected extremes for the dominating species.

One mass sensitive parameter is the depth of the shower maximum. In Fig. 2.3, the mean depth is shown, measured by multiple experiments over a large energy range and also simulations for proton and iron primaries. The composition around 10^{15} eV becomes progressively heavier until 10^{17} eV and lighter again towards higher energies. This fits to the picture of the rigidity dependent maximum energy of the dominating source type around 10^{15} eV, with light elements fading out first. At 10^{17} eV possibly a new source type with predominantly light mass composition starts to dominate the cosmic-ray flux. This picture is also supported by measurements of the KASCADE-Grande experiment: in the same analysis, which revealed the heavy knee, a light cosmic-ray component with a comparatively hard energy spectrum was found to set in around 10^{17} eV [23].

At the highest energies, systematic uncertainties in both, measurements and models for air showers cause an ongoing dispute about the interpretation of data [24].

2.3 Sources of cosmic rays

The most straightforward way to find sources would be to point cosmic rays back to their origin. However, because cosmic rays are charged, they are deflected by interstellar and intergalactic magnetic fields. This turns out to be a key issue, because only at extremely high energies, above $10^{19.5}$ eV, protons may be able to traverse the Milky Way without significant deflection. Indications for a correlation between extragalactic source candidates and cosmic rays above this energy were found, but not confirmed yet [25].

Below these energies, sources have to be identified via modeling to measured data. The energies observed in cosmic rays are believed to be only attainable in a prolonged, cyclic process. The power-law shape of the energy spectrum can with very general assumptions be explained by stochastic acceleration. A process believed to offer sufficiently efficient energy gain is relativistic shock acceleration [26, 27].

With these basic assumptions already source candidates can be identified. To accelerate particles of charge Z to a maximum energy E_{max}, the combinations of size R, magnetic field strength B, and relativistic shock front speed $\beta = v/c$ of the object have to be sufficiently high [28]

$$E_{\mathrm{max}} = \frac{1}{2} \cdot 10^{18}\,\mathrm{eV} \cdot \beta Z \cdot \frac{R}{\mathrm{kpc}} \cdot \frac{B}{\mathrm{\mu}G}. \tag{2.2}$$

Galactic cosmic rays, up to at least 10^{15} eV, may originate from the shock fronts of supernova remnants. Supernova remnants have sufficient energy output and many other features, like the mass composition of cosmic rays at the lower energy end, are theoretically comprehensible with models of them [29, 30]. Furthermore, gamma-ray observations indicate supernova remnants to be acceleration sites [31].

Features of the spectrum and mass composition indicate the transition to another main type of source around 10^{17} eV. While there is no broadly accepted favorite, candidates can be compiled with Eq. 2.2, and common examples are neutron stars, active galactic nuclei or gamma ray bursts [18]. At the highest energies, at 10^{20} eV, even finding a plausible candidate becomes challenging.

2.4 Air showers

Air showers, used for ground based detection of cosmic rays, are caused by primary cosmic-ray particles hitting the atmosphere. Inelastic interactions produce secondary particles, which, if sufficiently energetic, continue to produce further particles. This process continues until the energy is dispersed so much that absorption in the atmosphere takes over and the particle number in the shower starts to decline again. Like in a calorimeter, the energy of the primary particle is at least partially deposited in the atmosphere.

Due to the high degree of complexity, often Monte Carlo simulations are used to model air showers. In the simulations interaction models are used, obtained from measurements

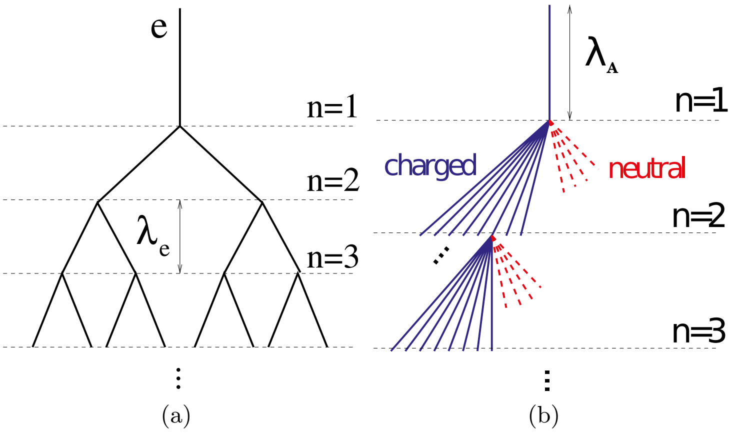

Figure 2.4: (a) Heitler model for electromagnetic cascades. After each interaction length λ_e the number of particles doubles via pair production and bremsstrahlung. (b) Extended Heitler model for hadronic cascades with the hadronic interaction length λ_A. Each interaction creates a pion jet. Neutral pions decay instantly into photons, feeding the electromagnetic cascade. Charged pions remain in the hadronic cascade until they decay into muons. Fig. from Ref. [32].

of experiments at particle accelerators. These interaction models are the main source of systematic uncertainty in air-shower modeling. Especially hadronic interactions are problematic, because they have have to be extrapolated from phenomenological descriptions to higher energies and the very forward phase space. The current limit of particle accelerators is a center-of-mass energy of $13{\cdot}10^{12}$ eV, which is reached for proton collisions by the Large Hadron Collider [33]. This is the same as the center-of-mass energy of 10^{17} eV cosmic-ray protons colliding with low-energy air particles.

To understand air showers, it is helpful to distinguish the electromagnetic, the hadronic and the muonic component. The electromagnetic component are the electrons, positrons and photons of the shower. Number-wise they dominate all other particles. Qualitatively, the electromagnetic component can be understood with the Heitler model [34], which is illustrated in Fig. 2.4. It describes the development of a electromagnetic cascade, taking only two processes into account: pair production and bremsstrahlung. According to the model, each process doubles the number of electromagnetic particles after one electromagnetic interaction length λ_e, dividing the primary energy equally among the particles. After n steps the particle number N_n and energy E_n per particle are

$$N_n = 2^n, \tag{2.3}$$

$$E_n = \frac{E_0}{N_n}. \tag{2.4}$$

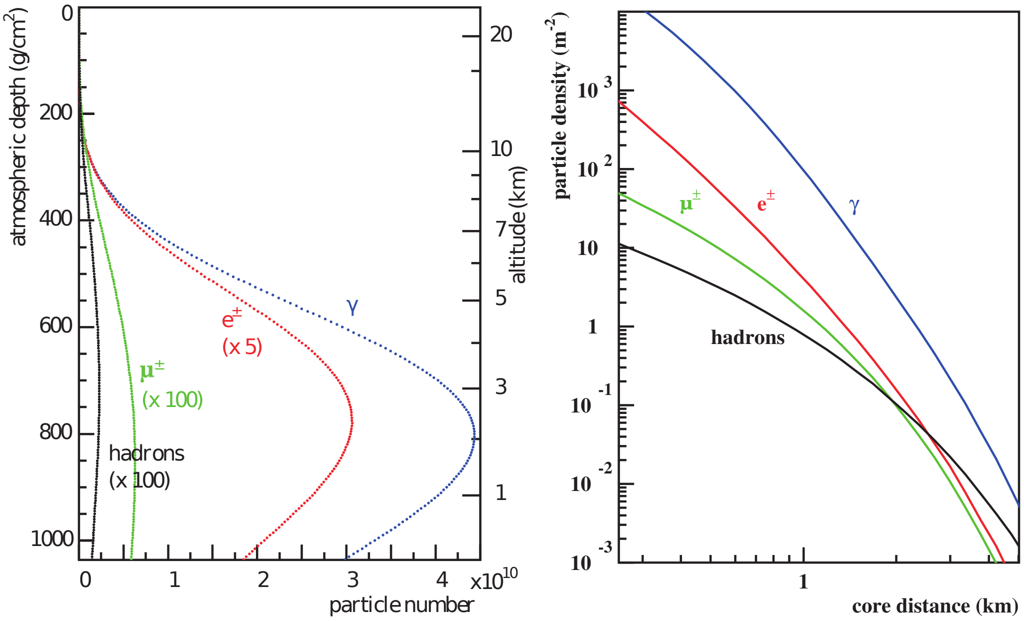

(a) (b)

Figure 2.5: (a) Longitudinal distribution of different components of a simulated air-shower, initiated by a proton with an energy of 10^{19} eV. The depth of the shower maximum is mostly determined by the electromagnetic component $(\gamma, e^{\pm})$. (b) The lateral distribution of particles shows a significant particle number even at distances of several km from the shower axis. Figs. from Ref. [32].

These processes continue until a critical energy E_{crit} is reached at which the interaction length becomes smaller than the absorption length. At that point the shower reaches its maximum and the particle number starts to decline exponentially. This results in a longitudinal profile, as shown in Fig. 2.5. The number of particles in the maximum is

$$N_{\mathrm{max}} = \frac{E_0}{E_{\mathrm{crit}}} = 2^{n_{\mathrm{max}}}. \tag{2.5}$$

With the interaction length λ_A, between a nucleus with mass number A and air, the atmospheric depth of the shower maximum X_{max} from the Heitler model is

$$X_{\mathrm{max}} = \lambda_A + \lambda_{\mathrm{e}} \cdot n_{\mathrm{max}} = \lambda_A + \frac{\lambda_{\mathrm{e}}}{\ln 2} \cdot \ln \frac{E_0}{E_{\mathrm{crit}}}. \tag{2.6}$$

The shower maximum is measured in terms of atmospheric depth, which is the path integrated density.

Due to the dominating number of electromagnetic particles N_{em}, the atmospheric depth of the shower maximum is very close the purely electromagnetic one. From the

Heitler model $N_{\mathrm{em}} \propto E_0$ is obtained, so the energy of the electromagnetic cascade can be reconstructed by measuring its particle number in the shower maximum.

The hadronic component consists primarily of n, p, π, ρ, and K. Although low in numbers, these particles play an important role for fueling the electromagnetic component and the production of muons in an air shower [17]. The hadronic component can qualitatively be understood with an extended Heitler model [35], also illustrated in Fig. 2.4. In this model, the hadronic cascade is comprised of pions. On each interaction, after one hadronic interaction length, the particle number is multiplied by the effective multiplicity k. As a simplification, one-third of the produced particles is assumed to be neutral pions π^0 and two-thirds are charged pions $\pi^{\pm}$, other hadrons are neglected. The neutral pions decay almost instantly with a lifetime of $8.52 \cdot 10^{-17}$ s, transferring energy from the hadronic to the electromagnetic component. The charged pions live 8 orders of magnitude longer, and therefore remain in the hadronic cascade for several generations of interactions. They decay into a muon and a muon neutrino when their energy falls beneath the critical energy, at which their decay length becomes smaller than their interaction length in the atmosphere. Therefore, the maximum number of muons N^{μ}_{max} is

$$N^{\mu}_{\mathrm{max}} = N^{\pi^{\pm}}_{\mathrm{max}} = \left(\frac{2}{3}k\right)^{n^{\mathrm{h}}_{\mathrm{max}}} \tag{2.7}$$

And the energy fed to the electromagnetic cascade is consequently

$$E_{\mathrm{em}} = \left[1 - \left(\frac{2}{3}\right)^{n^{\mathrm{h}}_{\mathrm{max}}}\right] \cdot E_0. \tag{2.8}$$

With a typical number of interaction generations n_{max} of 6, before decay, 90% of the energy in the hadronic cascade is transferred to the electromagnetic one [32].

According to the extended Heitler model, the muonic component is produced from the decay of charged pions into muons after reaching the maximum of the hadronic cascade. In real showers, there are multiple other processes producing muons. In recent years it was found that the muonic component is poorly described by current air-shower models [36]. One of the advantages of optical and radio measurements is their little sensitivity to the muonic component of the shower, avoiding this source of uncertainty.

Heavier nuclei can be implemented into the extended Heitler model with the superposition model: The binding energy of a nucleus, of several MeV per nucleon, is negligible against typical air shower energies. Therefore, a shower initiated by a nucleus with A nucleons can be modeled by A simultaneous proton showers with equally distributed energy E_A [32]

$$N^{\mathrm{max}}_{\mathrm{em}}(E, A) \approx A \cdot N^{\mathrm{max}}_{\mathrm{em}}(E_A, 1) = N^{\mathrm{max}}_{\mathrm{em}}(E, 1) \tag{2.9}$$

Thus, the maximum particle number of the electromagnetic component is mostly independent of the primary mass and can be used as an energy estimator for the primary particle. For muons, the model yields

$$N^{\mathrm{max}}_{\mu}(E, A) \approx A \cdot N^{\mathrm{max}}_{\mu}(E/A, 1) = A^{1-\alpha} \cdot N^{\mathrm{max}}_{\mu}(E, 1). \tag{2.10}$$

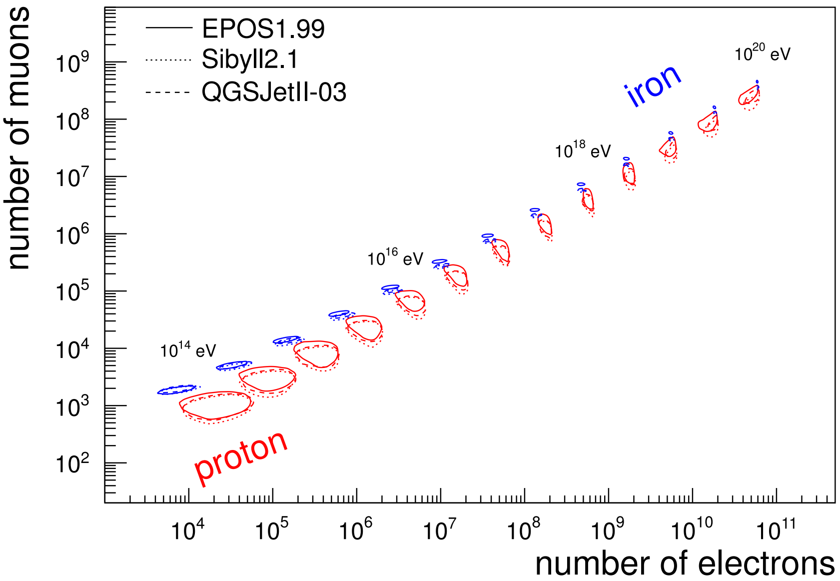

Figure 2.6: Number of muons versus number of electrons from Monte Carlo simulations of vertical air showers with different hadronic interaction models. The lines indicate 90% contours of the distributions for a fixed energy. The simulations are evaluated at an observation depth of 800 g cm^{-2}. Fig. from Ref. [19].

With $\alpha = 0.82...0.94$, the maximum number of muons can be used as an estimator for the primary mass [32]. Iron showers tend to have several 10% more muons than proton showers. Due to shower-to-shower fluctuations, the primary mass can only be determined statistically with this method.

While the equations only apply in the shower maximum, electron and muon numbers depend also during other parts of the shower development on energy and primary mass. In Fig. 2.6, the electron and muon number are shown for different energies at a constant observation depth.

Using particle detector arrays to measure electrons and muons individually, these dependencies can be used to reconstruct energy and mass of the primary particle. An accurately measured energy is imperative for properly interpreting the muon number as a mass estimator. Furthermore, air-shower simulations are usually used as a reference for interpreting the electron and muon numbers. This makes the method sensitive to the choice of the hadronic interaction model.

The depth of the shower maximum $X_{\max}$ as a function of the mass number A of the primary particle follows from Eq. 2.6 [32]:

$$X_{\max}(E, A) = \lambda_A(E, A) + \frac{\lambda_{\mathrm{em}}}{\ln 2} \cdot \ln \frac{E_0}{A \cdot E_{\mathrm{crit}}}. \tag{2.11}$$

For heavier nuclei, the first interaction takes place higher in the atmosphere, due to a larger inelastic nucleus-air cross section and due to the simultaneous development of several subshowers after the first interaction. Therefore, air showers initiated by heavier nuclei tend to have the shower maximum higher in the atmosphere and, due to averaging over several subshowers, feature lower fluctuations between different air showers [19].

With optical detection techniques, which have sensitivity to the longitudinal shower development, these dependencies of $X_{\max}$ can be used to reconstruct the primary mass statistically. Although to less extent than for the muon number, the proper interpretation of $X_{\max}$ requires an accurate energy measurement.

2.5 Detection of air showers

There are different detection techniques for air showers. The two general types of detectors are particle detector arrays and optical detectors. They measure either the lateral or the longitudinal profile of the air shower (see Fig. 2.5). A third type, the radio detection technique, regained popularity lately. It will be discussed individually in Ch.3. Contemporary cosmic-ray detectors often combine different techniques, to profit from their different advantages, like the Tunka detector complex, introduced in Ch.4.

2.5.1 Particle detector arrays

Since significant particle densities are still reached at ground level for energies above 10^{14} eV, sparse arrays of particle detectors can be used to detect the secondary particles of air showers directly. Experiments like Tunka-Grande [37], KASCADE-Grande [38], TIBET [39] and Telescope Array [40] use scintillator detectors to detect the light emission of ionizing particles traversing scintillating materials.

The second, popular choice of particle detectors are water-Cherenkov detectors: huge tanks with water, equipped with photo multipliers inside to detect the Cherenkov emission of traversing particles. Examples are Haverah Park [41], IceTop [42] and the surface detector of the Pierre Auger Observatory [43].

The stations of the devices are placed with a spacing ranging from 13 m at KASCADE, covering $200\,\mathrm{m} \times 200\,\mathrm{m}$ for energies between 10^{14} eV and 10^{16} eV [44], to 1.5 km spacing at the Pierre Auger Observatory [43], covering $50\,\mathrm{km} \times 70\,\mathrm{km}$ for $10^{18.5}$ eV to 10^{20} eV. To reach lower energies the detectors can be placed at high altitudes, like the recently deployed HAWC experiment at 4000 m height, which reaches down to 10^{12} eV [45].

The particle detector arrays usually come with the advantage of a full duty cycle, maximizing statistics, and are therefore best suited to measure the energy spectrum up to the highest energies. They reach energy resolutions of 20-30%, but often with model-dependent energy scales due to calibration procedures relying on air-shower simulations. For the reconstruction of the mass composition, these detector types struggle with systematic uncertainties due to strong model dependencies. The weaknesses can partially be overcome by combining particle detectors with other techniques, like optical or radio detectors, whose interpretation is less model dependent. This approach is followed by several experiments, like TAIGA, Telescope Array and the Pierre Auger Observatory [37, 46, 47].

2.5.2 Optical detectors

Optical detectors measure the electromagnetic emission of air showers close to the optical wavelength band. The two established principles are based on the detection of air-Cherenkov radiation or fluorescence light.

The refractive index of air, although small, causes air-shower particles to emit Cherenkov radiation. Due to its concentration in the forward direction, it can be detected already at energies as low as 10^{10} eV, which is used to detect the comparatively deep air showers from gamma rays. Imaging telescopes, like MAGIC and H.E.S.S. [48, 49], huge doublets and quadruplets of mirror telescopes, can detect the Cherenkov ring of air showers directly. Non-imaging types of Cherenkov detectors are sparse arrays of PMTs, detecting the coincident flash of UV light over an extended area, like Tunka-133 [8] or Yakutsk [50].

Above 10^{17} eV omnidirectional emitted fluorescence light can be detected. It is caused by the interaction of air-shower particles and nitrogen in the air. For these very high energies, mirror telescopes are used, similarly to the imaging Cherenkov telescopes. While Cherenkov telescopes are most sensitive when looking directly into the air shower, fluorescence telescopes aim to get a side view of the shower development. The number of particles from a portion of the longitudinal shower development is directly proportional to the intensity of the fluorescence emission, so the shower maximum can be directly observed after corrections for geometry and absorption. The Fly's Eye experiment [51], its continuation, HiRES [52], and the fluorescence detectors of the Telescope Array [53] and the Pierre Auger Observatory [54] use fluorescence detectors for air-shower measurements. Recently, the pathfinder missions TUS [55] and JEM-EUSO [56] are developed, to use satellite borne fluorescence telescopes in space for observing huge volumes of the atmosphere from above. If sufficiently low detection thresholds are reached, they can possibly detect the flux of cosmic rays beyond 10^{20} eV.

The advantage of the optical techniques is their good sensitivity to the depth of the shower maximum of 20-30 $\mathrm{g/cm^2}$ and a high energy precision of 10-15%. Their energy calibration is also less dependent on air-shower models than for particle detectors, because they are mainly sensitive to the electromagnetic component of the shower and can be calibrated absolutely with reference sources. Still, measurements at the highest energies with the two biggest experiments, the Pierre Auger Observatory and Telescope Array, both calibrated with fluorescence telescopes, indicate possible problems in the understanding of the energy scales [7]. The general disadvantages of optical techniques are their sensitivity to the atmospheric conditions and the low duty cycle, because they can only operate during clear, moonless nights.

The radio technique, introduced in Ch. 3, features many advantages of optical detectors, while being less sensitive to atmospheric conditions and having an almost full duty cycle.

3 The radio detection technique

Air-shower detection with the radio technique emerged as a research field in the 1960s [57]. Back then, both, theoretical concepts for radio emission from air showers [58, 59] and the experimental proof were accomplished [60]. After a burst in interest, the development of the technique was suddenly stopped, as it was realized that the analog technology at the time made the radio technique unpractical.

In the 2000s the field underwent a renaissance [61], initiated by two experiments, LOPES[62] and CODALEMA [63]. They proved the feasibility of the detection technique with the now cheaply available digital electronics and digital signal processing.

A third generation of experiments emerged from the success of its predecessors, with LOFAR [64], AERA [65] and Tunka-Rex [66]. They have to demonstrate the advantages and benefits of a radio detector for air showers in practice.

The advantages of the radio detection technique are its almost full duty cycle, with downtimes only during thunderstorms, in combination with sensitivity to the longitudinal shower development. Because the radio measurement is only sensitive to the electromagnetic shower component, like for optical techniques, systematic uncertainties from air shower models are smaller than for particle detector arrays. With the possibility of an absolute calibration, the radio technique can provide an absolute energy scale for air-shower measurements. Thus, it can potentially combine advantages of both, particle-detector arrays and optical techniques. Additionally, the radio signal in the MHz frequency range suffers very little attenuation in the atmosphere. Thus, it is well suited for the detection of very inclined air showers, providing information on the electromagnetic component, which is absorbed before reaching the ground.

This chapter begins with an introduction to the current theoretical understanding of radio emission from air showers. Then, an overview about the modeling of the radio signal is given. Finally, the detection in general and current experiments are discussed, to summarize the current status of the research field.

3.1 Emission mechanisms

The radio emission of an air shower can be described with the classical Maxwell equations [68, 69], given the distributions of charged particles and their time evolution. For its understanding it is useful to divide it into effective, comprehensible mechanisms. Currently two experimentally confirmed emission mechanism, illustrated in Fig. 3.1, were identified dominating the radio emission from air showers: geomagnetic deflection and the Askaryan effect. They both originate mostly from the electromagnetic component

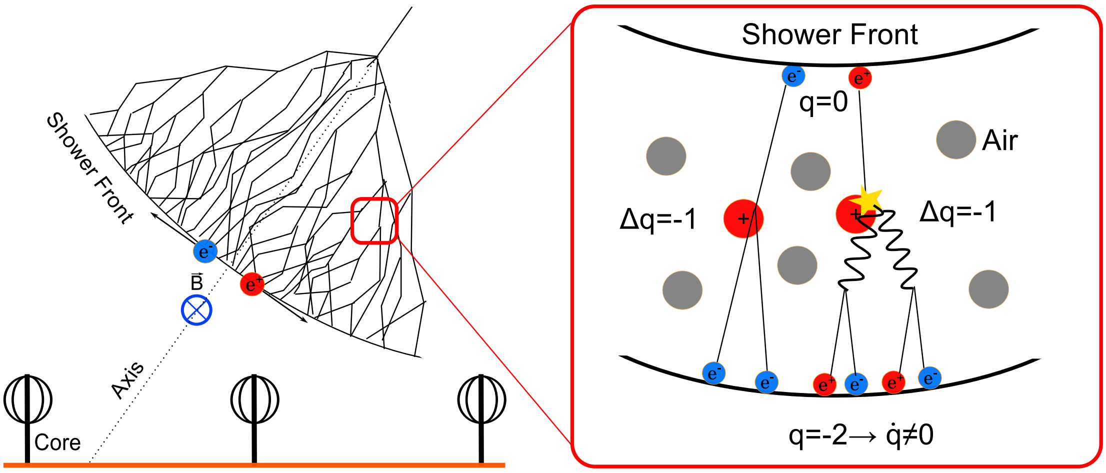

Figure 3.1: Emission mechanisms causing the radio signal from air showers. The dominant contributions originates from the geomagnetic deflection of charged particles and the resulting time-varying transverse currents. A smaller contribution arises due to a time-varying negative charge excess.

of the air shower, because it is the dominating contributor in terms of particle numbers and charge, and emission of the other components is additionally suppressed due to the higher mass of their particles. In most circumstances, except for showers almost parallel to the Earth's magnetic field, the main contribution of radio emission in air showers is of geomagnetic origin. The Earth's magnetic field deflects charged particles in the shower, inducing a transverse current [58]. As particle numbers vary over time, so does the current, emitting electromagnetic radiation in the process. The magnitude of the emitted radiation depends on the Lorentz force. Since particles move approximately in the direction of the shower axis, the magnitude of emitted radiation is proportional to $|\vec{v} \times \vec{B}|$, or $|\vec{B}| \cdot \sin\alpha$, with the angle α between the magnetic field $\vec{B}$ and the shower axis $\vec{v}$. The polarization of the radiation is aligned with the current, along $\vec{v} \times \vec{B}$, or the east-west axis, if projected on the ground.

A smaller contribution, typically in the order of 10% is induced by the Askaryan effect. Processes producing electrons and positrons during the air-shower development are asymmetric, because the air shower propagates through air, which contains only electrons. By ionizing air molecules and annihilation of positrons, the shower gains more negative than positive charge. This produces a charge excess varying in time, thereby causing an electromagnetic emission. This is known as Askaryan effect [59]. The polarization pattern of this second contribution is radial with respect to the shower axis. Contributions of both emission mechanisms with different polarization patterns add to a signal which is azimuthally asymmetric with respect to the shower axis.

Due to the thickness of the shower front of a few meters, broad band emissions of both mechanisms add up coherently in the MHz range. Consequently, the signal amplitudes

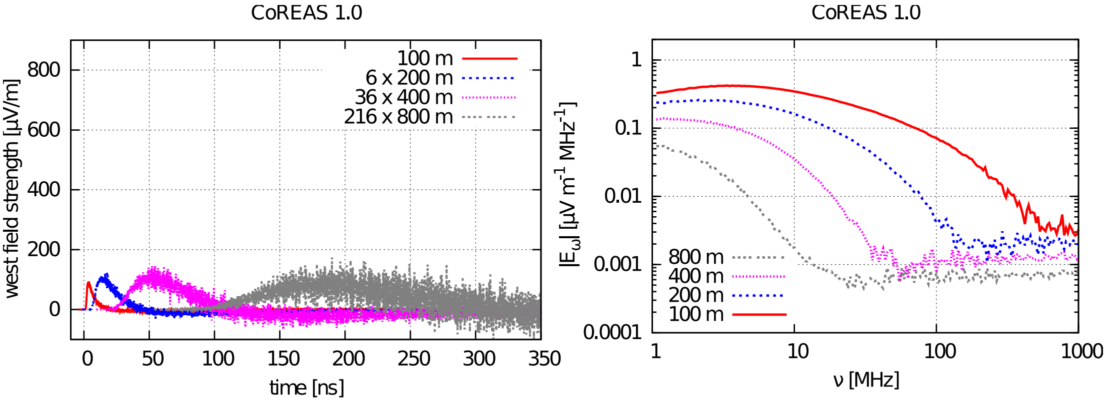

Figure 3.2: Radio signal and amplitude spectrum, simulated with the CoREAS simulation code for a 10^{17} eV vertical air-shower, induced by a proton. Magnetic field and observation depth were set to the Pierre Auger Observatory. Figs. from Ref. [67], the flattening at high frequencies is due to numerical noise in the simulation.

are roughly proportional to the particle number, and therefore also to the air shower energy. The resulting signal pulses have a width of several 10 ns. Simulated example signals and their spectra are depicted in Fig. 3.2

The small refractive index of air also has an impact on the radio signal on ground. As the air-shower front propagates faster than the speed of light in air, radiation from different stages of the air-shower development adds up coherently at different positions on ground. Although the emission is not caused by the Cherenkov effect itself, coherence conditions are similar. Thus, the refractive index leads to enhanced radiation close to the Cherenkov angle and the maximum of the signal is displaced from the shower axis towards the Cherenkov cone. With a Cherenkov angle for air showers of around 1°, the Cherenkov cone is typically located at a distance around 50 to 150 m to the shower core, depending on the distance to the shower maximum, which itself depends on observation depth and zenith angle. This becomes especially important at the higher frequencies, where coherence is only given at the Cherenkov angle. The experiments LOFAR [70], ANITA [71] and CROME [72] detected signals close to the Cherenkov cone at frequencies of up to 190 MHz, 900 MHz and 4.2 GHz, respectively.

3.2 Modeling of radio emission

To determine charge distributions, needed for the calculation of the radio emission with the Maxwell equations, Monte Carlo simulations of air showers are used, as in other fields of cosmic-ray research.

There are two different approaches how to treat the simulation output [67]: microscopic models, like end-point formalism and ZHS, which are implemented in CoREAS [73] and ZHAireS [69], respectively, calculate emission for individually simulated particles. Macroscopic models, like MGMR [74], which is implemented in EVA [75], determine the emission of effective currents. While the microscopic models determine the emission without introducing new parameters, they are usually more computationally intensive.

The simulation code used in this work is CoREAS. It is based on the end-point formalism, calculating emission at the beginning and end of particle tracks, as if they were accelerated and stopped suddenly [68]. Its predecessor, REAS 3.1 [76] used summarized simulation output from the CORSIKA [77] air-shower simulation code to calculate the radio emission. In its latest version, CoREAS, the calculation of the radio emission is directly implemented in the CORSIKA code.

Although the radio models in general converged during the last decade [67], big changes are common even in the latest updates. For example the update from REAS 3.1 to CoREAS changed predicted amplitudes by a factor of two. And measurements from two calibrated experiments, LOPES and AERA, gave contradicting results on which of the two predictions is right [78, 79]. This contradiction was solved in the context of this work, by revising the calibration of LOPES (see Sec. 5.6) and by adding a measurement from Tunka-Rex (see Sec. 7.2), now uniformly confirming the amplitude scale predicted by CoREAS [1]. Because comparisons of the models are regularly performed, it can be used as a benchmark for other models as well.

3.3 Radio detection of air showers

The radio emission from air showers can be detected using antenna arrays. The signature of the signal is a coincident radio pulses in multiple antennas, usually together with an event in an independently operating air-shower detector.

The detection threshold for a radio measurement in the 30-80 MHz band is ultimately limited by galactic noise. Galactic background and anthropogenic contributions to noise are shown in Fig. 3.3. Typical detection thresholds for signal amplitudes are 60 to 100 μV/m, corresponding to an energy threshold of about 10^{17} eV. A simulated radio signal footprint for a 10^{17} eV air shower is depicted in Fig. 3.4. Sec. 6.4 is dedicated to determine detection thresholds for Tunka-Rex.

The first two generations of radio experiments deployed arrays onto existing air-shower detectors to prove the principle of radio detection and develop a trigger. In the mean time it became clear, that at least close to the detection threshold, a trigger based on radio measurements alone is very challenging. Thus, radio experiments so far are mostly triggered by host or auxiliary air-shower detectors.

Radio experiments established and confirmed the picture of radio emission from air showers explained in the last sections: the first generation of radio experiments, in the 1960s, proved the dominant emission mechanism to be of geomagnetic origin, by finding the expected dependence of the signal strength on the geomagnetic angle α, and by measuring a predominantly east-west aligned polarization pattern [57]. This was confirmed by all following experiments, including Tunka-Rex. The newer radio detectors,

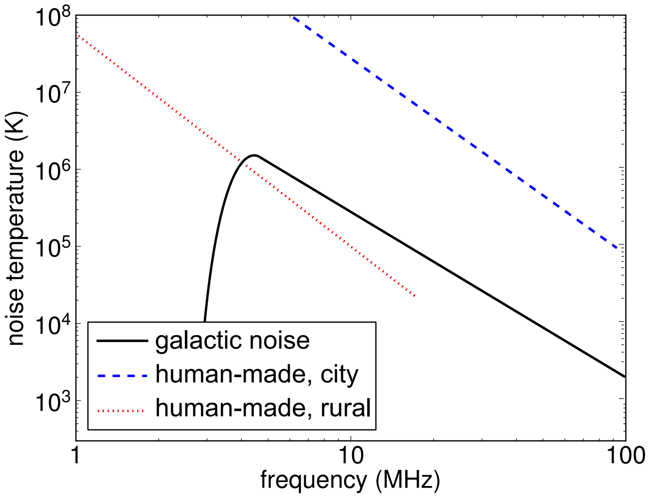

Figure 3.3: Noise contribution of galactic and human-made origin in the most commonly used radio frequency band for the detection of cosmic rays. Galactic noise limits the detection of radio signal on remote measurement sites. Fig. after Ref. [80].

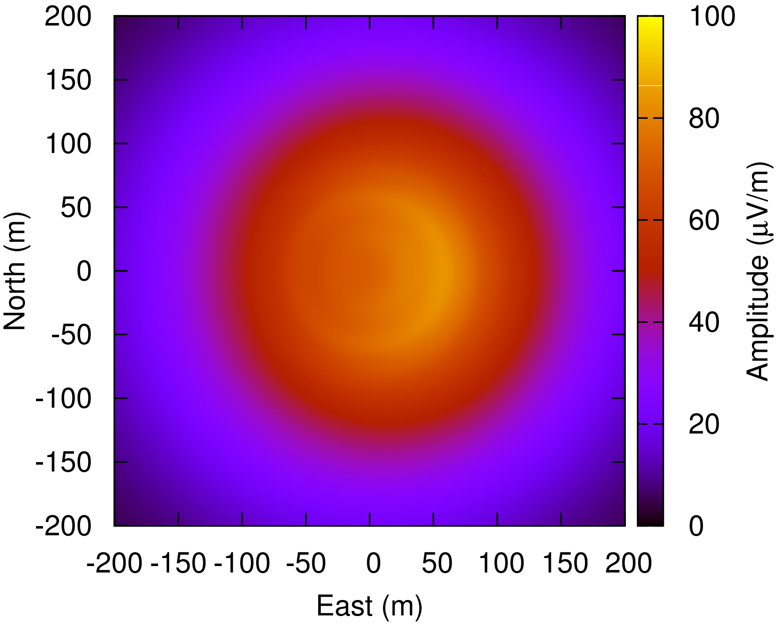

Figure 3.4: Simulated footprint of the radio signal, bandlimited to 30-80 MHz, from a 10^{17} eV vertical proton air-shower in the Tunka valley. Since typical detection thresholds for individual antennas are 60-100 µV/m, this shower is close to the detection threshold.

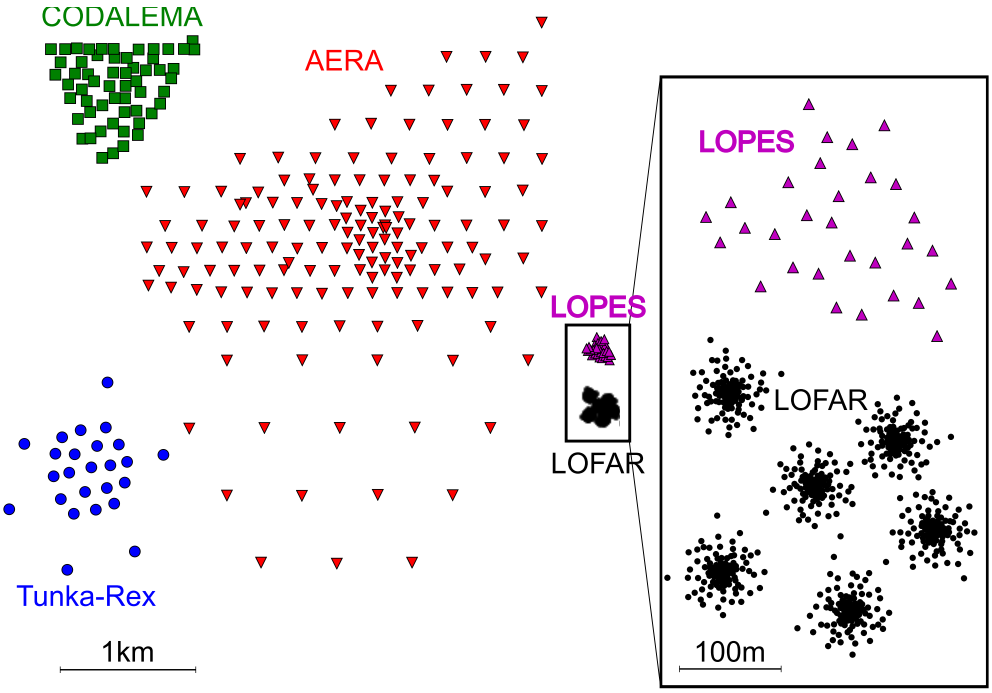

Figure 3.5: Layouts of the radio experiments detecting cosmic rays in a frequency band of approximately 30-80 MHz. The order of magnitude for the covered area is in the km^2 range, which provides sufficient statistics at the detection threshold of around 10^{17} eV.

since the 2000s, also reached sufficient sensitivity to the polarization of the signal to find contributions from the Askaryan effect on a statistical basis [81, 82, 83].

A reconstruction of the energy is possible by measuring the signal scale, e.g., via the amplitude at certain distance. This is demonstrated in detail in Sec. 7.1. Several experiments proved resolutions around 20% from comparisons with their host experiments [84, 85]. A recently published method based on the integrated power of the radio signal, reached a similar result [86].

Experimental indications for the sensitivity of the radio signal to the depth of the shower maximum were first claimed by the LOPES experiment: a correlation between the slope of the lateral distribution of radio amplitudes and the mean muon pseudorapidity of a shower was found. The muon pseudorapidity is an indicator for the muon production depth, which is connected to the height of the shower development [87]. The sensitivity of radio measurements to the longitudinal shower profile was confirmed recently by Tunka-Rex in the first direct comparison to independent measurements of the depth of the shower maximum by Tunka-133 [85].

In the following paragraphs, the digital radio experiments which measure in the 30-80 MHz frequency band are introduced. Their layouts are depicted in Fig. 3.5.

LOPES

The LOFAR Prototype Station [62] was an array of 30 inverted V-shaped dipole antennas, covering an area of roughly 200×200 m^2 and operating in the 43-74 MHz band. It was deployed on the KASCADE [44] field and triggered by the KASCADE-Grande experiment [38], located at the Karlsruhe Institute of Technology (KIT), Germany. The advantages of LOPES were the available energy and geometry reconstruction to high precision from KASCADE-Grande. The downsides were its small covered area and proximity to densely populated areas with increased background.

LOPES operated from 2003 to 2013. With its high synchronization precision between antenna stations, on a level of 1 ns, it proved the feasibility of air-shower detection with digital radio interferometry and established many basic concepts realized in modern radio experiments [88, 89]. It was also one of the first absolutely calibrated radio experiments, giving important input to models of radio emission. The absolute calibration of LOPES is revised in the context of this work [1]. Furthermore, the measurement of the amplitude scale of radio emission at LOPES is compared to Tunka-Rex in Sec. 7.3.

LOFAR

The Low Frequency array [64] is a large radio interferometer, distributed over several countries in Europe. It is designed for radio astronomy, but the central antenna clusters in the Netherlands are extended with a scintillator array to detect cosmic-ray air showers as well [90]. The covered area is about 300×300 m^2, containing 576 slanted dipole antennas operating in the 30-80 MHz band, of which half can be read out at once.

LOFAR has by far the densest layout, enabling a deep test of models for the distribution of radio amplitudes and shape of the radio wavefront [91, 92]. However, because it was not designed for cosmic-ray observation, it has only a simple scintillator array for triggering and for a rough estimation of the shower energy and geometry, but no independent information about the shower maximum. The amplitude scale of this experiment was calibrated lately, in the context of this work [2].

AERA

The Auger Engineering Radio Array is the radio extension of the Pierre Auger Observatory, in Marlague, Argentina [65]. It consists of more than 150 antennas of different types, partially log-periodic dipole antennas and partially butterfly antennas, which operate in the 30-80 MHz band [93]. With 17 km^2, it covers the largest area of all radio experiments, thus potentially extending to the highest energies. However, the lower energy threshold suffers from the Earth's magnetic field being close to the global minimum at the site. Furthermore, the infill array of the surface detector of the Auger Observatory, which is the host experiment of AERA, is comparatively sparse, causing an relatively large uncertainty on the shower geometry [94].

This experiment was one of the first to prove a contribution from the charge-excess emission to the polarization [81]. Furthermore, it is absolutely calibrated, but uses a different approach for energy estimation than prior experiments: integrating over the lateral distribution of radio amplitudes, the total energy in the radio signal is determined, which is correlated with the air-shower energy [86].

The electronics used for Tunka-Rex are based on designs for AERA, which saved significant cost for the development of Tunka-Rex [95]. Moreover, the software framework used for data analysis in Tunka-Rex is based on the radio part of the Auger Offline framework, developed by the Pierre Auger collaboration [96].

CODALEMA

CODALEMA [63] is a radio detector at the radio observatory of Nancey, France. Starting data taking in 2003, the detector currently operates 57 butterfly antennas, covering an area of about 1 km^2. The analyzed frequency band is 35-80 MHz. Although it also operates a scintillator array for triggering, one of its main goals is the development of a self-trigger.

Tunka-Rex

The Tunka-Radio extension is the main focus of this work and will be thoroughly described in the next chapter.

4 The Tunka detector complex and the Tunka Radio Extension

The Tunka detector complex consists of multiple detectors for high-energy cosmic rays, located at the coordinates 51°48' 35" N, 103°4' 2" E, close to the southern tip of Lake Baikal in Siberia, Russia. Its altitude is 670 m above sea level, resulting in a vertical atmospheric depth of 955 g/cm^2. Due to its location, surrounded by mountains, it is known for its dry climate, and especially suited for optical observation techniques.

The initial idea of the Tunka project was to study cosmic rays above an energy of 10^{15} eV with the air-Cherenkov technique. It started in 1993 with 4 photomultiplier (PMT) stations and was extended until 2000 to Tunka-25, with 25 PMT stations distributed over 0.1 km^2, which operated until 2003 [97]. Tunka-25 covered an energy range from 10^{15}-10^{17} eV.

In 2009 the project in the Tunka valley was continued with Tunka-133, a new, larger PMT array, comprising an air-Cherenkov detector for air showers up to 10^{18} eV. From the start of Tunka-133, test stations for the Tunka Radio Extension (Tunka-Rex) were deployed, to test their reliability for the planned antenna array. In 2012 almost all cluster centers of Tunka-133 were equipped with a Tunka-Rex antenna station, and data taking started in October 2012.

Since 2014, the site was further extended in the framework of the Tunka Advanced Instrument for cosmic-ray physics and Gamma Astronomy (TAIGA). It consists currently of the air-Cherenkov detector Tunka-133, the scintillator extension Tunka-Grande, and Tunka-HiSCORE, a non-imaging air-Cherenkov detector for air showers from gamma rays [37]. Stations of all detectors, except Tunka-HiSCORE are shown in Fig. 4.1. Another extension, an array of imaging air-Cherenkov telescopes, called Tunka-IACT, is already under construction.

This chapter starts with an introduction to Tunka-133, which provides a basis for the layout, data acquisition, trigger and to some extent the data analysis of Tunka-Rex. Then, Tunka-Rex is described, the focus of this work, and finally a short summary about the status of Tunka-Grande is given, the future host providing a trigger for Tunka-Rex.

4.1 Tunka-133: an air-Cherenkov detector

Tunka-133 is a non-imaging air-Cherenkov detector for air showers [8]. It consists of 175 PMT stations, distributed over 3 km^2. The layout is depicted together with the different Tunka-Rex stages in Fig. 4.2. The stations are grouped in clusters, which each consists of 7 PMT stations distributed in a hexagonal pattern. The clusters themselves are also

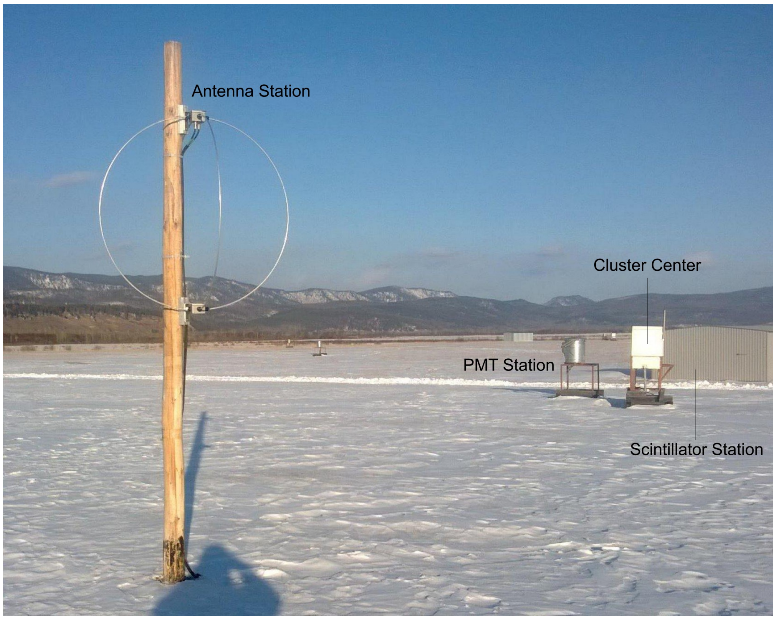

Figure 4.1: A Tunka-Rex antenna station with its two, perpendicular SALLA antennas in the front. In the back a PMT station of Tunka-133, the cluster center containing electronics and the housing of a Tunka-Grande scintillator station are visible.

distributed hexagonally. There is a central, dense array, with a radius of about 500 m, equipped with 133 PMTs in 19 clusters, hence the name Tunka-133. The PMT stations there have a spacing of about 85 m and cover an area of 1 km^2. Additionally, there are 6 outer clusters with distances of up to 1000 m from the center, increasing the effective area for the highest energies to about 3 km^2.

A PMT stations consists of a metal bin containing an 8 inch PMT, shown in Fig. 4.3. The PMT is covered by a window and pointed upwards. To avoid obstruction by snow or condensed water, the window is heated and covered by a remotely controlled lid during day time and bad weather. Due to the depth to which the PMT is suspended in the bin, Tunka-133 is fully efficient for all zenith angles $\theta \leq 50^\circ$ at energies $E > 10^{16.2}$ eV [20]. Via reflections from the inner bin walls, also events with higher zenith angles are detected, but with reduced efficiency and reconstruction quality [98]. In 2015, the interior of the metal bins was painted black to suppress reflections, and thus the detection of events with zenith angles above 50° is no longer possible.

The event reconstruction of Tunka-133 is based on autonomous cluster triggers. A cluster is triggered by at least 3 of the 7 PMTs in a cluster surpassing a signal threshold within 0.5 µs. After the trigger, data of the full cluster, i.e., the 7 PMTs and the Tunka-Rex station, is sent to the central data acquisition (DAQ) [99]. Events then have to be identified offline by looking for coinciding individual clusters.

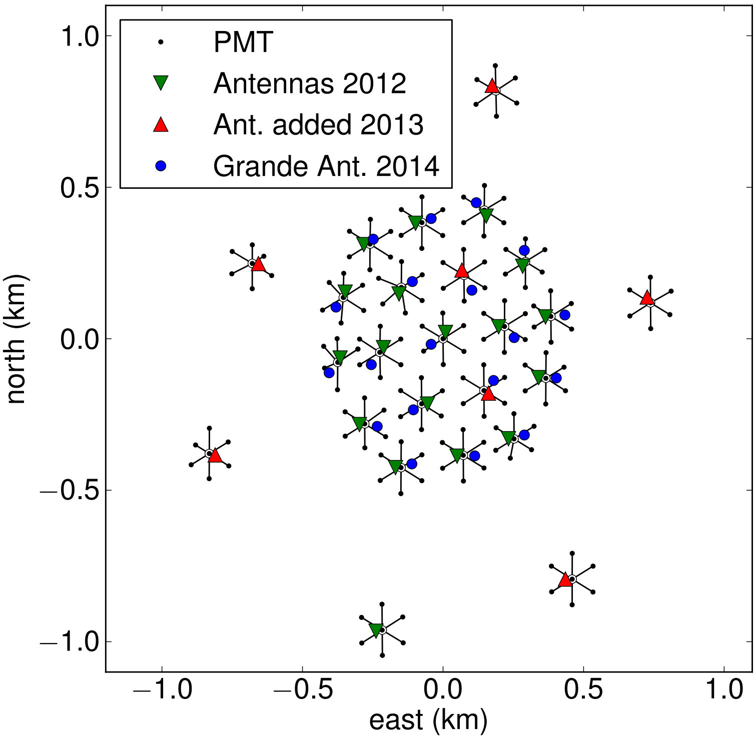

Figure 4.2: Layout of Tunka-133 and Tunka-Rex in its different stages. From 2013 on, all clusters of Tunka-133 also had an antenna station. In 2014 a second antenna station was placed close to each of the 19 first stations in the central array, together with the scintillator stations comprising Tunka-Grande.

As all optical detectors, Tunka-133 operates during clear, moonless nights. Additionally, the detector is shut down for maintenance in summer. From the 400 h of operation time per year, about 250 h remain after the selection of good-weather periods.

4.1.1 Data acquisition

Analog data from the PMTs of Tunka-133 and the Tunka-Rex antenna stations is sent via coaxial cable to the local data-acquisition (DAQ) electronics on cluster level. These electronics are located in the so-called cluster centers, i.e. white metal boxes with voltage supply and heating, located close to the central PMT of each cluster. A picture of the interior of a cluster center is shown in Fig. 4.4.

The analog signal is digitized in the cluster centers with analog-to-digital converters (ADC), implemented on the electronics boards of Tunka-133. In each cluster center there are 4 boards with a total of 16 channels. 14 channels are used by the 7 PMTs of the cluster, one for the anode and one for the last dynode of each PMT. The remaining two channels are used by Tunka-Rex and are read out together with all other channels in

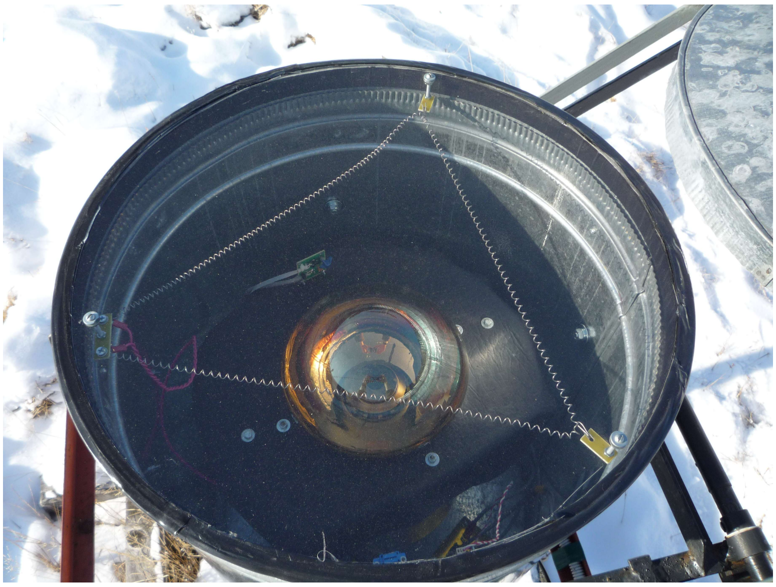

Figure 4.3: Interior of a PMT station, containing mainly the PMT of 8 inch diameter. The triangular shaped wire above the PMT is for heating, to keep the window dry.

case of a cluster trigger. The ADC boards are based on the 12-bit flash ADC AD9430 and have a sampling rate of 200 MHz.

In case of a trigger, the digitized data is sent via optical cables further to the central DAQ, where it is stored for later offline analysis. The recorded traces are 1024 samples long, corresponding to about 5 µs, and it is centered around the time of the cluster trigger of Tunka-133. The relative position of the signal in the antennas is determined in Sec. 6.2.

4.1.2 Tunka-133 reconstruction

The reconstruction of air-shower events with Tunka-133 starts with the recorded signal traces of the PMTs in different clusters. Clusters with coincident triggers within 2 µs are considered as one event [100]. Pulses in PMT traces are identified by a clear excess above the baseline over several samples. A parametrization of the pulse shape is fitted to the trace to identify the pulse maximum, integral, width and arrival time, where the latter is defined as the time when the signal reaches 25% of its maximum [100].

Combining pulse fits from all PMTs with signal, the arrival direction is determined with a fit of the arrival times to a parabolic shower front, using the signal center of mass as a preliminary estimate of the core position. The precision of the reconstructed arrival direction is 0.3° [8].

To increase the precision of the core position to about 10 m, it is determined from a fit of the distribution of signal amplitudes as a function of distance to the shower axis.

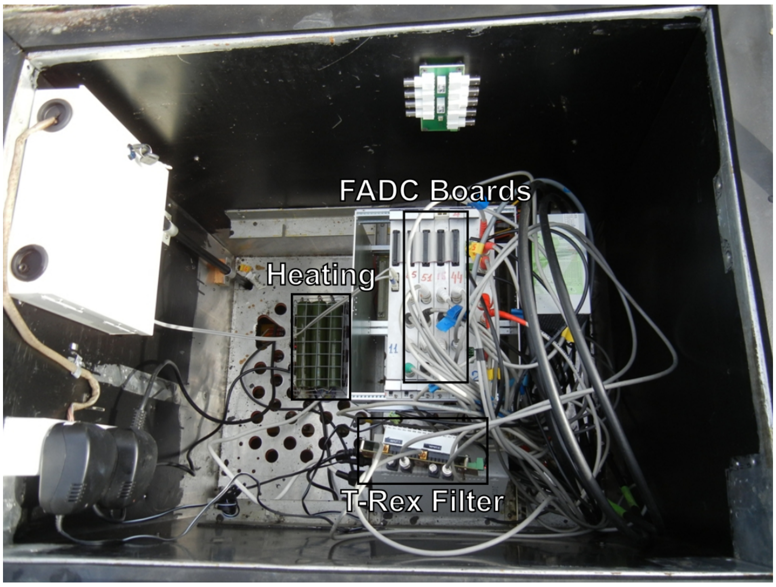

Figure 4.4: Interior of a cluster center. The signals of 2×7 PMT channels and 2 antenna channels enter via coaxial cable, are digitized and are further transmitted via optical cables to the central data acquisition for storage. The box is heated to ensure stable temperature conditions for the electronics.

Furthermore, the depth of the shower maximum X_{max} is reconstructed with the same fit from the slope of the amplitude-distribution function at a distance beyond 200 m from the shower axis [100]. For the energy reconstruction, the distribution of integrated signal pulses is fit. The reconstructed value at a distance of 200 m from the shower axis is used as an energy estimator [8]. In Fig. 4.5, an example event with both distributions is shown. The precision for the reconstruction of energy and X_{max} is 15% and 28 g/cm^2, respectively.

The calibration of the energy reconstruction originates from an absolute calibration for air-Cherenkov detectors, performed with the QUEST [101] experiment [101]. QUEST was an array of PMTs co-located with the EAS-TOP particle detector array [102]. The scintillator detectors from EAS-TOP were later used in the KASCADE-Grande [38] experiment and are currently used in Tunka-Grande [37]. The calibration for the reconstruction of X_{max} is performed by tuning the scale until Tunka-133 data fits to measurements of HiRES/MIA [103] and the fluorescence detector of the Pierre Auger Observatory [104, 100].

4.2 Tunka-Rex: a radio detector

Tunka-Rex is the radio extension of Tunka-133. A test station of Tunka-Rex was already deployed with the inauguration of Tunka-133, in 2009, to prove the principal

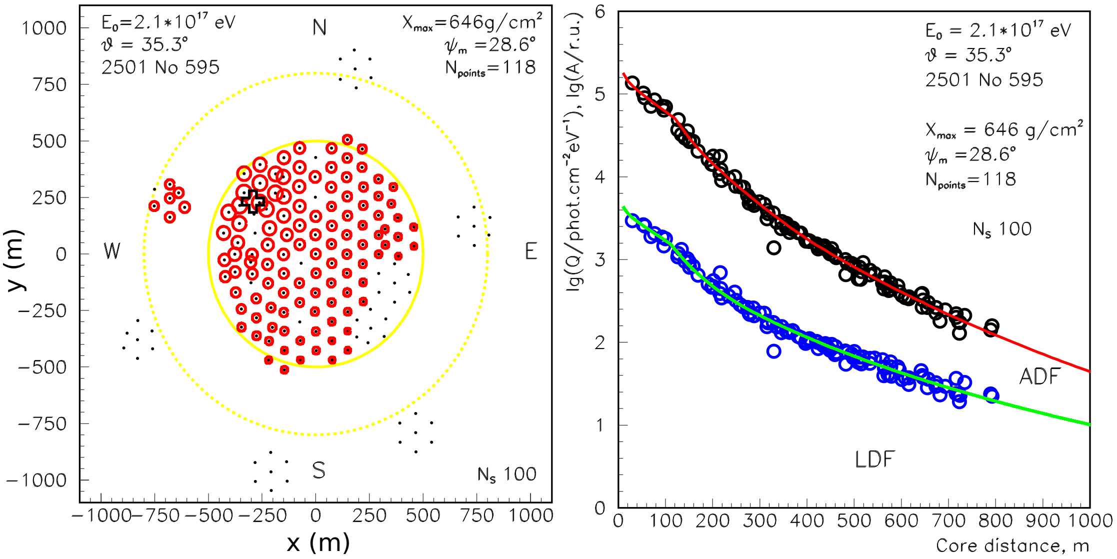

(a) (b)

Figure 4.5: (a) Lateral distribution of the air-Cherenkov signal on the Tunka-133 array in an example event with a reconstructed energy of $E_0 = 2.1{\cdot}10^{17}\,\mathrm{eV}$ and a zenith angle of $\vartheta = 35.3°$. (b) Lateral distribution function (LDF) and amplitude distribution function (ADF) (relative units) of the air-Cherenkov signal in shower coordinates. Fig. from Ref. [100].

functionality [105]. In 2012, 17 out of the 19 central PMT clusters, and 4 of the 6 outer clusters of Tunka-133 were equipped with an antenna station (see Fig. 4.2). All, except 3 of the outer stations, started operation the same season, in October 2012. For the second season, in 2013, the array was completed by equipping the remaining clusters with antennas, resulting in a total of 25 antennas, operating since October of the same year. The distribution of antennas follows the clusters of Tunka-133: 19 antennas are located in the central detector, with a spacing of about 200 m, covering an area of 1 km^2, and another 6 antennas with a spacing of 500 m extend the covered area to over 3 km^2. The array in its different stages is shown in Fig. 4.2.

The antennas of the first two seasons are plugged into the data-acquisition system of Tunka-133 and are solely triggered by Tunka-133 in the first two seasons, 2012/2013 and 2013/2014. Whenever Tunka-133 is triggered, the corresponding antenna data is stored as well. Therefore, the antennas were only operational together with Tunka-133 during moonless winter nights with good weather, resulting in a duty cycle of about 5%. While this strips the radio technique of one of its main advantages, its high duty cycle, it enables calibration and comparison of the reconstruction from Tunka-Rex to Tunka-133, a well-established device.

In 2014, the deployment of the scintillator extension Tunka-Grande started. Each of its stations has been equipped with a Tunka-Rex antenna station as well. Besides increasing the antenna density, from November 2015 on the scintillator detector triggers the full antenna array, greatly extending the uptime of Tunka-Rex. Furthermore, Tunka-Rex provides a connection between Tunka-133 and Tunka-Grande, and will be used for cross-calibration of all three devices.

4.2.1 Antenna station

The Tunka-Rex antenna station can be seen in Fig. 4.1. Each station has two perpendicularly aligned Short Aperiodic Loaded Loop Antennas (SALLA) [106] for the two channels. The two antennas are oriented with the antenna-arc plane rotated by ±45° with respect to the magnetic north. With the two channels combined, the station is sensitive to both polarization components of an incoming radio signal in the far field region of the source. Thus, the full electric-field vector, defining the radio signal, can be reconstructed, given that the incoming direction of the signal is known.

Each SALLA consists of two aluminum arcs with 120 cm diameter. It is an economic and rugged antenna. Towards the ground, in the lower box connecting the antenna arcs, it houses a load with a resistance of 390 Ω. This reduces the antenna sensitivity from below, suppressing the reception of reflections from the ground. Thus, the SALLA features negligible systematic uncertainty from the dependence of gain and directional pattern on the ground conditions. As a trade-off, the SALLA has generally a lower gain than common alternatives [93]. The properties and calibration of the antenna are discussed in detail in Secs. 5.4 and 5.5 and the impact of the reduced gain on the detection threshold is small, as discussed in Sec. 6.4.

The antenna footpoint is directly connected to a low-noise amplifier (LNA) in the upper box connecting the arcs. For better impedance matching of antenna and LNA, the antenna is coupled via a 4:1 impedance transformer. The LNA amplifies the signal by about 24 dB. 29.9 m of RG213 cable connect the LNA at the antenna to a filter amplifier in the cluster center. The cluster center contains also the electronics for data acquisition.

The filter amplifier enhances components of the signal inside the design frequency band of 30-80 MHz by about 32 dB and attenuates components outside this band. The design of the filter amplifier is based on hardware developed and used by AERA [95]. Properties of the electronics are further discussed in Sec.5.3.

The data acquisition (DAQ) of Tunka-Rex is identical to the DAQ of Tunka-133, already described in Sec. 4.1.1. The sampling rate of 200 MHz is sufficient to fully cover the design band of Tunka-Rex of 30-80 MHz in the first Nyquist domain [107].

4.2.2 Timing calibration

Because the individual clusters of Tunka-133 operate independently, they have to be synchronized in order to later reconstruct the arrival direction of air showers. This is done by sending a synchronous signal at the beginning of each night from the central

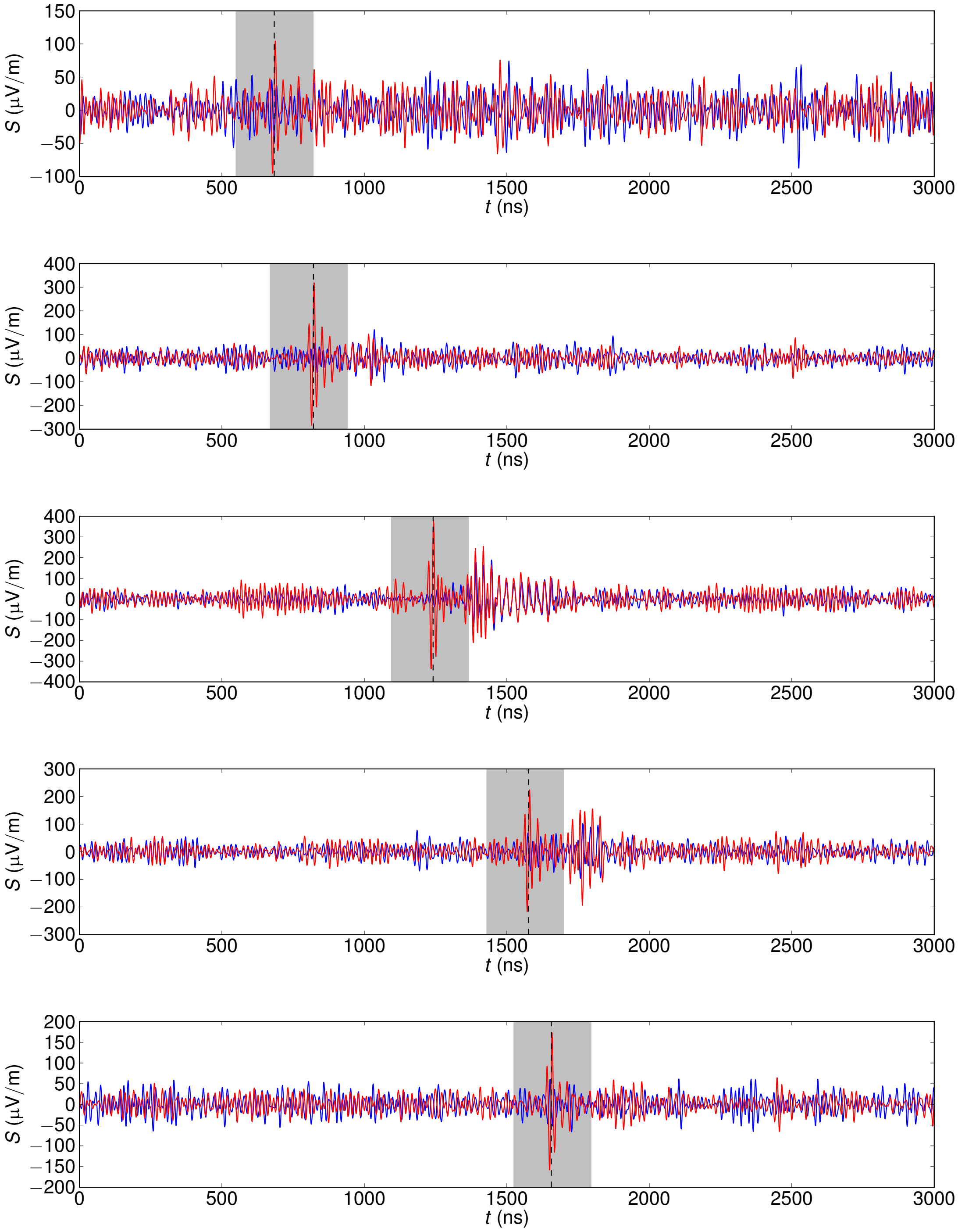

Figure 4.6: Typical Tunka-Rex event: Traces from the two channels (red and blue lines) of 5 antenna stations with signal. From the sequence of signal-pulse times (dashed lines), the incoming direction of the air shower can be reconstructed (depicted in Fig. 4.7). Grey boxes indicate the signal window. The time axes of the traces were shifted to start simultaneously.

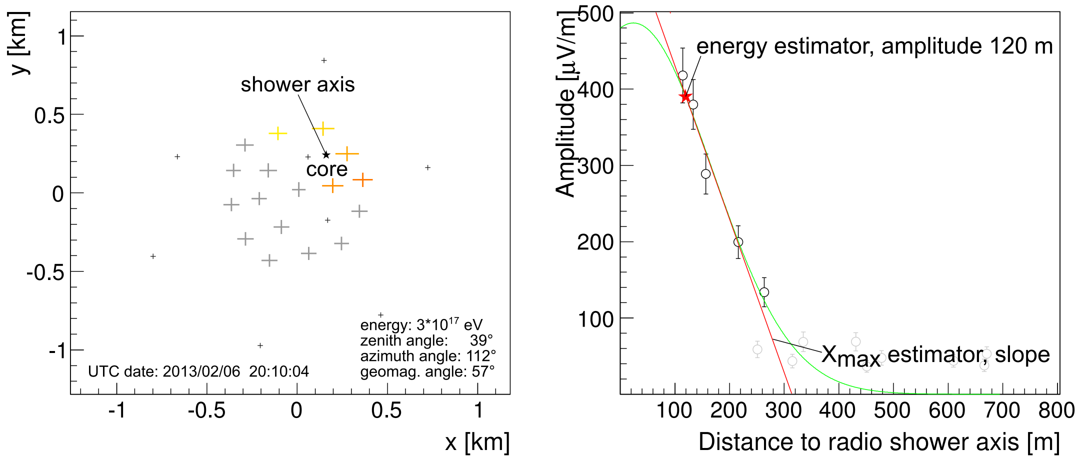

(a) (b)

Figure 4.7: (a) Signal distribution on the array for the Tunka-Rex event shown in Fig. 4.6 and the reconstructed shower axis. The color code indicates the arrival time of signal pulses. (b) Lateral distribution of signal amplitudes. Primary energy and the depth of the shower maximum can be reconstructed from the amplitude at 120 m and the slope of the distribution, respectively.

DAQ, in the center of the array, to the local DAQs of all clusters. The signal is returned, and with the delay until return, differences in propagation times between cluster centers can be determined and corrected. Furthermore, a master clock, from which all local clocks are derived, is provided by the central DAQ to all cluster centers. Lastly, all local clocks are centrally reset each second to avoid drifts.

With this procedure, a relative timing accuracy of about 10 ns between different clusters is achieved [99]. This means that the different clusters have offsets of several ns against each other. These offsets are stable to sub-ns level within a night, but jump by several ns in between nights [108]. In Sec. 6.3.2 its is shown that this accuracy suffices to reconstruct the incoming direction of an air shower with a precision of 1°. In Fig. 4.6, the traces of an example event are shown on a synchronized time axis, and in 4.7 the direction reconstruction is illustrated. The lateral distribution of radio amplitudes and reconstruction of air shower parameters, illustrated in Fig. 4.7 (b), is further discussed in Sec. 6.3.3.

For Tunka-133 the timing accuracy is further improved using data from measured air-shower events: by minimizing the residuals to a parabolic shower front model in high-energy events, the timing is determined with better accuracy [20]. For Tunka-Rex, a similar approach is currently under development with the goal to achieve about 1 ns relative timing accuracy. Such an accuracy is necessary for an analysis of the radio wavefront or for application of interferometric methods [89].

(a) (b)

Figure 4.8: (a) Interior of the aluminum huts, housing the scintillator detectors of Tunka-Grande. (b) There are also underground detectors, in a tunnel at a depth of 1.5 m. They are shielded versus electrons and photons, to measure the remaining muonic shower component.

4.3 Tunka-Grande: a particle detector array

Tunka-Grande is a detector consisting of 19 scintillator stations at the Tunka site. Its layout is depicted in Fig. 4.2 and follows that of the central Tunka-133 clusters. The exterior of a station is an aluminum hut, which can be seen in Fig. 4.1. It houses 12 aboveground scintillators and 8 underground scintillators for muon detection, shown in Fig. 4.8. The scintillators are each $80 \times 80 \times 4\,\mathrm{cm}^3$ in size and were already used for the cosmic-ray experiment KASCADE-Grande [37] and before that in EAS-TOP [102]. The muon detectors are located in a tunnel at a depth of 1.5 m beneath the surface, shielded by soil and concrete against electrons. As of the 2014/2015 season, only the 7 innermost scintillator stations had the muon detectors installed.

DAQ and time synchronization are similar to Tunka-133. Each station features a Tunka-Rex antenna connected to its DAQ, almost doubling the antenna number of Tunka-Rex to 44. From November 2015 on, Tunka-Grande is operated also during daytime, triggering the full Tunka-Rex array, and therefore potentially increasing the uptime of Tunka-Rex by one order of magnitude. Tunka-Rex can provide an absolute energy scale for Tunka-Grande and will be used to cross-calibration Tunka-133, Tunka-Grande and Tunka-Rex.

This instrument can be used to investigate the capabilities of a radio detector in combination with a scintillator detector, accessing both, the electron-to-muon ratio and the depth of the shower maximum for the determination of the mass composition.

5 Calibration of the signal chain for the Tunka radio station

[1] The purpose of the Tunka-Rex antenna station is to measure the radio signal from cosmic-ray air showers. After reception by the antenna, the signal has to traverse several hardware components until a trace is recorded in units of ADC counts. A reconstruction of the initial incoming signal, in terms of physical units on an absolute scale, requires detailed knowledge about the transmission properties of all stages of the signal chain. This enables a comparison of the measured signal with model calculations or independent, calibrated measurements by other experiments.

In this chapter, the signal reconstruction for Tunka-Rex is developed, and the calibrations of the different stages of hardware are described. It starts with an introduction on how the incoming signal can be reconstructed from the linear response functions of the signal chain components. The signal chain is then divided into two parts, the electronics and the antenna. For the electronics, scattering parameters are introduced, as a representation of their linear response functions. The scattering parameters are determined in a measurement under laboratory conditions. After a short introduction to antenna theory, the vector effective length is identified as the most useful representation of the antenna-response function. Since the antenna is sensitive to its surroundings, it cannot be calibrated easily to high precision under laboratory conditions. Therefore, a calibration campaign with a reference source was conducted to obtain the vector effective length from a combination of measurements and an antenna simulation. Finally, uncertainties for the signal reconstruction are discussed.

5.1 Signal reconstruction

A radio signal, received by the Tunka-Rex antenna station, has to traverse antenna, low-noise amplifier, coaxial cable, filter amplifier and digitizer electronics. These parts comprise the signal chain. Since each stage is linear to good approximation, the output can be obtained by convolving the incoming signal E with the linear response function H of the respective part of the signal chain

$$E_{\text{out}}(t) = E_{\text{in}} * H = \int_{-\infty}^{\infty} H(t-\tau) \cdot E_{\text{in}}(\tau) d\tau. \tag{5.1}$$

Because air-shower signals have limited support, Eq. 5.1 can be approximated in their case by an integral over a recorded trace with finite length.

---

[1] Parts of this chapter have been published in Ref. [66].

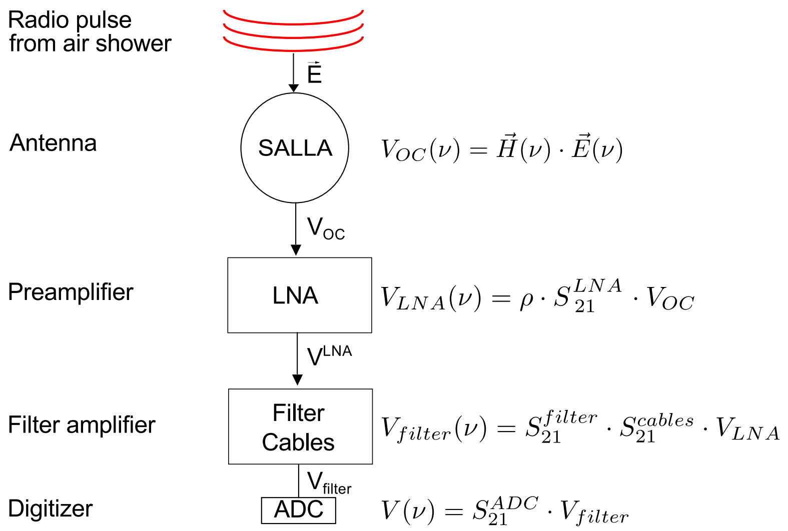

Figure 5.1: Flow diagram of the signal transmission and data acquisition of the Tunka-Rex antenna station. On the right hand side there is the corresponding transformation in the frequency domain for each transition.

The calculation is most conveniently handled in the frequency domain, by Fourier transforming signal $\mathcal{F}(E) = \mathcal{E}$ and response $\mathcal{F}(H) = \mathcal{H}$. With the convolution theorem, the convolution turns into a point-wise multiplication in the frequency domain

$$\mathcal{E}_{\text{out}}(\nu) = \mathcal{E}_{\text{in}} \cdot \mathcal{H}. \tag{5.2}$$

As discussed in the following sections, the linear response functions of the electronics parts and the antenna are the forward transmissions S_{21} and vector effective length $\rho\vec{\mathcal{H}}$, respectively. A flow diagram with the different stages of the signal chain and the respective transformations is shown in Fig. 5.1. Combining all transitions gives the total linear response in the frequency domain for the full signal chain

$$\mathcal{V}_{\text{out}}(\nu) = S_{21}^{\text{ADC}} S_{21}^{\text{filter}} S_{21}^{\text{cable}} S_{21}^{\text{LNA}} \cdot \rho\vec{\mathcal{H}}\vec{\mathcal{E}}. \tag{5.3}$$

$\vec{\mathcal{E}}$ is the incoming signal in terms of electric field strength. $\mathcal{V}$ is the output voltage of the analog signal chain fed to the ADC boards and recorded in terms of ADC counts.

In order to obtain the original incoming signal in terms of electric-field strength, the digitization and system response of the signal chain has to be inverted. For the digitization procedure this is simple backward mapping of ADC counts to voltage and will be discussed in Sec. 5.3. However, to invert the projection of the electric field on the vector effective length in Eq. 5.3, information from both antenna channels has to be used, by combining them in a system of equations

$$\vec{\mathcal{V}}(\nu) = \mathcal{H}\vec{\mathcal{E}}. \tag{5.4}$$

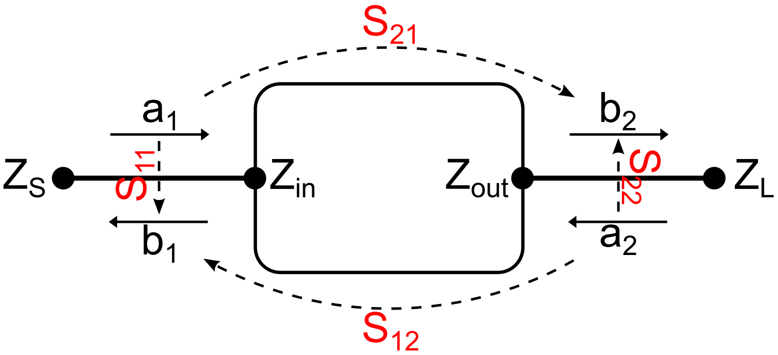

Figure 5.2: Illustration of a linear two-port network. The scattering parameters S_{ij} give the complex amplitudes of transmitted and reflected waves, relative to the incoming ones a_1 and a_2 for both ports. The resulting outgoing waves b_1 and b_2 can be calculated from them. Z_{S},Z_{L}, Z_{in} and Z_{out} denote the impedance of source, load, network input and output.

The elements of $\vec{\mathcal{V}}(\nu)$ are voltages from the two channels, and rows of the $2{\times}2$ matrix $\mathcal{H}$ are the vector effective lengths of the channels multiplied by the electronics response. Eq. 5.4 can be inverted to obtain the electric-field vector with two exceptions: lacking sensitivity to some polarization component perpendicular to the incoming direction of the signal, or the channels having linear dependent responses. By aligning the two antennas of a station perpendicularly, both cases are generally avoided.

The system response $\mathcal{H}$ depends on the incoming directions, which consequently has to be known for signal reconstruction. One way to solve this problem is by reconstructing the incoming direction iteratively, adapting the antenna response in each step [109]. For the Tunka-Rex standard analysis, this problem is solved by setting the direction to the incoming direction of the air shower, reconstructed by Tunka-133.

5.2 Scattering parameters

While the electronics in the analog hardware chain are complicated networks with many parts, the analysis of their response can be simplified by utilizing their linearity. A linear system preserves the frequency of an input sine wave and only changes its phase and amplitude. For a two-port network this means that a wave, entering at port 1, will at least partially be transmitted to port 2 and have the same frequency there. However, if not perfectly matched, the wave will also be partially reflected.

Treating all parts as abstract linear two port networks, they become black boxes, whose response for each frequency is fully described by 4 parameters. These 4 parameters can be represented in different ways. In high frequency applications, scattering parameters S_{ij} are a typical choice, because they can be measured directly.

For an incoming sine wave at port 1, with complex amplitude a_1, and reflected wave

b_1, and likewise a_2, b_2 for port 2, the scattering parameters are defined as

$$\begin{pmatrix} b_1 \\ b_2 \end{pmatrix} = \begin{pmatrix} S_{11} & S_{12} \\ S_{21} & S_{22} \end{pmatrix} \cdot \begin{pmatrix} a_1 \\ a_2 \end{pmatrix} . \tag{5.5}$$

The parameters are illustrated in Fig. 5.2. If there is an incoming wave to one port, but none to the other, the scattering parameters describe for each frequency the amplitude and phase of the reflected or transmitted wave relative to the incoming one.

In practice, the network has always to be operated with a source and a load connected to its input and output. The outgoing wave is in general a superposition of the reflected and transmitted waves at the respective port plus reflections from source and load. The reflection coefficients r, common in wave mechanics, are independent of source and load, and can be calculated from the scattering parameters:

$$r_1 = S_{11} + \frac{S_{12} S_{21} r_\mathrm{L}}{1 - S_{22} r_\mathrm{L}} \tag{5.6}$$

$$r_2 = S_{22} + \frac{S_{12} S_{21} r_\mathrm{S}}{1 - S_{11} r_\mathrm{S}} . \tag{5.7}$$

r_L and r_S are the reflection coefficients of the load, connected to port 2, and the source, connected to port 1, respectively. If the source is impedance-matched to the input and the load is impedance-matched to the output of the network, the source and load reflections disappear, $r_\mathrm{L} = r_\mathrm{S} = 0$. In that case, the reflection coefficients are identical with S_{11} and S_{22}.

The transmission parameters t, often mentioned in this context, have to be handled with care

$$t = 1 + r. \tag{5.8}$$

In the case of a linear, active network, t describes the amplitude of the wave entering the network, i.e., the voltage drop over its load, but not necessarily the outgoing wave at port 2, because the network can shift phase and change the amplitude linearly. Still, t will be needed later on to describe the response of the low-noise amplifier, when it is loaded with the antenna impedance, with measurements taken while it was matched to $50\,\Omega$.

A typical application for scattering parameters are amplifiers. With the forward direction from port 1 to 2, ideally all elements of the scattering matrix should be zero, except the forward transmission S_{21} which should be large. In that case, the forward transmission describes the change in amplitude and phase for signal components of all frequencies when traversing the amplifier and is equivalent to the more commonly used power gain $G = |S_{21}|^2$. Therefore, S_{21} can be interpreted as the response function of the system in the frequency domain, i.e., the Fourier transform of the response function, and directly used for signal reconstruction.

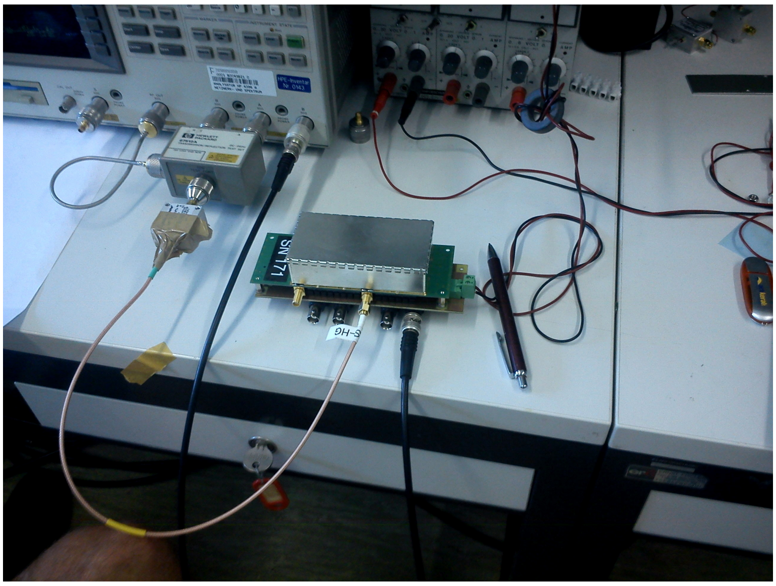

Figure 5.3: The Tunka-Rex filter amplifier during the calibration measurement with the network analyzer HP Agilent 4396A. The signal input 2 and output 4 are tested here. The BNC output channels 1 and 3 of the filter are only dummies, originally being designed for an additional low gain channel for AERA.

5.3 Electronics calibration

The network analyzer HP Agilent 4396A was used to measure the scattering parameters S_{ij} of the low-noise amplifiers, filter amplifiers and cables in the laboratory. The measurement setup of the filter amplifier can be seen in Fig. 5.3. The network analyzer is connected to the input and output of the part under test. A sine-wave signal from one side, input or output, is compared to the received signal from either the other or the same side to determine the respective scattering parameters. E.g., for the forward transmission S_{21}, the input signal is compared to the output signal. Scanning a given frequency range, the relative amplitudes and phases are recorded, directly representing the scattering parameters. Before a measurement, the network analyzer is calibrated with cables, connectors etc. as during the measurement. With proper setup and calibration, the measurement uncertainty is below 1% on the amplitude and below 1° on the phase.

Low-noise amplifier

The low-noise amplifier (LNA) is the first amplification stage, directly connected to the antenna. Its purpose is to maximize the signal-to-noise ratio by amplifying the signal as early in the signal chain as possible, before attenuation can happen due to propagation through cables. Additionally, the LNA should add little noise, because its contribution

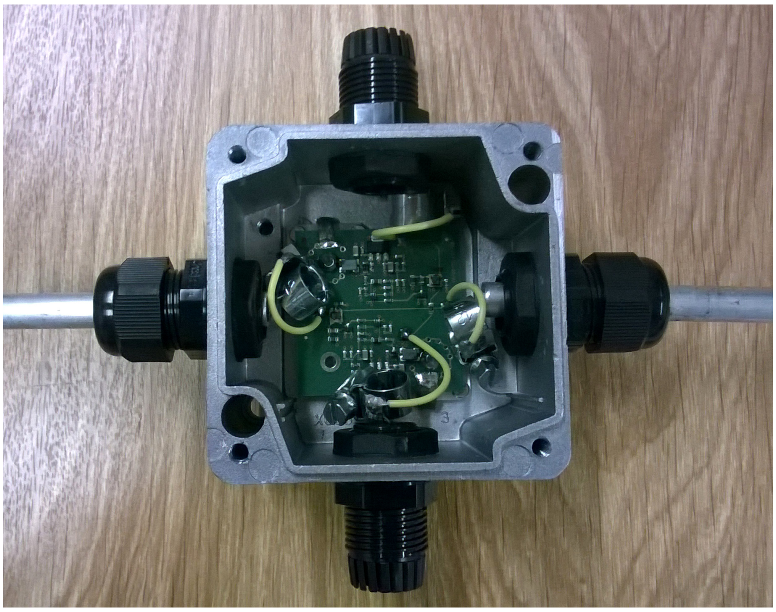

Figure 5.4: The Tunka-Rex low-noise amplifier (LNA). It is connected via clamps to the antenna arcs and located in the upper antenna box (see Fig. 4.1). The board has two LNA mounted, one for each channel of the antenna station.

adds directly to the effective system noise temperature T_{sys}. For components later in the signal chain this is less important, since all further noise contributions T are effectively damped by the power gains G of the prior stages

$$T_{sys} = T_1 + \frac{T_2}{G_1} + \frac{T_3}{G_1 \cdot G_2} + ... + \frac{T_n}{G_1 \cdot G_2 \cdot ... \cdot G_{n-1}} = \sum_{i=1}^{j} \frac{T_i}{\prod_{k=0}^{i-1} G_k} \; ; \; G_0 = 1. \tag{5.9}$$

Therefore, the system is usually dominated by the noise contributions until the first amplifier stage.

Details on the amplifier design can be found in Ref. [95], where also stability and linearity were shown. The noise temperature is around 200 K, which is of the same order of magnitude as the contribution from the resistor of the SALLA, as well as the galactic background received by the antenna.

The low-noise amplifier is shown in Fig. 5.4. It is connected via clamps to the antenna arcs and has a N-type connector for its output from below. It is supplied via a bias voltage of 6 V on the signal cable from the filter amplifier.

The measurement of the scattering parameters in this case is not as simple as for the remaining parts: the low-noise amplifier input has to be connected, and therefore impedance matched, to the antenna. The antenna impedance is generally not constant over frequency and it is not possible to achieve matching over a wide band. To improve the impedance matching to the antenna, the amplifier features a 4:1 impedance transformer at its input, transforming the 50 Ω input impedance of the LNA to 200 Ω, which is closer to the impedance of the SALLA.

For the calibration measurement in the laboratory, this firmly attached transformer is inverted using a measurement adapter with inverse transformation ratio. The clamps of the amplifier are connected to the BNC output of the network analyzer via this adapter, which introduces a significant systematic uncertainty, as discussed in Sec. 5.7.

The output of the low-noise amplifier is matched to 50 Ω, which is similar to the network analyzer ports and the signal chain.

In Figs. 5.5 and 5.6 the gain[2] and group delay[3] of the forward transmission are depicted. After a steep rise up to a frequency of 20 MHz, the amplification stays stable at around 22 dB. The production variations are 0.1 dB and the measurement uncertainty is 0.02 dB.

The phase shift is in good approximation linear. Consequently, the group delay varies little, between 4 to 8 ns with an uncertainty of 2 ns (compared to cables and filter with group delays around 100 ns).

The reflection S_{11} was measured as well. Due to impedance matching in the measurement, it was found to be below −10 dB in the design band. However, because of the different impedance load of the LNA, when connected to the antenna, the determined S_{11} has little direct meaning for measurements at Tunka-Rex. It will be needed later for the determination of the LNA input impedance, which is required to correct for the impedance mismatch between the LNA and the antenna.

Because of the good impedance matching of filter and cable, there is little reflection towards the LNA output and S_{12} and S_{22} of the amplifier have negligible impact on the signal reconstruction. They were exemplarily measured to be around −30 dB and −10 dB, respectively, but not determined for all parts individually and are not further taken into account.

Impedance matching

Since the low-noise amplifier will be operated at a different impedance than during the calibration measurement, the impact of the mismatch between antenna and amplifier has to be considered for signal reconstruction. Therefore, the amplitude transferred from the antenna to the amplifier input is determined, as well as how this amplitude is changed by the low-noise amplifier.

The amplitude transfer corresponds to the voltage dropped over the low-noise amplifier input. In the Thevenin equivalent diagram of the antenna and the amplifier, both input impedances are simply connected serially. Thus, the fraction of voltage, dropped over

---

[2] The gain G is the logarithmic power ratio: $G[dB] = 20 \cdot \log |S_{ij}|$.

[3] The group delay τ is the derivative of the phase $\varphi = \arg S_{ij}$ with respect to frequency: $\tau = -\frac{\mathrm{d}\varphi}{\mathrm{d}\omega}$. If $\tau(\omega)$ is constant, the signal shape is conserved and τ is equal to the time delay.

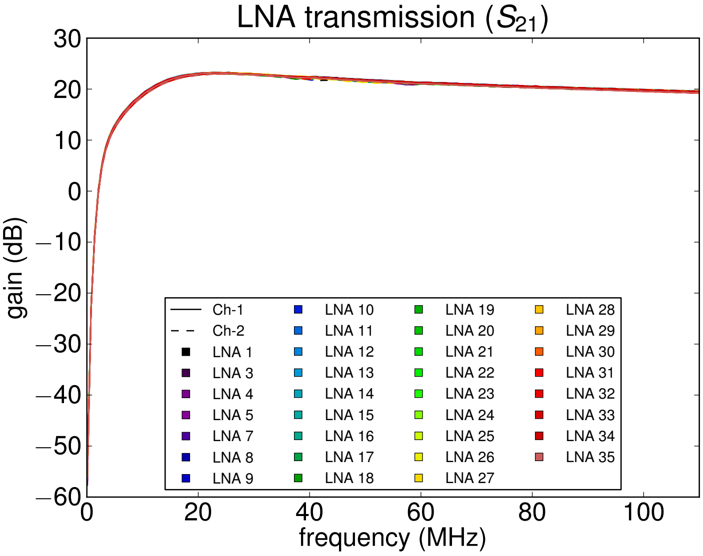

Figure 5.5: Forward gain of the LNA. The impedance mismatch between the LNA input and the antenna, as well as the network analyzer, is later taken into account for the calibration and signal reconstruction. The color code applies to all figures for the LNA in this section.

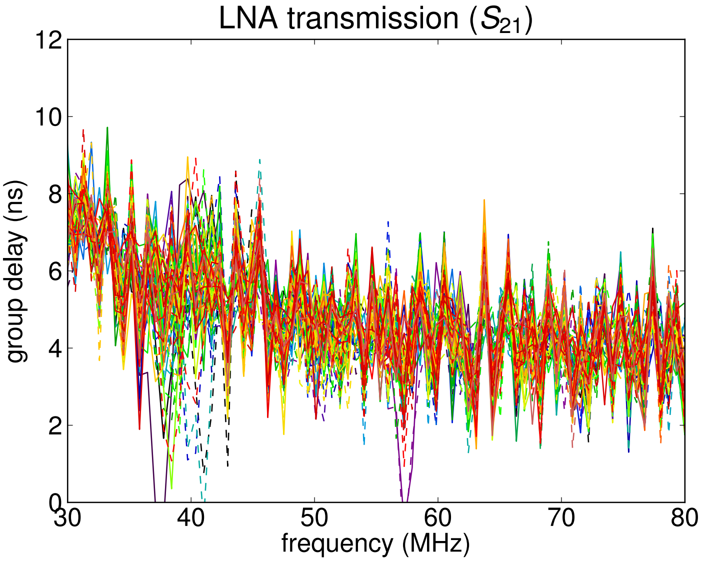

Figure 5.6: The group delay of the LNA is generally small and constant to good approximation. It therefore conserves signal shapes and maximizes signal-to-noise ratios for peaked signals. The scatter corresponds to the measurement uncertainty of the group delay.

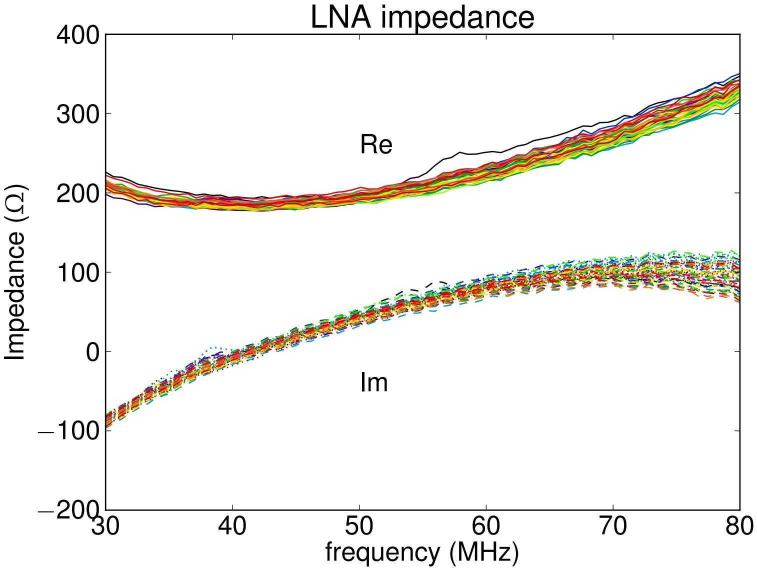

Figure 5.7: Input impedance of the LNA, with real part in continuous and imaginary part in dashed lines. For proper measurements with the network analyzer, a measurement adapter is used to recover impedance matching to 50 Ω during the measurement. The signal transmission from antenna to LNA depends on the impedance matching.

the amplifier input impedance is [110]

$$\rho(\nu) = \frac{Z_{\mathrm{LNA}}}{Z_{\mathrm{SALLA}} + Z_{\mathrm{LNA}}}. \tag{5.10}$$

The matching factor ρ describes the fraction of open-circuit voltage of the antenna V_{oc} dropping over the LNA impedance. V_{oc} is the maximum voltage drop over the antenna ports, when they are terminated with infinite resistance. ρ is determined by the impedances of the amplifier Z_{LNA} and the antenna Z_{SALLA}. The antenna impedance is retrieved from an antenna simulation in Sec. 5.4, because it cannot be reliably determined under laboratory conditions. With the output impedance of the network analyzer $Z_{\mathrm{NWA}} = 50\,\Omega$, the input impedance of the amplifier can be determined from the reflections measurements with $r = S_{11}$

$$Z_{\mathrm{in}}(\nu) = n_Z \cdot Z_{\mathrm{NWA}} \cdot \frac{1 + S_{11}}{1 - S_{11}}. \tag{5.11}$$

The impedance transformer, included in the measurement adapter, with the transformation ratio $n_Z = 4$ is taken into account here. The resulting input impedance is shown in Fig. 5.7.

Finally, the measured forward transmission of the LNA has to be corrected for the influence of the measurement setup, i.e. for reflection during the calibration measure-

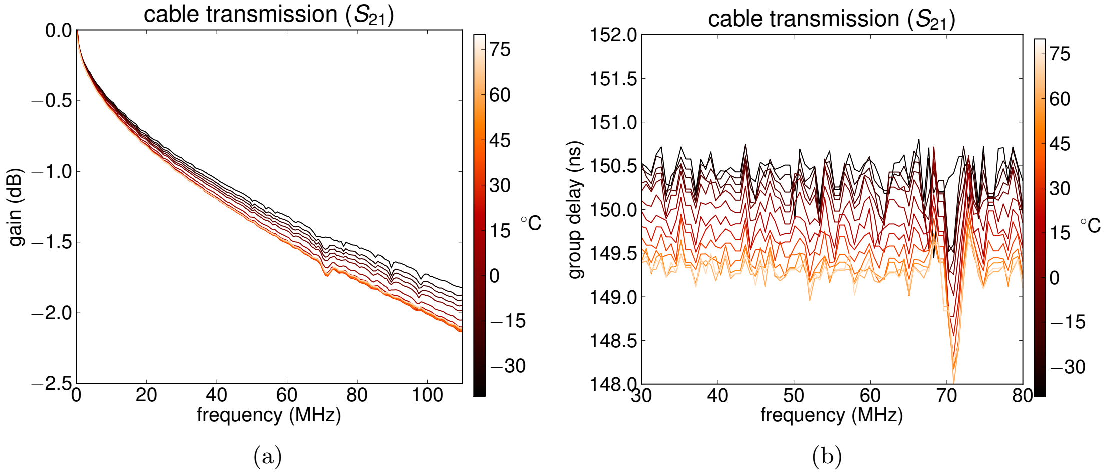

(a) (b)

Figure 5.8: (a) Gain and (b) group delay of one of the 29.9 m long RG213 cables connecting the LNA to the filter amplifier. While the dependence of the gain on the temperature contributes to the systematic uncertainty, the change of the group delay is small compared to other uncertainties.

ment and the transformer in the adapter. Because the signal transfer into the LNA is described separately by the matching factor ρ, the measured forward transmission does not describe the remaining transmission characteristics of the LNA properly. For this remaining part, a transmission parameter is determined which gives the ratio between the amplitude of an outgoing wave b_2, to the one entering the LNA a_1^{in}, which remains after transformation and reflection at the input. It can be obtained with Eqs. 5.5 to 5.8, assuming approximate matching, i.e., $a_2 = r_{\mathrm{S}} = r_{\mathrm{L}} = 0$. Additionally, treating amplitudes, the voltage transformation due to the measurement adapter has to be taken into account with $U_{\mathrm{out}} = U_{\mathrm{in}}/\sqrt{n_Z}$:

$$S_{21} = \frac{b_2}{a_1^{in}} = \frac{b_2}{a_1} \cdot \frac{1}{\sqrt{n_Z} \cdot (1 + S_{11})} = \frac{S_{21}^{\mathrm{meas}}}{\sqrt{n_Z} \cdot (1 + S_{11})}. \qquad (5.12)$$

S_{21}^{meas} is the forward transmission measured with the network analyzer. S_{21}, multiplied with the matching factor ρ, is the amplitude transmitted to the LNA output per amplitude of the open-circuit voltage of the antenna.

Transmission lines

The LNA and filter amplifier are connected by two lines of (29.9 ± 0.1) m RG213 coaxial cable, on for each channel. Although being very well matched to 50 Ω, and therefore having negligible reflections, the cables feature a frequency dependent attenuation and delay, and therefore, have to be taken into account during reconstruction of signals measured by Tunka-Rex.

In terms of scattering parameters cables are a very simple two port systems: S_{11} and S_{22} are very close to zero and S_{21} and S_{12} are similar. In Fig. 5.8, the transmission for one of the used cables is shown as an example at different temperatures. The cable attenuates the signal by 1 to 2 dB depending on frequency, and delays it by a constant time of about 150 ns. The values given by the data sheet [111] are 1.4 dB attenuation at 50 MHz with a delay of 149.5 ns, fitting well to the measured values within uncertainties.

Filter amplifier

The filter amplifier is the last part of the analog hardware chain of Tunka-Rex and the last amplification stage before digitization. Since for the digitization it is necessary to discretize the signal in time, i.e. record the signal strength in certain time intervals defined by the sampling rate, part of the information can get lost. This issue is most conveniently discussed in the frequency domain, by Fourier transforming the signal shape: according to the Nyquist-Shannon sampling theorem [107] the information of a signal, sampled at a certain frequency, can be fully restored in case of a finite signal bandwidth. With the sampling rate ν_s and the upper band limit ν_max, the requirement to conserve the information is

$$\nu_\mathrm{s} > 2\nu_\mathrm{max}. \tag{5.13}$$

Signal components with frequencies above half the sampling rate cannot be distinguished from corresponding components at lower frequencies. This phenomenon is known as aliasing.

For the Tunka-Rex experiment, the signal is sampled at 200 MHz. Consequently, an analog band-pass filter is used remove signal components above 100 MHz. To avoid background from commonly used radio communication bands, the design frequency band of Tunka-Rex is further restricted to 30-80 MHz. Similar bands are realized in the experiments LOPES, CODALEMA, LOFAR and AERA [62, 63, 64, 65].

A filter amplifier in the calibration setup is shown in Fig. 5.3. Its design is based on the filter board used at the AERA experiment. Therefore, it is equipped with 2 inputs via SMA connectors, one for each antenna channel, and 4 BNC outputs, originally for the two channels with low and high gain of AERA. Since Tunka-Rex has a single amplification stage, two of the outputs are dummies and only channels 2 and 4 are used for input 1 and 2, respectively. The filter amplifier is supplied externally with 12 V from the cluster center, where it is located, and applies a bias voltage of 6 V to the input cable for the low-noise amplifier.

Details on the design can be found in Ref. [95]. There, stability, good linearity and a moderate noise temperature were shown, adding a negligible 23 K to the system noise, due to the effective damping by the gain of the LNA (see Sec. 5.3).

The measurement of the scattering parameter of the filter amplifier with the network analyzer is straightforward. Both ports of the filter amplifier are matched to 50 Ω, similar to the transmission lines it is connected to in Tunka-Rex and the ports of the network analyzer. Therefore, calibration conditions are similar to the operating conditions. Thus,

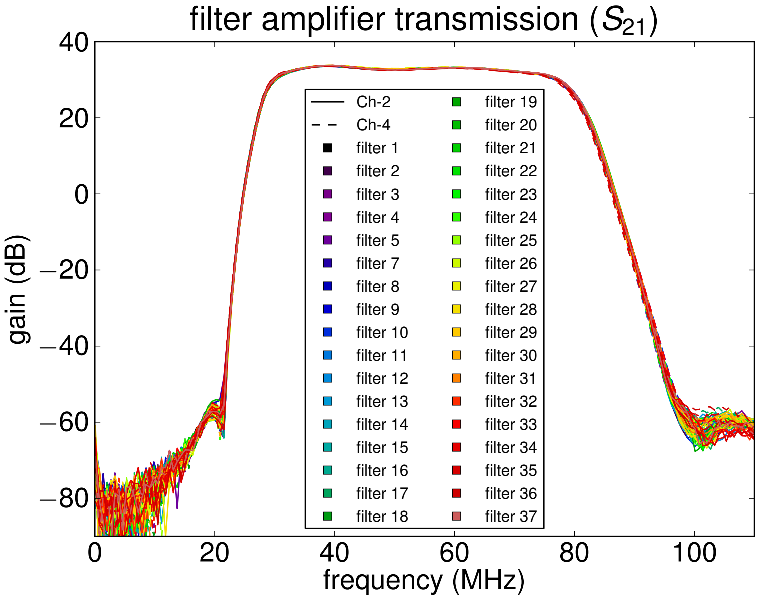

Figure 5.9: Forward gain of the filter amplifiers. They amplify signal components inside the design band by 32 dB and suppress signal components outside the design band by 60 dB, with a very steep falloff. The color code is the same for all plots for the filter amplifiers in this section.

the forward transmission S_{21}, directly represents the response function of the filter amplifier, which is required for the signal reconstruction in Tunka-Rex

In Figs. 5.9 and 5.10, the resulting forward gain and group delay of all filter amplifiers are shown. The gain illustrates the filter amplifiers purpose. Signal components with frequencies inside the passband are amplified by about 32 dB, corresponding to a factor of 40 in amplitude and varying by 0.2 dB at each frequency over the whole production series. Signal components with frequencies outside the passband are suppressed by 60 dB, i.e., the amplitude is damped by a factor of 1000. On the upper edge of the realized band the fall off begins a bit prematurely, so the gain already declined to 26 dB at 80 MHz. Therefore, the realized band ends slightly below the design band, already at 76 MHz. The measurement uncertainty on the gain in the design band is around 0.05 dB. Frequencies outside the design band, with significantly larger measurement uncertainty on the gain, are digitally cut during signal reconstruction.

The phase shift is in good approximation linear. Therefore, signal forms and signal-to-noise ratios are roughly conserved. The corresponding group delay varies only by several 10% around a mean of 80 ns inside the realized band. The group delay is measured with a precision of about 2 ns. No significant production fluctuations of the group delay are visible, which exceed the precision of the measurement.

Due to good impedance matching of the filter-amplifier ports to 50 Ω, the input

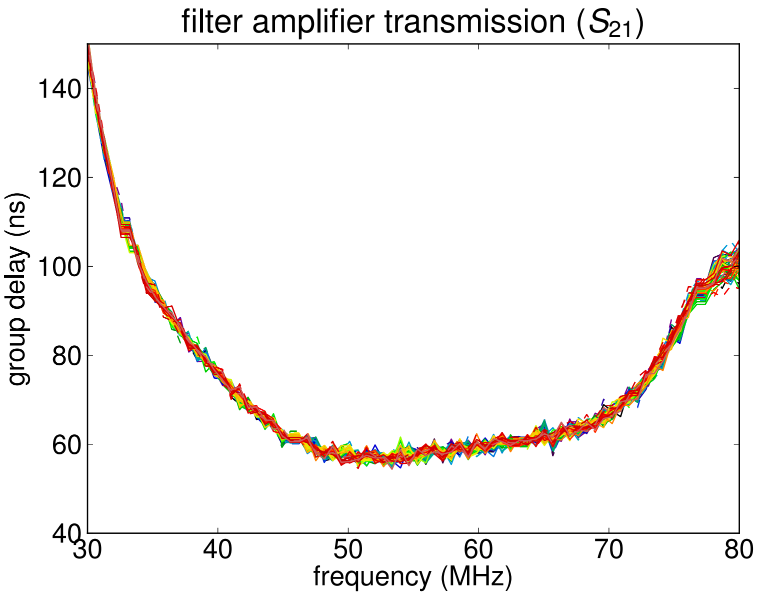

Figure 5.10: Group delay of the filter amplifier in the Tunka-Rex design band. A signal peak is delayed by about 80 ns by the filter amplifier.

reflection S_{11}, shown in Fig. 5.11, remains below $-10\,\mathrm{dB}$. For the same reason, the scattering parameters S_{22} and S_{12} are only of minor relevance. They were exemplarily measured for a few filter amplifiers and found to be below $-10\,\mathrm{dB}$.

Digitization

The last stage of the signal chain is the digitization. For the digitization, existing data acquisition boards from Tunka-133 are used, located in the cluster centers. The boards are based on the commercially available AD9430 flash analog-to-digital converter (ADC). The ADCs have a sampling rate of 200 MHz with 12 bit depth.

In the simplest case, with a flat response in frequency space, the ADC transforms voltage U to ADC counts n_{ADC}, independent of frequency

$$n_{\mathrm{ADC}} = c_{\mathrm{ADC}} \cdot U + b_{\mathrm{ADC}}. \tag{5.14}$$

With a 12 bit ADC, the counts range from 0 to 4095 and the baseline is $b_{\mathrm{ADC}} = 2047.5$. The designed upper and lower bound of the voltage are $0.35\,\mathrm{V}$ and $-0.35\,\mathrm{V}$, corresponding to a calibration constant of $c_{\mathrm{ADC}} = \frac{4096}{0.7\,\mathrm{V}} = 5850\,\mathrm{V}^{-1}$.

However, since the boards were not included in the antenna calibration with the reference source (see Sec. 5.5), an individual calibration measurement has been performed to ensure proper signal reconstruction. Two campaigns were conducted to calibrate the digitizer boards: first, a measurement with little sensitivity to frequency dependence,

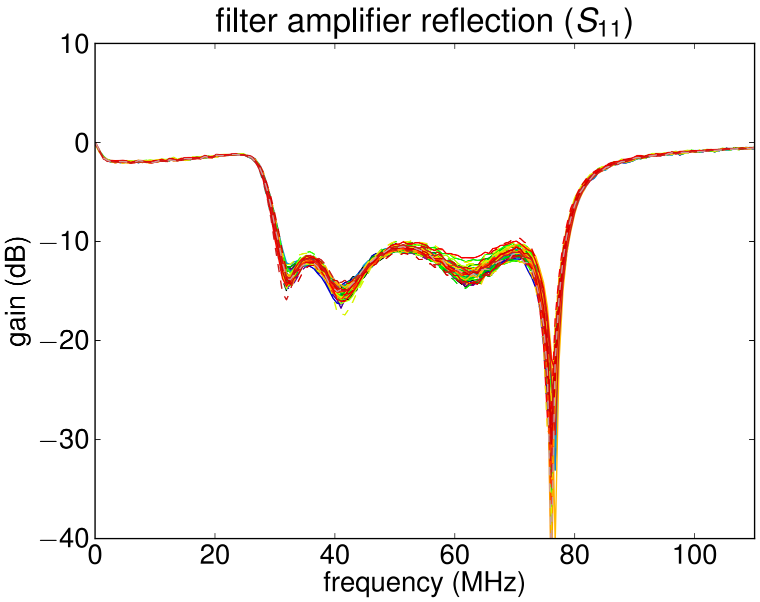

Figure 5.11: Reflection measurements for the filter-amplifier input. The filter amplifier, network analyzer and cables connected to the filter amplifier during the operation in Tunka-Rex are impedance matched, therefore reflections are generally small.

to roughly check the calibration constant, and then, a frequency-dependent one, after significant deviations to the design were found.

First, an overall check of the calibration constant was performed with the battery-operated, portable signal generator RSG 1000, also used in the calibration with the reference source (see Sec. 5.5). The signal generator produces a pulse train signal. With an adjustable attenuator, the peak height of the output was varied. To bandlimit the signal, it is connected to a filter amplifier of Tunka-Rex, to avoid aliasing due to the sampling rate of 200 MHz of the digitizers. To determine the mean peak voltage for different levels of attenuation, it was measured with an oscilloscope.

Then, the signal generator plus filter amplifier, with known peak height of the output signal, was connected to the digitizer boards of the antenna stations with IDs 15, 16 and 6 to exemplarily measure the corresponding output of the data acquisition. In Fig. 5.12, the resulting output is shown for one antenna station, as well as the expected output from design specifications. The best fitting calibration constant was found to be $c_{\mathrm{ADC}} = 3871.2\,\mathrm{V}^{-1}$, instead of $5850\,\mathrm{V}^{-1}$. The voltage conversion of the implementation realized in the digitizer boards significantly differs from the expected conversion according to the design specifications.

Because of the deviation, a second calibration campaign was conducted, to determine the frequency dependent response of the digitizers. A calibrated signal generator of the

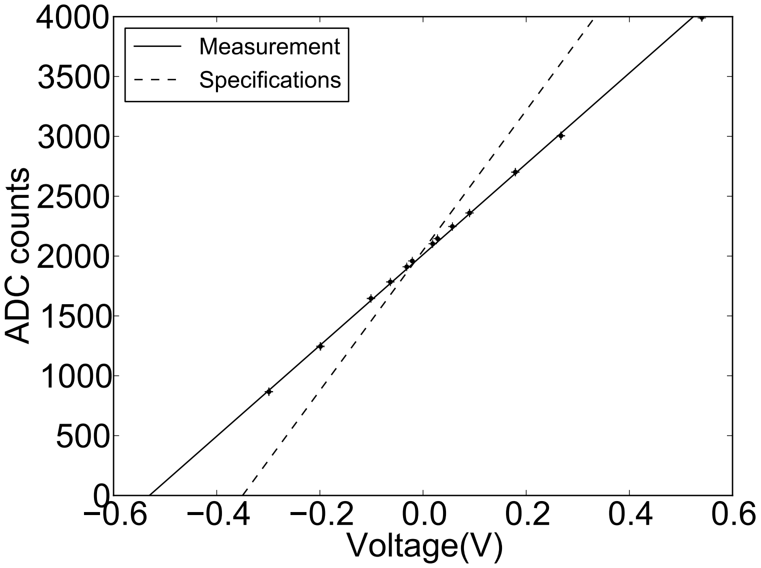

Figure 5.12: Peak voltage fed to the digitizer boards versus recorded peak ADC counts. Although the digitizers are linear, their conversion differs significantly from the specifications.

type Tecktronix AFG 3252 was connected directly to the digitizer board of station 15 to feed a sine-wave signal. Since the signal contains only a single frequency, a filter for bandlimiting is not needed in this measurement. Traces were recorded with signal frequencies from 18 MHz to 79 MHz in steps of 3 MHz, all with an amplitude of 0.25 V.

In the recorded traces, sine waves with the same frequency as fed to the input were recovered, confirming the linearity of the ADCs. The peak ADC counts at each frequency, corresponding to the 0.25 V measurement are shown in Fig. 5.13. The second measurement confirms the average value determined by the first calibration with the pulse train generator, and reveals a slight frequency dependence.

This frequency dependence can be inverted during signal reconstruction, using scattering parameters, as for the other electronics, by introducing a forward response S_{21}^{ADC} for the digitizers. The response was normalized to the designed voltage range of -0.35 to 0.35 V to convert ADC counts to voltage via Eq. 5.14 with the originally designed calibration constant $c_{\mathrm{ADC}} = 5850\,\mathrm{V}^{-1}$

$$S_{21}^{\mathrm{ADC}} = \frac{n_{\mathrm{ADC}}^{\mathrm{meas}}}{n_{\mathrm{ADC}}^{\mathrm{design}}} \tag{5.15}$$

The phase of the response cannot be measured this way. However, a far deviation from a linear phase would have lead to disagreement between the sine and the pulse train calibrations due to significant dispersion of the pulses. Since any linear phase conserves signal shape and only shifts them homogeneously in time, the phase is set to a constant, arbitrary value of 0.

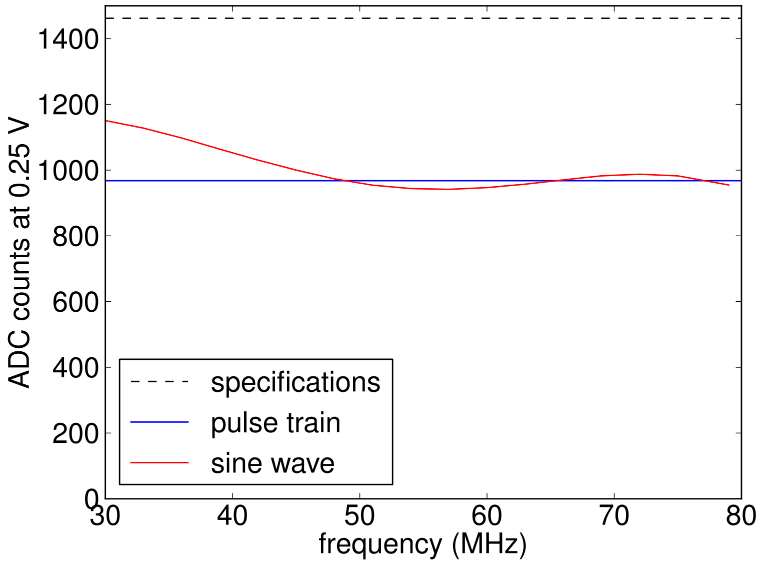

Figure 5.13: Response function of the digitizer boards. Two calibration measurement were performed: First with a peak generator (Fig. 5.12), sufficient to determine a mean value for the voltage conversion and second, with a sine generator, as a function of frequency.

With the ADCs as the last part, the signal chain, from the low-noise amplifier, over the cable, to the filter amplifier and ADCs, is calibrated. The transition of the signal from voltage to ADC counts is fully described. The last step, the calibration of the bare antenna, to describe how the radio signal is received by the antenna, and thus transformed to a voltage, is described in the next sections.

5.4 Antenna parameters of the SALLA

An antenna is a structure working as an interface between a guided electromagnetic wave and an electromagnetic wave in free space or vice versa. In other words, it is a device receiving electromagnetic radiation, in our case that of an air shower, and converting it to a measurable electric signal.

For the case of an air shower, the incoming electromagnetic signal can be assumed to be sufficiently far from its source, i.e., in the far-field region, and is therefore fully characterized by the time-dependent electric field vector. The response of an antenna to such an electric field depends on the incoming direction, polarization and frequency of the incoming signal. It is usually described by the gain and directivity of the antenna. Although these parameters describe an emitting antenna, antenna physics for reception and emission are equivalent according to the reciprocity theorem [112]. Consequently, antenna parameters for both cases equally describe an antenna and can be deduced from one another.

Especially if in addition to the amplitude, also the polarization is of interest, the vector effective length is a more useful quantity than the gain. These parameters and their relation to each other will be introduced in the following sections.

Gain and directivity

The most common terms to describe the emission and reception of an antenna are the directivity and the gain. The directivity D describes how the irradiated power P of the antenna is distributed over the solid angle $\Omega(\theta, \varphi)$ [113]

$$D = \frac{\mathrm{d}P}{\mathrm{d}\Omega} = \frac{S(\theta, \varphi)}{\langle S \rangle}, \tag{5.16}$$

with the Poynting vector $S = \left|\vec{S}\right|$ (not to be confused with the signal amplitude S used in other chapters of this thesis). The maximum of the directivity D_0 is a characteristic property of the antenna and describes how directional it is.

While the directivity describes how the power is distributed over the solid angle, it bears no information on the overall efficiency η of the antenna. Therefore, the gain G is introduced, the directivity multiplied by the antenna efficiency. It can be interpreted as the power emitted in a certain direction divided by the power which would be emitted in this direction by a perfect isotropic radiator. The gain can be written in terms of the electric far field $\vec{E}(r, \theta, \varphi)$ of an antenna, at the distance r in the direction θ, φ, with the relation $S = \vec{E}^2/Z_0$, where $Z_0 \approx 377\,\Omega$ denotes the vacuum impedance, and with the energy flux of a perfect isotropic radiator $S_{\mathrm{iso}} = P_{\mathrm{in}}/(4\pi r^2)$

$$G = D \cdot \eta = \frac{S(\theta, \varphi)}{S_{\mathrm{iso}}} = \frac{4\pi r^2 \vec{E}^2}{Z_0 P_{\mathrm{in}}}. \tag{5.17}$$

If the antenna is used as a receiver, the effective aperture A_{eff} describes the received power P_{rec} per incoming energy flux S. Since the effective aperture of the perfect isotropic radiator is $\lambda^2/4\pi$ with the wavelength λ, the effective aperture can be directly related to the gain, as stated by the reciprocity theorem [114]

$$G = A_{\mathrm{eff}} \cdot \frac{4\pi}{\lambda^2}. \tag{5.18}$$

For these considerations, it is assumed that the polarization in the receiving case is matched to the emitting case. Otherwise, the different components of polarization have to be treated separately. Furthermore, gain and effective aperture generally depend on the incoming direction and frequency.

To determine the gain for the SALLA, the antenna-simulation code NEC2 [115] was used to simulate the electric far field $\vec{E}$ of the passive antenna structure above marshy ground (as expected in the Tunka valley). The gain can be retrieved from $\vec{E}$ via Eq. 5.17. The configuration of the simulation is given in App. B.

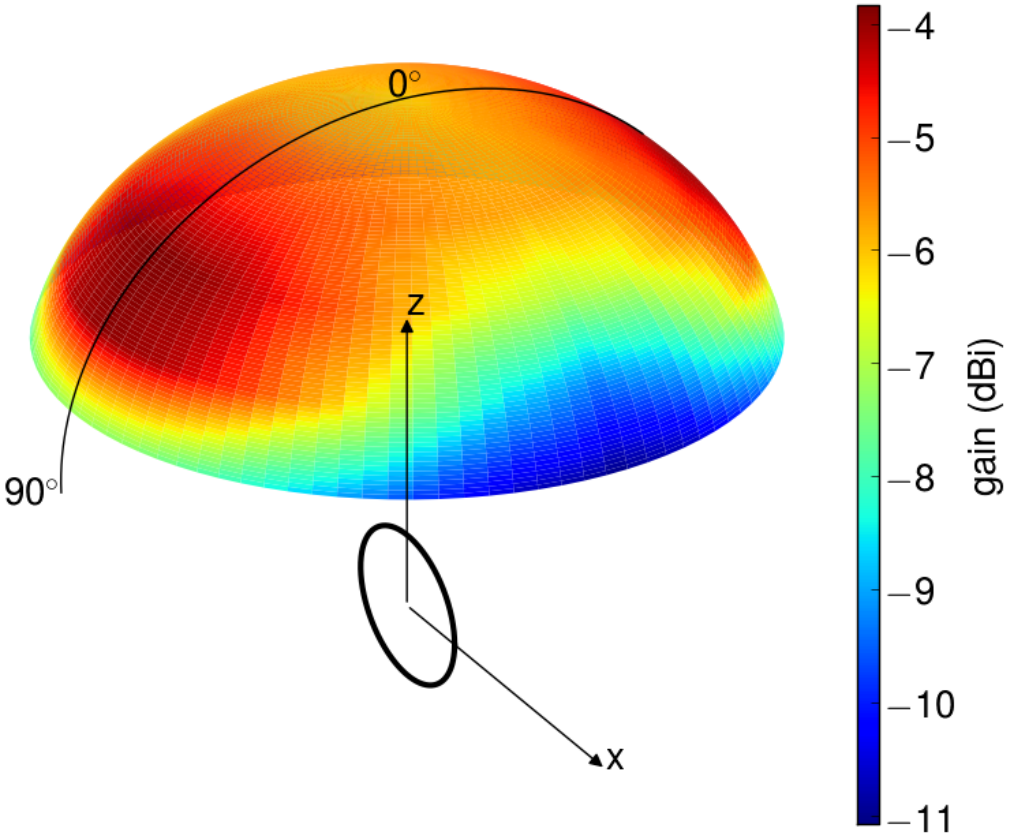

Figure 5.14: Simulated gain pattern of the SALLA at 50 MHz over marshy ground. The circle at the center indicates the orientation of the SALLA. The color encodes the gain towards the respective direction on the unit sphere up to a zenith angle of 75°.

In Fig. 5.14, the full gain pattern for a frequency of 50 MHz over marshy ground is shown. According to the simulation the SALLA has a comparatively uniform gain, covering a big fraction of the sky, up to zenith angles of about 70°. The directivity is very similar to that of a horizontal dipole in a similar height of about 2.5 m above ground. Due to the resistive load at its bottom, the gain is only about −5 dBi [4] towards the sky, roughly 10 dB lower, than for a simple dipole. However, as shown in Sec. 6.4, a higher gain would barely affect the detection threshold, which is limited by galactic background. Moreover, the load suppresses the reception of signal from below, reducing the dependence of the antenna on the ground conditions due to reflections from the ground. In Fig. 5.15, a slice of the simulated gain pattern for the SALLA is depicted for several ground conditions, showing expectedly little variation.

---

[4] Logarithmic power ratio with the perfect isotropic radiator as reference, gain $G[dBi] = 10 \cdot \log(D\eta)$.

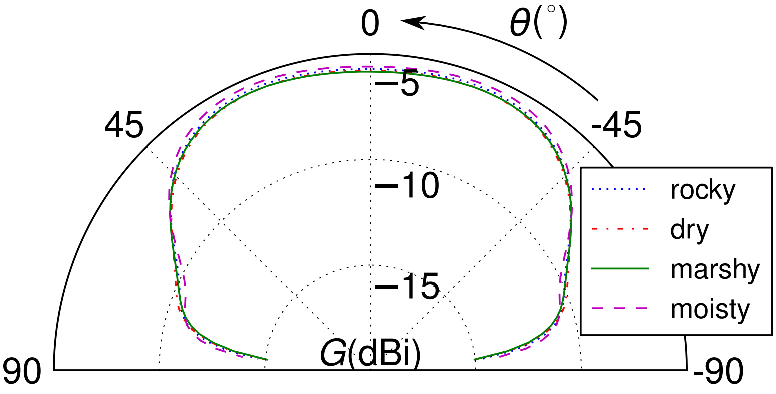

Figure 5.15: A slice along the antenna arc plane of the SALLA gain pattern simulated at 50 MHz for different grounds. Due to a resistive load towards ground, the SALLA has little dependence on ground conditions.

Vector effective length

For many applications of radio antennas, the polarization does not play an important role. For the radio detection of cosmic rays however, the reconstruction of the polarization is very common, as it was found to have a characteristic signature [57]. Therefore, instead of the gain, the vector effective length of the antenna is more commonly used, because it has the polarization incorporated more conveniently.

The vector effective length $\vec{\mathcal{H}}$ is a representation of the response function of the antenna in the frequency domain. It gives the open-circuit voltage $\mathcal{V}_{\mathrm{oc}}$ per electric field $\vec{\mathcal{E}}$, caused by an incoming radio signal with frequency ν

$$\mathcal{V}_{oc}(\nu) = \vec{\mathcal{H}}(\nu, \theta, \varphi) \cdot \vec{\mathcal{E}}(\nu) \tag{5.19}$$

Contrary to the gain, using the vector effective length $\vec{\mathcal{H}}$, the signal is handled terms of amplitudes instead of power. $\vec{\mathcal{H}}$ contains the full information for the reception of any incoming electrical field with arbitrary polarization. In case of emission, $\vec{\mathcal{H}}$ describes the electrical far field at the distance r, caused by a current I in the antenna terminals [113]

$$\vec{\mathcal{E}}(r, \theta, \varphi) = \frac{-iZ_0kI\vec{\mathcal{H}}}{4\pi r} \cdot e^{-ikr}, \tag{5.20}$$

with the vacuum impedance $Z_0 \approx 377\Omega$, the wavenumber $k = 2\pi/\lambda$ and the wavelength λ.

In Fig. 5.16, the vector effective length of the SALLA is shown, obtained via Eq. 5.20 from the simulated far field. Similar to a horizontal dipole, it is mainly sensitive to an electric field aligned with the antenna arc plane.

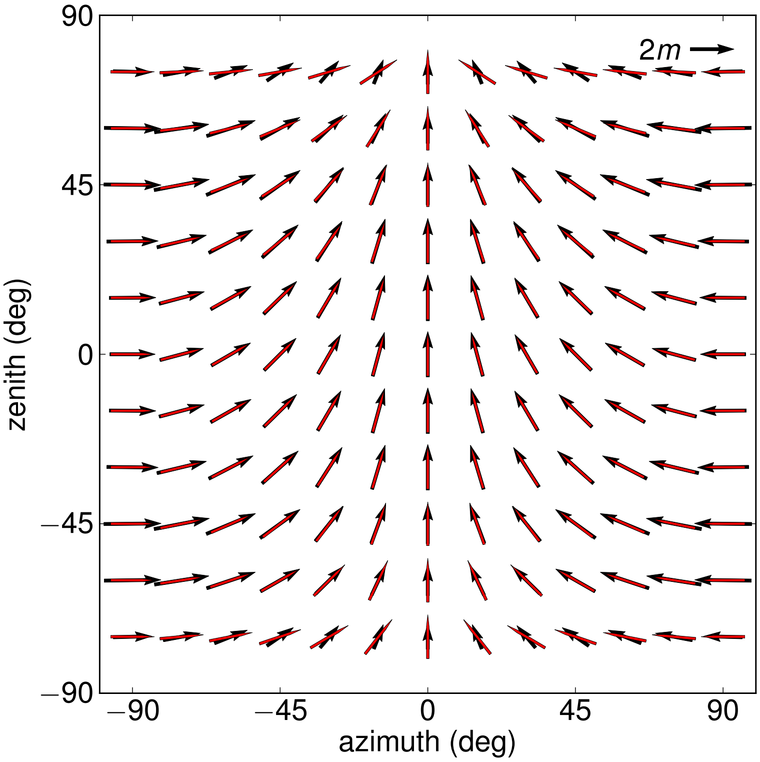

Figure 5.16: The vector effective length $\vec{\mathcal{H}}$ of the SALLA for a frequency of 50 MHz. The position of the arrows shows which incoming direction they describe. Their direction and length denote $\vec{\mathcal{H}}$ along the spherical base vectors $\vec{e}_\theta$ and $\vec{e}_\phi$. The red, headless lines indicate the orientation of the antenna arc plane. In the upper right, an arrow corresponding to a $|\vec{\mathcal{H}}| = 2\,\mathrm{m}$ is shown for scale.

5.5 Antenna calibration with a reference source

While the vector effective length $\vec{\mathcal{H}}$ can be obtained theoretically, there are limitations on how well the antenna can be modeled. A calibration measurement on the other hand is very cumbersome, since it requires a well defined signal source, and has to be performed for all relevant frequencies, incoming directions and polarizations. Therefore, a combined approach was pursued for the calibration of the Tunka-Rex antenna station, roughly following the concept of the LOPES calibration [116]. The directivity and phase of the vector effective length are obtained from simulations. A calibration with a reference source is then performed to obtain the correct scale for all frequencies and check the directivity.

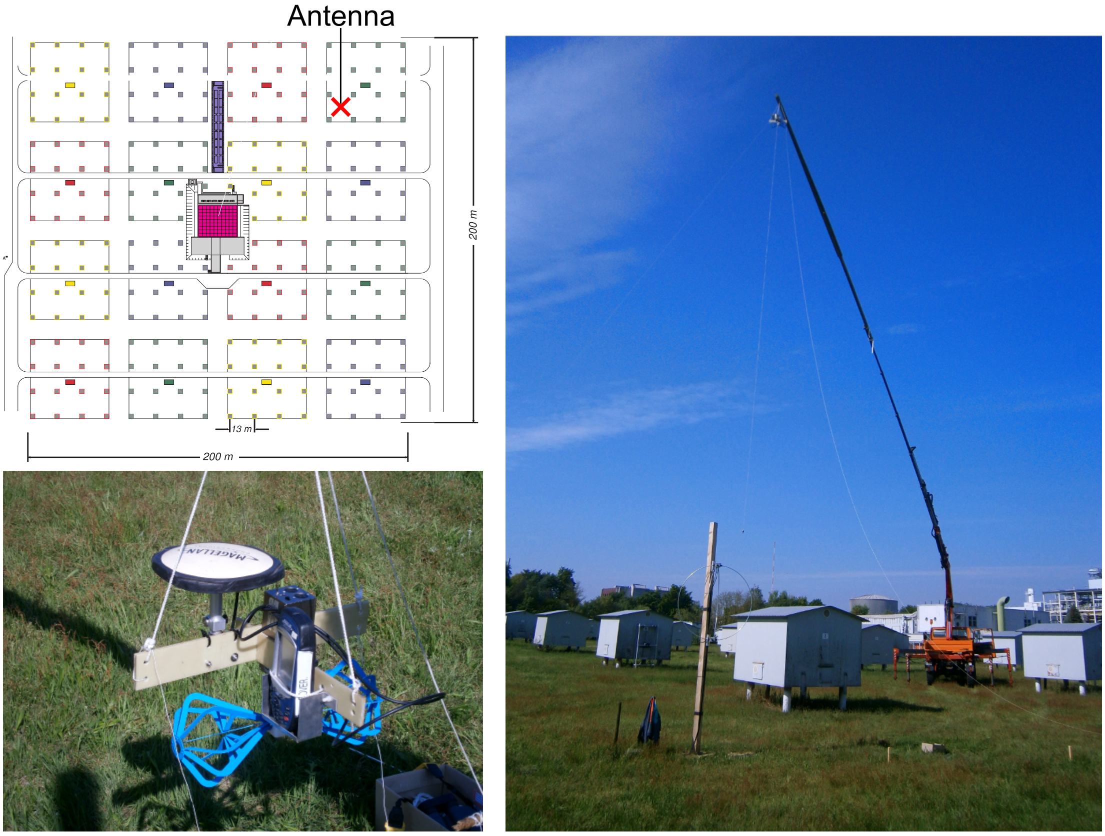

Figure 5.17: **Top:** Map of the KASCADE field. The position of the Tunka-Rex antenna station is indicated, which was used for the calibration. Square markers indicate the KASCADE detector stations. Fig. adapted from Ref. [44]. **Bottom:** Support frame for the reference source. It also holds one receiver of a differential GPS and strings to align and stabilize the antenna during the measurement. **Right:** Preparation of the calibration measurement. The crane holds the reference source above the SALLA, while two people align it via the attached strings. The distance to the antenna is at least 10 m, precisely determined with the differential GPS.

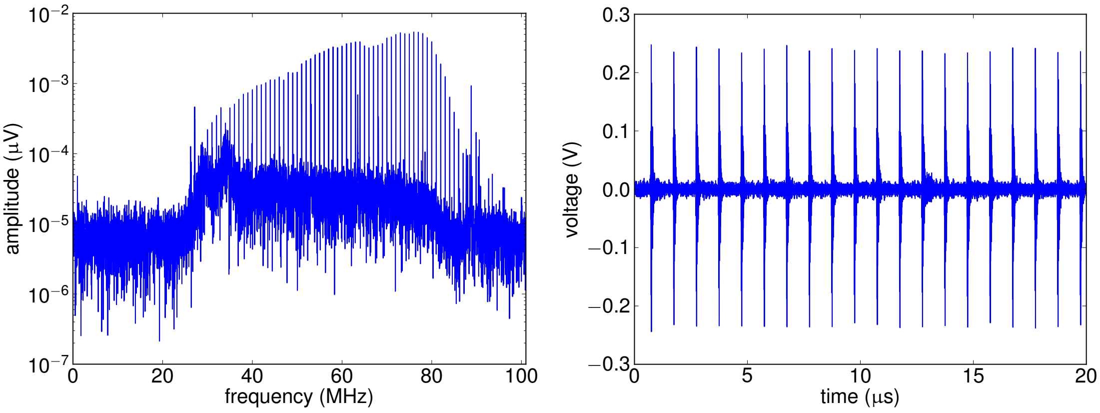

(a)

(b)

Figure 5.18: (a)The amplitude spectrum of the reference source is a frequency comb, consisting of amplitude peaks with 1 MHz spacing and known magnitude. (b)The signal in the time domain is a pulse train with 1 µs spacing. The frequency comb of the reference source extends to 1 GHz, but due to the analog filter of the Tunka-Rex antenna station only frequencies within 30 to 80 MHz are visible.

The reference source

The used reference source is the commercially available VSQ 1000 reference source, shown in Fig. 5.17 bottom, as mounted for the calibration. It is manufactured and calibrated by Schaffner Electrotest GmbH (now Teseq). It consists of the biconical antenna DPA 4000 with a length of 40 cm and the battery-operated signal generator RSG 1000.

The signal generator generates a frequency comb in the range of 30 to 1000 MHz with a selectable spacing of 1, 5 or 10 MHz. For the calibration measurement, the 1 MHz configuration was used exclusively. Thus, the signal in the frequency domain will contain a peak of known height at the full MHz steps. In the time domain, the resulting signal is a pulse train with 1 µs spacing. The reference antenna was originally designed for 300 to 1000 MHz, but is certified down to 30 MHz. Below 100 MHz, the emitted power declines quickly, being barely measurable in the used setup at the lower edge. In Fig. 5.18, a recorded example trace and amplitude spectrum are shown.

The directivity of the biconical antenna is close to a cosine, like for a dipole antenna in free space. Because of the flat directivity around the main direction, errors due to misalignment are small. The emitted signal is polarized linearly along the antenna axis.

The calibration values are given in terms of effective field strength at each frequency and can be found in the calibration sheet in App. C. The reference antenna was calibrated in a semi-anechoic chamber in 3 m distance to a calibrated receiving antenna. By varying the height of the calibrated receiving antenna, the maximum amplitude at this lateral distance is determined. This calibration setup is called ”free field conditions” and reflections from the ground are maximized this way. However, for the application in air shower measurements, the calibrated field strength was recalculated to a distance of 10 m and free space conditions, i.e., only taking the direct emission into account, without reflections. These conditions fit the needs of cosmic-ray measurements better, because the direct radio signal usually dominates and also simulation of radio emission from air showers are evaluated for free space conditions.

The two-sigma uncertainty on the calibration values is given by the manufacturer to 2.5 dB, corresponding to a 16% one-sigma uncertainty on the amplitude. This includes uncertainties for the extrapolation to the far field at 10 m (calculated using a dipole model).

Calibration setup

Due to available infrastructure and experience the calibration was performed at KIT, Germany. A Tunka-Rex antenna station was deployed on the former KASCADE [44] field, co-located with the LOPES experiment [62]. The position of the SALLA antenna is indicated in Fig. 5.17 top. It was put on a wooden pole, at the same height and with the same alignment versus the magnetic north as in Tunka-Rex. The full, original analog signal chain, consisting of low-noise amplifier, cables and filter amplifier were mounted to it. The only remaining difference in the analog antenna structure, affecting the reception, is the ground. However, the ground has little impact on the SALLA, as discussed in Sec. 5.7.

The original data-acquisition system (DAQ), including the digitizers, could not be brought to KIT. instead it was substituted by a calibrated oscilloscope of the type HP Agilent 54853A. Thus. the calibration is almost end-to-end, except for the DAQ. The DAQ of Tunka-Rex was calibrated individually (see Sec. 5.3).

The oscilloscope HP Agilent 54853A has an analog bandwidth of 2 GHz and was set to a sampling frequency of 2 GHz. The recorded trace contains 131072 samples, resulting in a length of about 66 µs.

A differential GPS was used to measure the distance and relative position of the reference source to the antenna station. It consists of 2 GPS receivers with antennas. One was positioned on the roof of a close-by container and the other was put in a support frame together with the reference source (see Fig. 5.17 bottom). It records each second the relative positioning of the two receivers with an accuracy of 0.3 m.

The calibration was performed on May 8th 2013. The environmental conditions on that day were wet ground with sunny weather and temperatures raising from 16 to 20 °C during the calibration measurement.

Calibration procedure

The calibration procedure is as follows: A crane was parked in 20 m distance to the SALLA. During the measurement, the engine of the crane was turned off, to avoid

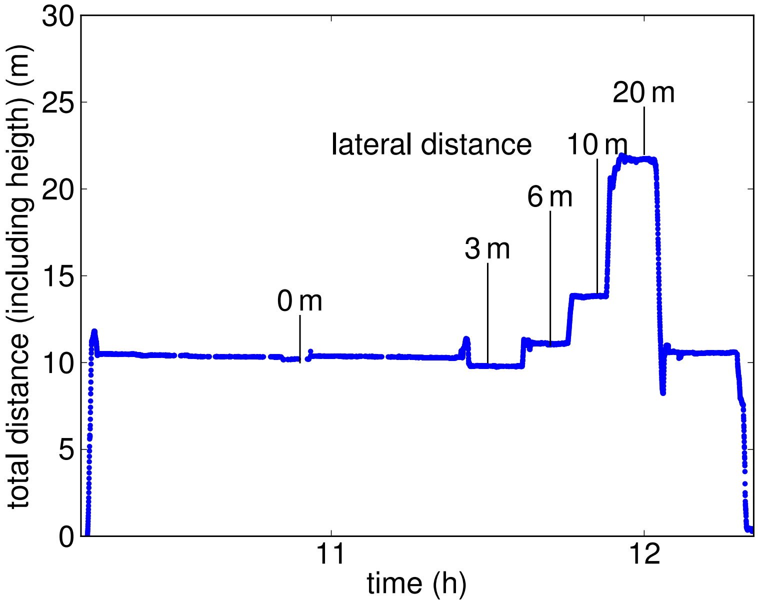

Figure 5.19: Distance between the reference source and the antenna station, measured with the differential GPS during the calibration. For times, when data was taken, the lateral distance is indicated, which corresponds to different zenith angles, since the height above ground was always about 10 m.

interference. A support frame, produced for the LOPES calibration was mounted on the crane, shown in Fig. 5.17 bottom. It holds the reference source and GPS receiver with its antenna. The recorded positioning data is later assigned to its respective measurement by the GPS time stamp. The recorded antenna-source distance during the whole campaign is shown in Fig. 5.19.

First, the reference source was put directly next to the SALLA for a reference position. Then, the source was put above the antenna in at least 10 m distance and aligned along one antenna channel with strings from the ground. The time was noted and multiple measurements were taken for that position.

Besides the measurement with the source directly above the antenna, it was also displaced laterally to measure at different zenith angles. For these measurements, the reference source (and polarization) was always aligned along the channel perpendicular to the axis of lateral displacement, i.e., with the main direction of the reference source pointed towards the aligned channel. Measurements were taken for lateral distances of 0 m (directly above the antenna), 3 m, 6 m, 10 m, and 20 m, all in about 10 m height above the antenna level. The corresponding zenith angles relative to the SALLA were 0°, 20°, 34°, 49° and 68°, respectively. They were determined with the data of the differential GPS.

Evaluation

The output of the measurements described in the last section are traces and their Fourier transforms, as shown in Fig. 5.18. To obtain the vector effective length, the electric field amplitudes of the reference source were compared to the voltage amplitudes of the calibration measurement. To obtain electric field amplitudes from the effective field strengths given by the calibration sheet (see App. C), the values simply have to be multiplied by $\sqrt{2}$.

The voltage amplitudes $\mathcal{V}(\nu = k) = \mathcal{V}_k$ can be obtained from the discrete Fourier transform of the trace V_n with N entries by normalizing it properly

$$\mathcal{V}_k = \frac{2}{N} \sum_{n=0}^{N-1} V_n \cdot \exp(-i2\pi kn/N). \tag{5.21}$$

Since the trace is real valued, it is fully described by the coefficients corresponding to the positive frequencies. Therefore, k is an integer either from $[0, N/2]$ if N is even or $[0, (N-1)/2]$ if N is odd. With the sampling frequency ν_s, k corresponds to the frequency

$$\nu = \frac{k\nu_\mathrm{s}}{N}. \tag{5.22}$$

While commonly used libraries to calculate discrete Fourier transforms, like *FFTW* [117], usually return only the sum of Eq. 5.21, the normalization is necessary in order to interpret the Fourier coefficients as voltage amplitudes of single frequency components.

Each peak of the comb spectrum can be described by a single Fourier coefficient, if the resolution is smaller than the width of the peak and the Fourier coefficient is located precisely at the right frequency (and the sampling rate is sufficiently stable). Otherwise spectral leakage artificially increases the width of the peak.

With a width below 10 kHz, which is the resolution achieved with the recorded traces, the first condition is fulfilled. To calculate the Fourier coefficients at the precise position of the peaks, i.e., the full MHz frequencies, the traces have to be truncated properly. According to Eq. 5.22, the trace length, in terms of samples, has to be an integer multiple of $\nu_\mathrm{s}/\Delta\nu$ for the Fourier coefficients to be located in certain intervals of frequency $\Delta\nu$. With a sampling frequency of $\nu_\mathrm{s} = 2\,\mathrm{GHz}$ and a required spacing for the Fourier coefficients of $\Delta\nu = 1\,\mathrm{MHz}$, the trace length has to be truncated to a multiple of 2000 samples. The largest multiple of 130000 samples was chosen to minimize the statistical uncertainty. An enlarged part of the spectrum from the truncated trace is shown in Fig. 5.20. As intended, the peaks of the frequency comb are described by a single point.

Results

The resulting spectrum $\mathcal{V}(\nu)$, represents the voltage amplitudes for the recorded traces. Following Sec. 5.1, the open-circuit voltage $\mathcal{V}_\mathrm{oc}$ of the bare antenna can be obtained by dividing $\mathcal{V}(\nu)$ by the remaining response of the signal chain, determined in Sec. 5.3

$$\mathcal{V}_\mathrm{oc}(\nu) = \frac{\mathcal{V}_\mathrm{out}(\nu)}{S_{21}^\mathrm{filter} S_{21}^\mathrm{cable} S_{21}^\mathrm{LNA} \rho}. \tag{5.23}$$

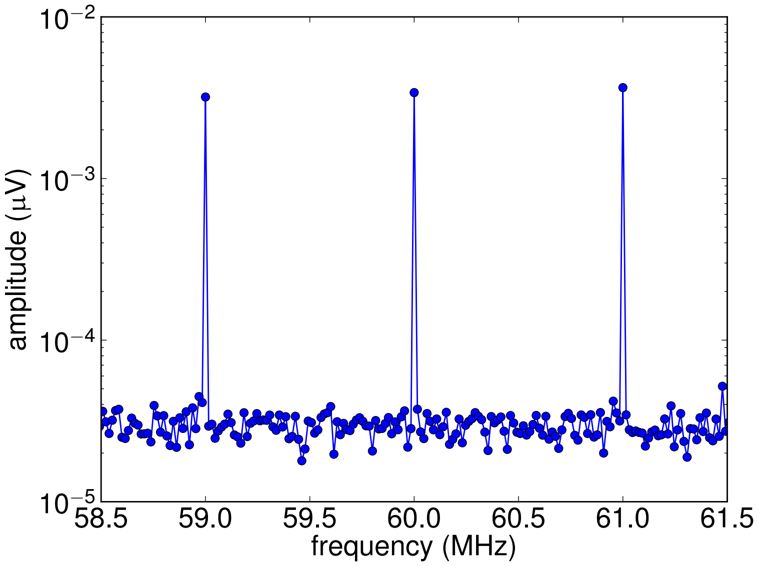

Figure 5.20: Zoom into the recorded spectrum of a trace, which is used for calibration. By properly truncating the trace, the Fourier coefficients are located directly on the full MHz peaks and spectral leakage is avoided.

From a formal point of view, when the antenna receives a signal, the electrical field is projected on the vector effective length of the antenna. Therefore, in general, at least two linearly independent measurements are necessary to invert the projection. But with the source aligned with one channel, there is practically only a single measurement, with only little signal in the second channel, originating from crosstalk and misalignment.

To simplify the inversion and enable it with a single measurement, the knowledge about the direction of the vector effective length, can be exploited. The calibration measurements confirm the dipole antenna-like polarization pattern of the SALLA, which was obtained from simulations (see Sec. 5.4). The SALLA has maximum sensitivity for a horizontal polarization in the antenna-arc plane and minimum sensitivity for a polarization perpendicular to the antenna-arc plane.

Using the polarization axis of maximum sensitivity $\vec{p}$ as the direction of the vector effective length $\vec{\mathcal{H}}$, with absolute value $\mathcal{H}$, the received voltage for a single antenna channel (see Eq. 5.19) becomes

$$\mathcal{V}_{\mathrm{oc}}(\nu) = \mathcal{H}(\nu) \cdot \vec{p} \cdot \vec{\mathcal{E}}(\nu). \tag{5.24}$$

The electric field $\vec{\mathcal{E}}(\nu) = \vec{\mathcal{E}}_{\mathrm{ref}}(\nu) \cdot r_{\mathrm{ref}}/r$ can be obtained from the calibration values of the reference source $\vec{\mathcal{E}}_{\mathrm{ref}}$ at a distance of $r_{\mathrm{ref}} = 10\,\mathrm{m}$ and the measured distance to the antenna under test r. Because the reference source was aligned with one antenna channel, $\vec{\mathcal{E}}$ is also aligned with $\vec{p}$ for this channel and Eq. 5.24 can be solved using absolute values

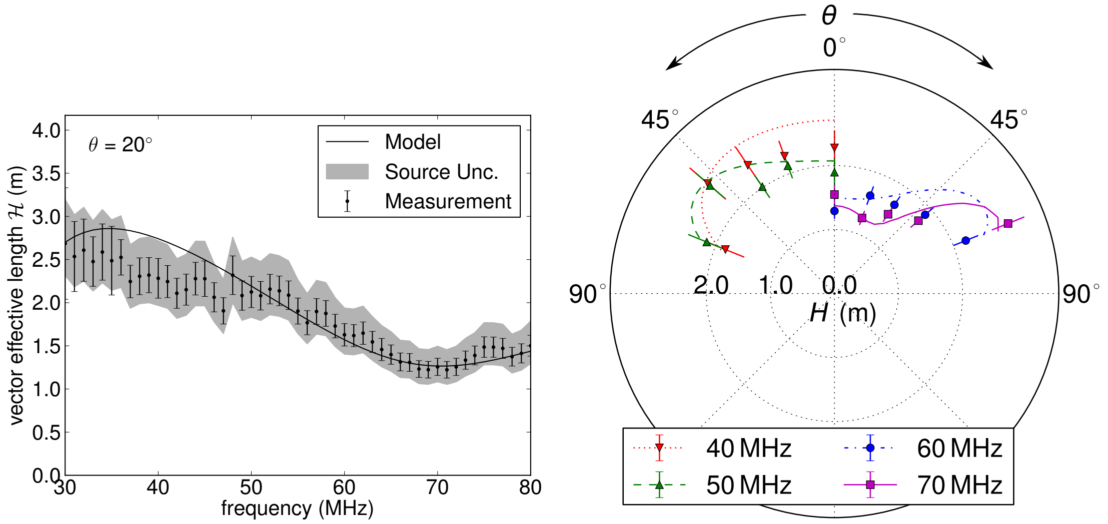

(a) (b)

Figure 5.21: Comparison of the vector effective length $\mathcal{H}$ from the calibration with a reference source and an antenna simulation, (a) as a function of frequency for one zenith angle θ and (b) as a function of zenith angle for several frequencies. The different frequencies in (b) are distributed over 2 quadrants for illustration. The errorbars indicate uncertainties from statistical fluctuations, alignment, positioning, temperature and ground conditions. The gray band indicates the calibration uncertainty of the reference source.

$\mathcal{E}_{\mathrm{ref}} = |\vec{\mathcal{E}}_{\mathrm{ref}}|$

$$\mathcal{H}(\nu) = \frac{r \cdot \mathcal{V}_{\mathrm{oc}}(\nu)}{r_{\mathrm{ref}} \cdot \mathcal{E}_{\mathrm{ref}}(\nu)}. \tag{5.25}$$

Thus, $\mathcal{H}$ can be determined with $\mathcal{V}_{\mathrm{oc}}$ (see Eq. 5.23) and r, which were measured during the calibration campaign, and the electric field strength of the reference source in terms of amplitudes $\mathcal{E}_{\mathrm{ref}}$, which can be obtained from the calibration sheet (see App. C). With the direction $\vec{p}$ of the vector effective length from an antenna simulation, $\vec{\mathcal{H}}$ can be fully determined

$$\vec{\mathcal{H}}(\nu) = \mathcal{H}(\nu) \cdot \vec{p}. \tag{5.26}$$

Since the phases of the electric field from the reference source are unknown, only the absolute value of $\vec{\mathcal{H}}(\nu)$ can be obtained with this method. For the phases, the values from the antenna simulation are used.

In Fig. 5.21, the obtained values for the vector effective length are compared to the ones expected from the antenna simulation. In App. A.2, additional results from the calibration measurements are shown and compared to the antenna simulation.

In Fig. 5.22, the ratio of vector effective lengths from the calibration measurements and the antenna simulation is shown for all zenith angles and relevant frequencies. Overall,

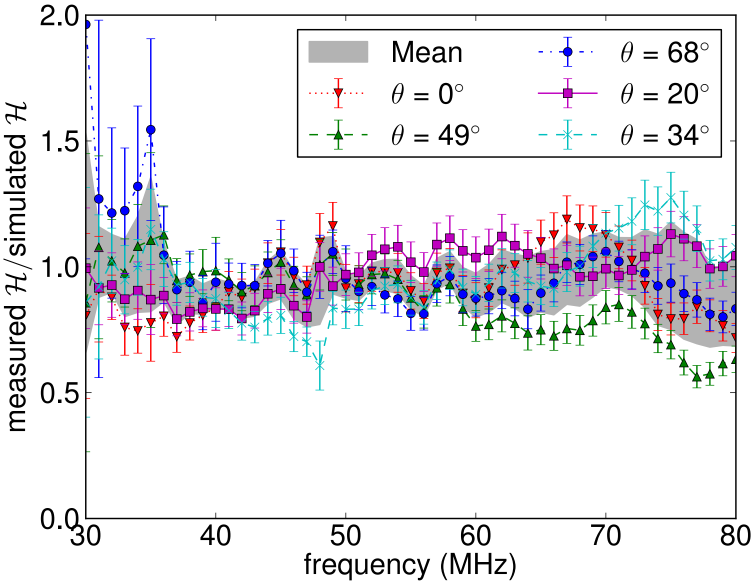

Figure 5.22: Relative deviation of measured and simulated vector effective length for all frequencies and measured zenith angles. The gray band indicates the mean and standard deviation. For the calibration, the simulated antenna pattern is normalized to the mean at each frequency.

the simulation approximately fits to the calibration results on an absolute scale. The measured vector effective length is on average 6% lower than the simulated one, well within the uncertainties for the calibration of the reference source alone. However, for this particular measurement of the bare antenna, additional systematic uncertainties have to be considered, e.g., several 10% from the measurement adapter for the low-noise amplifier. As explained in Sec. 5.7, these uncertainties cancel for the signal reconstruction.

The standard deviation of measurements at different zenith angles relative to the simulation (Fig. 5.22) at constant frequency is 12% on average. This is later used to estimate how well the simulated antenna pattern describes the real one. At the low frequencies, statistical fluctuations of the measurements tend to be higher due to the declining signal of the reference source. In the analysis of Tunka-Rex events, the frequencies below 35 MHz are cut, because interferences are regularly observed there (Sec. 6.1).

For the amplitude reconstruction of Tunka-Rex measurements, the simulated antenna pattern is frequency-wise normalized to the mean over the calibration measurements at different zenith angles. Consequently, the angular dependence and phase from the simulation is combined with the amplitude scale of the calibration with the reference source.

5.6 Cross-calibration with LOPES and LOFAR

Similar calibrations with the same reference source were performed for the LOPES [116] and LOFAR [2] experiments. While the calibration for the LOPES experiment was already performed in 2005, it was misinterpreted at first: the free-field calibration values available at the time were mishandled for free-space values. Since free-field conditions include reflections from the ground, the difference to free space conditions can be up to a factor of 2 in amplitude. After obtaining the proper free-space calibration values for the reference source from the manufacturer, this issue could be resolved in the framework of this work. This was done in direct cooperation with the LOPES collaboration and lead to an update on the amplitude scale of the LOPES experiment, published in Ref. [1].

The LOFAR experiment was calibrated in 2014, also in the context of this work, with the goal to have a another experiment with a consistent radio amplitude scale. Additionally, a calibration based on the galactic background was performed for LOFAR, as their antennas are completely dominated by the galactic background, suffering very little internal noise (Tunka-Rex has about equal contributions from galactic background and internal noise). The two calibration methods, via reference source and galactic background, were found to be consistent, hinting towards the validity of the calibration with the reference source and the calibration of the reference source itself. If AERA and CODALEMA will calibrate their antennas using the same reference source too, all contemporary radio experiments in the 30-80 MHz band will have a consistent radio-amplitude scale.

To check whether the signal reconstruction of Tunka-Rex, LOPES and LOFAR is consistent as well, the signal of the reference source was reconstructed with the software also used for air shower events in the individual experiments. Peaks of the resulting traces can be seen in Fig. 5.23, and their frequency spectra in Fig. 5.24, also with the calibration data indicated.

The reconstructed measurements of all three experiments agree within uncertainties on the total amplitude height and the frequency spectrum. For Tunka-Rex, the uncertainties on the calibration scale in comparison to LOPES and LOFAR are 6% from the temperature during the calibration and 3% from the source positioning and alignment, as discussed in Sec. 5.7. Additionally, for the individual recorded traces further uncertainties apply, which mostly average out over multiple calibration measurements. For Tunka-Rex, these uncertainties are 12% from the zenith angle dependence of the antenna pattern. The reconstruction of Tunka-Rex, contrary to LOPES and LOFAR, was not tuned on the incoming direction of the given example trace, but on the average over measurements at multiple zenith angles. Additionally, there are further statistical uncertainties on the alignment, positioning and emission of the reference source of several percent. Consequently, the calibration of all three experiments is consistent within these uncertainties.

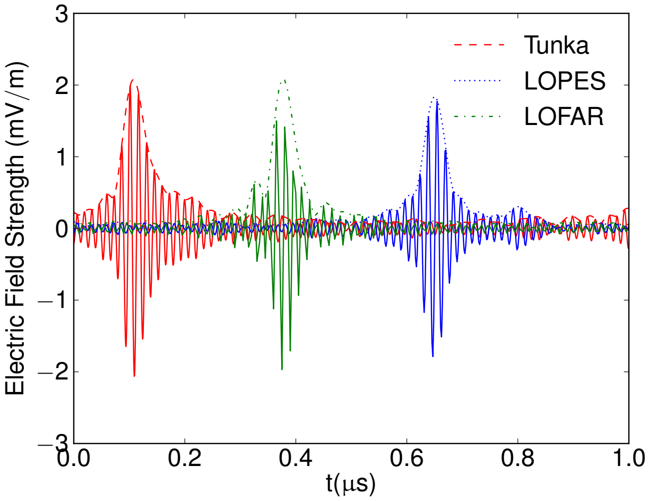

Figure 5.23: Reconstructed traces with the signal of the reference source and their Hilbert envelopes from the calibration campaigns of Tunka-Rex, LOPES and LOFAR. The signal was digitally bandlimited to the overlap of frequency bands from all three experiments. In the single traces, some statistical fluctuations remain, which average out over the multiple measurements for the calibration.

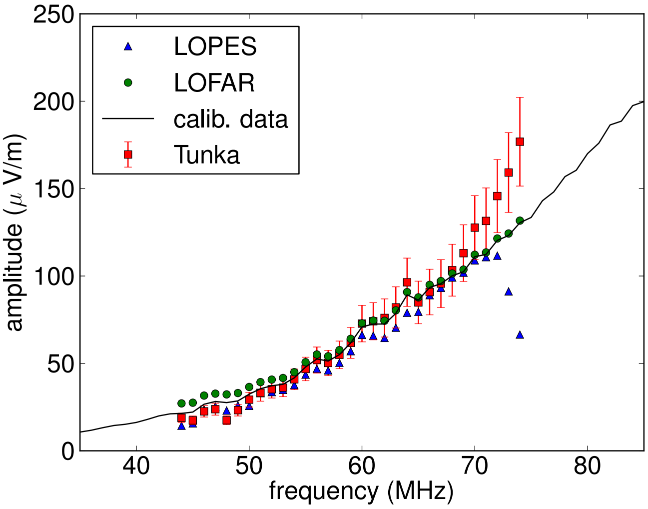

Figure 5.24: Frequency spectrum of the traces in Fig. 5.23 and the data from the calibration sheet. The spectrum was digitally cropped to the overlap of frequency bands from all three experiment. Differences to the calibration data remain due to statistical fluctuations and uncertainties in the reconstruction of individual traces, indicated for Tunka-Rex.

5.7 Uncertainties for the amplitude reconstruction

There are several sources of measurement uncertainties for the reconstruction of amplitudes with Tunka-Rex. The uncertainties can be divided into three categories with different correlations: Fully uncorrelated antenna-to-antenna fluctuations, uncertainties varying from event-to-event, connected to time or geometry-dependent conditions, and global uncertainties on the absolute scale from the calibration.

Known antenna-to-antenna fluctuations arise from uncertainties in the production of the passive antenna structure, as well as positioning and alignment of the SALLA antenna. Event-to-event contributions are the temperature during measurement, ground conditions, shortcomings of the antenna model and crosstalks. The latter two might not be intuitively expected in this category, but belong there, since they depend on the shower geometry. Uncertainties on the absolute scale are all connected to the reference source: its calibration, positioning, alignment and temperature.

In the following, the origin and estimates of the uncertainties are explained. The uncertainty from the measurement adapter of the low-noise amplifier and the uncertainty due to noise are special cases, which are discussed at the end.

Antenna positioning and alignment

Positioning and alignment of the SALLA can only be performed with finite precision. It has to be positioned in a certain height, and oriented along a certain azimuth angle with respect to the Earth's magnetic field and zenith angle relative to the ground.

The target height is 2.93 m above ground and the estimated precision of the mounting is 5 cm. Varying the height by 5 cm in the antenna simulation, causes the reconstructed amplitude to change by 1.3% on average.

During deployment the zenith angle uncertainty was determined with a pendulum, measuring the displacement of the lower end versus the upper one over 120 cm. The resulting deviations from vertical are below 5°. Consequently, an uncertainty of 1.5% for the reconstructed amplitude is obtained from the antenna simulation.

The azimuthal alignment was performed with a compass along magnetic coordinates with an estimated precision of 5°. The amplitude reconstruction with an antenna pattern rotated by 5° results on average in a difference of 1.0% for the reconstructed amplitude.

Thus, the total amplitude uncertainty from positioning and alignment is 2.2%, obtained from the quadratic sums of single contributions.

Antenna production variations

The SALLA consists of a 120 cm antenna arc, made from aluminum, the resistive load in the lower antenna box and the low-noise amplifier in the upper antenna box. While production fluctuations of the low-noise amplifier are compensated by calibrating each amplifier individually, the production fluctuations of the passive antenna structure are not taken into account, yet. They consist of variations in the antenna arc diameter,

Figure 5.25: Temperature chamber used for the calibration measurement at different temperatures. The part under test is put inside and heated or cooled during the measurement.

estimated to be 1 cm, and variations in the load resistor, given by the manufacturer with 1%.

To determine their impact on the amplitude reconstruction, the passive antenna structure was simulated several times, varying parameters in this range. Then, the average deviation of the gain was determined, as an estimator for the expected impact on the amplitude reconstruction. Only the realized frequency band for zenith angles up to 50° was evaluated, as for the standard data analysis of Tunka-Rex (Sec. 6.3).

The resulting uncertainties on the amplitudes are 0.3% due to the load and 1.0% due to the arc radius. Adding them in quadrature, results in a total of 1.0% due to production fluctuations.

Temperature

Electric properties, especially of complicated circuits, generally depend on the operation temperature. Since the calibration took place in the laboratory at around 20 °C, it has to be checked how much the transmission parameters change at temperatures encountered during operation.

Therefore, the measurement of the forward transmission was repeated exemplarily for one low-noise amplifier (LNA), one filter amplifier and the cables in a temperature chamber at different temperatures. The covered temperatures range from −40 °C to 75 °C. The Tunka-Rex data evaluated for the further chapters was taken from October to April in the winter nights of 2012/2013 and 2013/2014, the first and second measurement

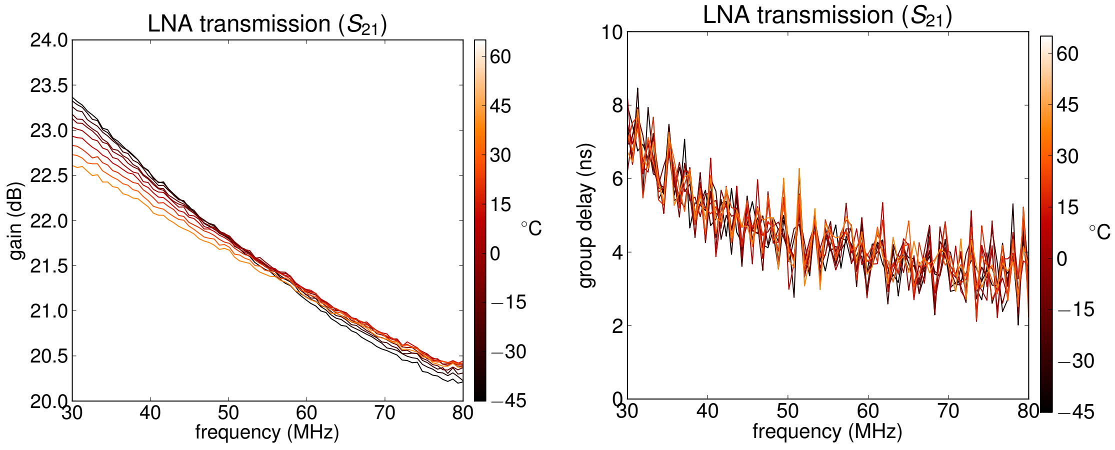

(a) (b)

Figure 5.26: (a) Gain and (b) group delay of the low-noise amplifier for different temperatures. While the gain shows a slight temperature dependence, the group delay only fluctuates within the uncertainties of the calibration measurement.

seasons of Tunka-Rex. According to the archive from a close by weather station [118], the temperature during that time period ranged between −40 °C and 0 °C. Therefore, in particular the low temperature behavior of the signal chain is relevant for this time period. For operation during day-time, possibly also in summer, with Tunka-Grande as trigger from November 2015 on, also the higher temperature behavior may become relevant.

The measurement setup is shown in Fig. 5.25 and the resulting forward transmission parameters of the LNA in terms of gain at different temperatures are shown in Fig. 5.26a. The group delay, depicted in Fig. 5.26b, remains constant within the measurement uncertainties. The gain gradually rises towards lower temperatures at frequencies below 55 MHz and slightly declines at higher frequencies. Overall, from 20 °C, at which it was calibrated to −40 °C its gain varies on average by about 0.3 dB (4% in amplitude).

The forward transmission of the 29.9 m RG213 cable is depicted in Fig. 5.8. The gain of the cable systematically rises towards lower temperatures by up to 0.2 dB (2% in amplitude), while the group delay increases by about 1 ns.

The temperature behavior of the filter-amplifier response was measured as well. However, usually the filter amplifiers are operated within the cluster centers of Tunka-133, heated to 18 to 25 °C. Therefore, they are not exposed to the cold outside temperature and the impact of the temperature can be neglected. Measurement results for the filter amplifier at different temperature are discussed in App. A.1.

Since the temperature drifts of different part are correlated, the total change in gain has to be considered. It ranges from 0.5 dB at 30 MHz, where drifts from cable and LNA

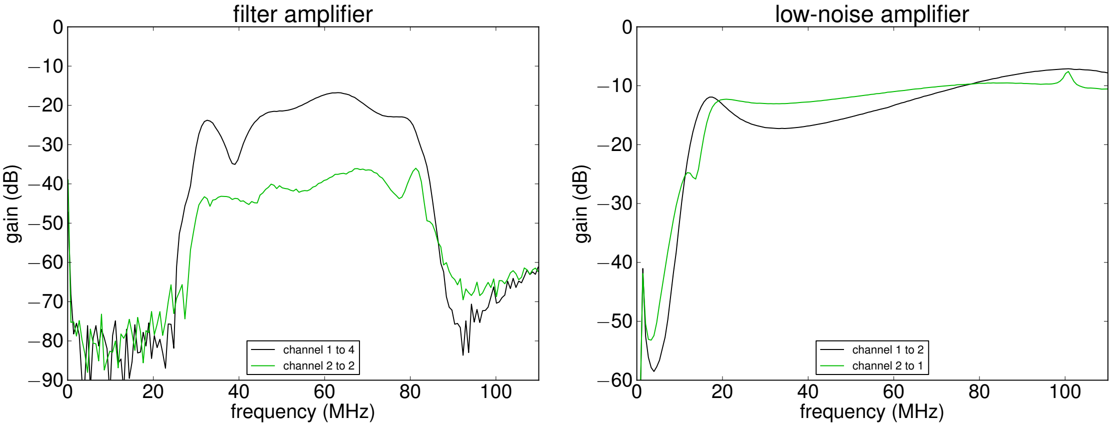

(a) (b)

Figure 5.27: Crosstalk of (a) the filter amplifier and (b) the low-noise amplifier. The gain here has to be compared to the gain for the forward transmission.

add up, to almost zero at 80 MHz, where they cancel. On average the gain changes by 0.3 dB (4% in amplitude), which is used as an estimator on the systematic uncertainty.

The passive antenna structure is assumed to have negligible temperature dependence: Its length changes in the given temperature range by several ‰. This is one order below the production fluctuations of the antenna arcs of 1 cm≙1%. The resistance of the aluminum arcs is with $\approx 10^{-3}\,\Omega$ negligible against the 390 Ω load, The resistance of the load itself varies by 50 ppm/K, resulting in several ‰. This is one order below the production fluctuations of 1%.

Crosstalk

The two channels of the LNA and the filter amplifier are place on one circuit board, very close next to each other. Therefore, the two channels are not completely decoupled. A signal in one channel is likely to cause some signal in the other channel as well, a phenomenon known as crosstalk.

To measure the crosstalk, the signal of the network analyzer is fed to one channel, but the output of the other channel is evaluated. These measurements were performed exemplarily for one low-noise amplifier and one filter amplifier.

Resulting gains are shown in Fig. 5.27. The crosstalk has to be compared to the forward gain at the respective frequency (Figs. 5.9 and 5.5). Due to the slightly asymmetric geometry of the filter, the crosstalk between input 1 and output 4 is about 20 dB stronger than between input 2 and output 2. Generally it is around −50 dB compared to the gain of about 32 dB in the realized band, thus, contributing at most 0.3% to the amplitude uncertainty.

The low-noise amplifier shows very similar responses for both channels, as expected due to its symmetric design. The crosstalk is around −35 dB relative to its gain of 22 dB, contributing at most 1.7% to the amplitude uncertainty.

For the reconstruction of the total amplitude from both channels, both crosstalk contributions add to 2% if the signals in both channels are equally large, and are negligible if the signal is mainly received by one channel. Since the alignment of the antennas in Tunka-Rex was designed to have equally large signals in both channels, an uncertainty of 2% has to be assumed due to crosstalk. Depending on the incoming direction, especially the azimuth angle, the sign of a recorded signal in a channel can flip with respect to the other channel, so the signals in both channels are either correlated or anticorrelated. Therefore, the crosstalk can both, enlarge or reduce the recorded signal amplitude by up to 2%.

Antenna model

As described in Sec. 5.5, the spread of the calibration measurements over different zenith angles of 12% is used as an estimator on how well the model describes the actual antenna pattern. Since this changes depending on incoming direction, the impact on the amplitude varies from event to event.

Ground conditions

For most antenna types, the ground conditions have a significant impact on the antenna performance due to reflections from the ground. For the SALLA however, the impact is expected to be small, since it was designed to have little sensitivity from below. To investigate the influence of the ground, several ground conditions were simulated and their response patterns were compared up to a zenith angle of 50°, as for the Tunka-133 standard analysis.

The simulated grounds vary by their conductivity and permittivity. A variety of ground conditions was chosen to cover different levels of moistness. The chosen, preset ground types in the NEC2 code were: average, dry, marshy, and ice, using marshy ground as default. The average variation of the reconstructed amplitude over these types is 2.9%

Source calibration and temperature dependence

The calibration of the reference source was performed by its manufacturer. According to the calibration report, the uncertainty for the given electric field values of the reference source is 16%. Known details on the calibration procedure are given in Sec. 5.5, as reported by the manufacturer.

The temperature dependence of the reference source adds another 6% uncertainty on the amplitude scale between temperatures of 10 to 30 °C. This range was not exceeded during the calibration. Temperature variations during Tunka-Rex measurements are considered independently (see above).

Source positioning and alignment

The distance of the reference antenna to the SALLA was measured with a differential GPS. Typically, the measurements for each zenith angle were performed within about one minute. Within this minute the GPS measurements show very little variation, in the order of 0.1 m. Additionally, the differential GPS has systematic uncertainties on the determined distance around 0.3 m. For the average distance during each measurement, both contributions add up in quadrature to 0.3 m. The resulting uncertainty on the determined vector effective length of the SALLA is 3.0%, which causes a similar uncertainty on the reconstructed amplitude.

The reference source is aligned via strings from ground along one of the SALLA channels. The estimated precision for the alignment between the reference source and the SALLA channel is 10°. Assuming a dipole antenna-like directivity for the reference source and the SALLA pattern, the resulting impact on the received signal amplitude due to this misalignment is 1.5%.

The total amplitude uncertainty from the source positioning and alignment is 3.4%, resulting from the quadratic sum of individual contributions.

Measurement adapter

The measurement adapter, necessary for the calibration of the low-noise amplifier (LNA), has a direct influence on the calibration measurements. Using an alternative adapter for the calibration of LNAs for Tunka-Grande in 2014 (not evaluated in this work), a systematic difference of around 2 dB (26% amplitude) was found between the two adapters alone.

However, since all electronics and their calibration were included in the calibration with the reference source, constant, systematic uncertainties during the calibration of the electronics cancel for the reconstruction of air-shower signals. They appear twice with opposite signs, during the calibration of the electronics and the calibration of the antenna. This is for example the case for the uncertainty due to the measurement adapter for the low-noise amplifier, but also for the electronics response in general. Thus, the amplitude scale of Tunka-Rex is to first order defined by the amplitude scale of the reference source. The remaining role of the electronics calibration is to compensate production fluctuations, which are comparatively small. Consequently, the contribution of the measurement adapter to the uncertainty of the amplitude reconstruction with Tunka-Rex is negligible.

Noise

There are multiple unidentified sources of background and thermal noise, which are visible in the recorded traces of the Tunka-Rex antenna stations as a noise floor. This noise adds power to the signal, and therefore, biases the reconstructed amplitude [119].

To determine the bias, air-shower simulations of radio signals with CoREAS [73] were performed, and the reconstructed amplitude before and after adding measured noise samples were compared to each other. The highest mean bias is found at the detection threshold (see Sec. 6.2), at a signal-to-noise ratio of 10, and amounts to 20%. The mean ratio of true and biased amplitudes was parametrized as a function of signal-to-noise ratio and is used to correct for the bias during the signal reconstruction. Details can be found in Ref. [120].

Summary

All uncertainties mentioned in this section are summarized in Table 5.1. Taking a single antenna, the total uncertainty for the reconstruction of the amplitude adds up in quadrature to 22%, not including uncertainties due to noise in individual measurements. It is dominated by the uncertainty on the absolute scale of 17%, mainly arising from the 16% of the calibration of the reference source. Another 14% have to be added from uncertainties varying from event to event, but correlated within individual events, and minor contribution of 2% from fluctuations from antenna to antenna within an event.

Different sets of uncertainties are required for different analyses. For example, the 2% antenna-to-antenna fluctuations have to be added in the fit of the lateral distribution of the radio signal. When comparing energy scales, based on averages over multiple antennas and events, antenna-to-antenna and event-to-event fluctuations average out and the scale uncertainty remains. For a comparison between the amplitude scales of LOPES, LOFAR and Tunka-Rex even the calibration uncertainty of the reference source drops out, because all three experiments used the same reference source.

Overall, the calibration enables a comparison of absolute radio scales, and therefore energy scales, on a 20% level, and for LOPES, LOFAR and Tunka-Rex even on a 10% level. This is exploited for the comparison of Tunka-Rex and LOPES presented in Ch. 7.

Table 5.1: Uncertainties for the reconstruction of the signal amplitude with Tunka-Rex. There are three categories: antenna-to-antenna fluctuations, uncertainties with event wide correlation and the uncertainty on the absolute scale. These have to be added depending on the analysis.

Level	Origin	Uncertainty (%)
Antenna-to-antenna	positioning and alignment	2
	antenna production	1
	Total	**2**
Event-to-event	antenna model	12
	environmental temperature	4
	ground conditions	3
	crosstalk	2
	Total	**13**
Absolute scale	source calibration	16
	temperature during calibration	6
	source positioning + alignment	3
	Total	**17**
Total		**22**

6 Event reconstruction and detection thresholds

To reconstruct the parameters of cosmic-ray air showers with radio measurements, the radio signal first has to be identified and separated from background. Only then, its properties can be correlated to air-shower parameters. The background, and subsequent selection criteria, also ultimately limit the sensitivity of a radio detector, dictating its detection thresholds and efficiency.

In this chapter, it is discussed what background is encountered at the experimental site and how it can be suppressed. Then, arrival times of radio signal from air showers are analyzed to identify a signal window. Requirements for signal-to-noise ratios are defined for a standard reconstruction method as basis for Tunka-Rex analyses. The standard reconstruction is then applied to data of the first two seasons (2012/2013 and 2013/2014). Finally, the detection thresholds of the detector are modeled, analyzed for different configurations and the model is checked against measurements.

6.1 Background at the site

Radiation in the radio band is commonly encountered all over the world in the form of the galactic radio background, as well as background with anthropogenic origin, e.g. from radio communication. Therefore, the first step for the measurement of the expectedly weak radio signal is to understand the background and possibly suppress it to enhance signal-to-noise ratios. To identify sources of background, a first, simple test was performed: The stages of the signal chain were gradually disconnected and traces were recorded to see how the mean frequency spectra change. In Fig. 6.1, the spectra are shown for different configurations.

In the first step, the full signal chain was connected. A flat frequency spectrum is obtained in the realized band with several peaks: at 20 MHz, from the heating controller, at 25, 50 and 75 MHz from the digitizers, also seen in the PMT traces, and at each 5 MHz of unknown origin.

In the next step, the antenna is short-circuited to suppress reception of external background, and to measure only thermal noise including that of the low-noise amplifier. The resulting spectrum is distorted, probably as a result of some not well understood impedance from the short-circuiting, now loading the low-noise amplifier. The overall power drops by roughly 3 dB, corresponding to a factor of 2. This was expected from the discussion of internal noise in Sec. 5.3: the background contribution received by

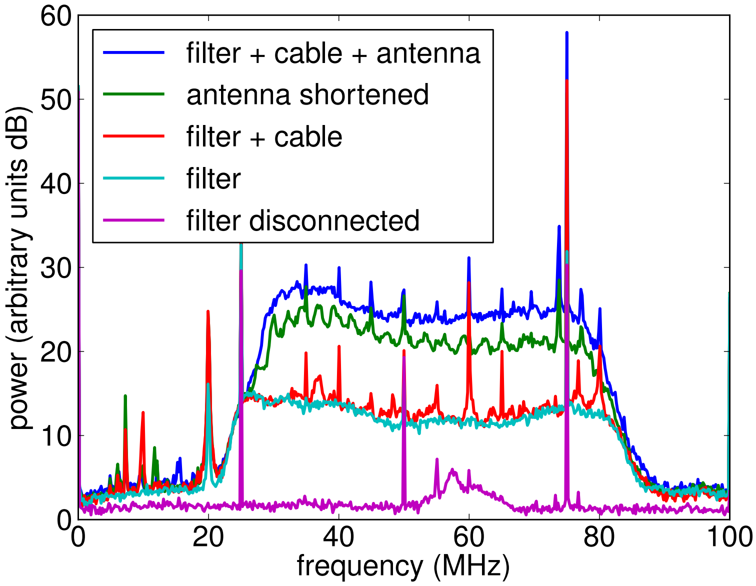

Figure 6.1: Mean spectra of one antenna station in different configurations. By gradually disconnecting the signal chain, noise sources can be identified. Around half of the noise is of external origin, probably galactic background. The remaining half is mostly thermal noise up to the first amplifier stage.

the antenna due to the galactic background, which depends on the antenna gain, is estimated to be in the same order as the internal system noise.

Then, the low-noise amplifier is disconnected completely, leaving the 29.9 m RG213 cable attached to the filter amplifier. The total power of the recorded spectrum drops significantly, by another 10 dB. The reason is that the first amplifier stage is disconnected, which is the main source of signal and system noise.

In the next step, the RG213 cable is disconnected from the filter amplifier. While the flat region of the spectrum remains the same, being dominated by the noise of the filter amplifier, the peaks at multiples of 5 MHz vanish. Thus, this signal is either directly received by the cable or results from reflections in the cables when connected to the LNA and filter amplifier.

Finally, the filter is disconnected and only the digitizers remain. The 25, 50 and 75 MHz peaks persist, also seen in the PMT traces. They are received directly by the digitizers, probably from a clock in the cluster centers.

The narrow peaks in the spectrum are easily suppressed during the offline signal processing by digitally filtering them, i.e. cutting them in the frequency domain. For the standard reconstruction all frequencies corresponding to integer multiples of 5 MHz are cut in the whole band.

Occasionally, broadband noise up to 35 MHz is observed in some antennas. To avoid having several classes of events, the lower band limit is simply increased from 30 to

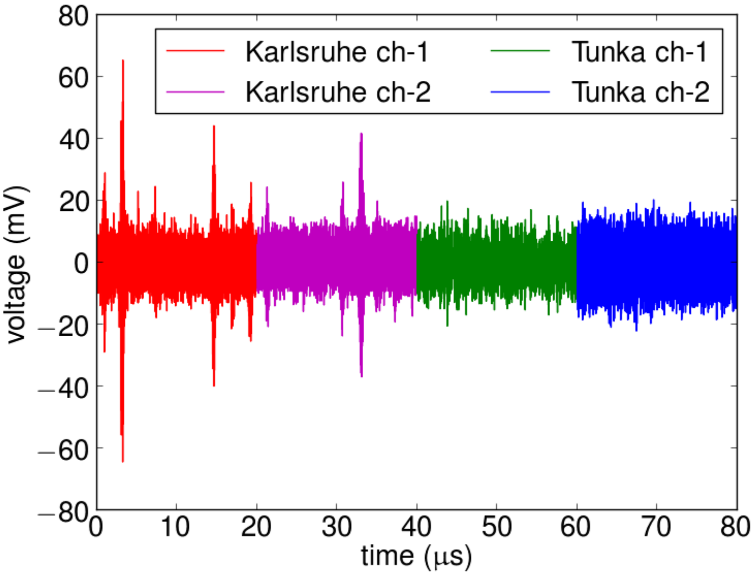

Figure 6.2: Traces from the full signal chain of an antenna station in the Tunka valley and from the antenna station deployed in Karlsruhe, at KIT Campus North, for the calibration. While the underlying, uncorrelated broadband background is comparable in magnitude, more transient pulses are recorded in Karlsruhe.

35 MHz for all events. Thus, a digital band-pass filter, applied during signal reconstruction, crops the amplitude spectrum to the realized band of 35 to 76 MHz.

6.1.1 Background measurement in Karlsruhe

One of the expected advantages of measurements in the Tunka valley is a reduced background compared to measurements in populated areas. With the Tunka-Rex antenna station deployed in Karlsruhe for the calibration, this assumption could easily be tested. With the same systems used for reception in the Tunka valley and Karlsruhe, the voltage traces can be directly compared to each other. For this purpose, some traces of antenna stations in both locations were recorded with an oscilloscope.

In Fig. 6.2, recorded traces during day time are shown. One difference is that significantly more pulses are observed in the traces from Karlsruhe. These are likely caused by switching electric devices close-by. If these peaks happen to appear in the signal window, they can be mixed up with the air-shower signal.

In the recorded test traces in Karlsruhe, a rate of about 400 kHz was found for pulses with a signal-to-noise (SNR) ratio above 10. With the signal window defined in Sec. 6.2, this would cause a peak within the signal window, possibly mixed up with the signal in 10% of the antennas during an air-shower event. The corresponding rate for the Tunka valley, determined in Sec. 6.2, is only about half that value. Therefore, indeed

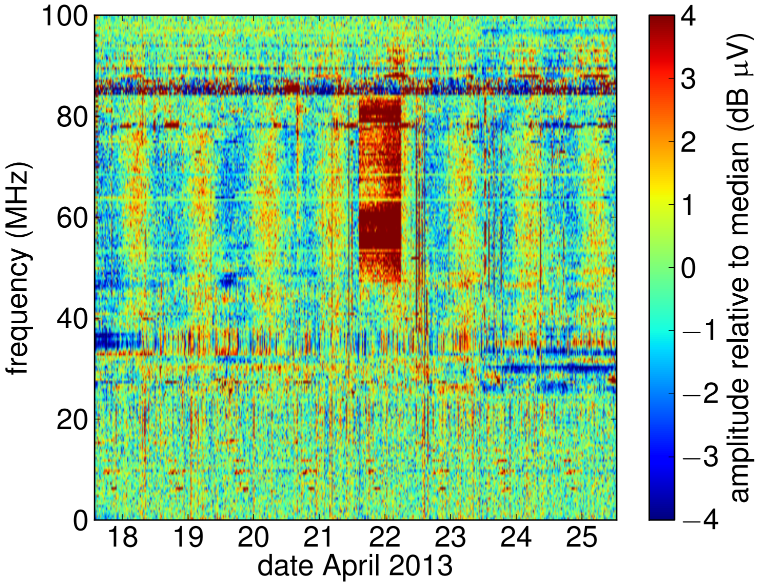

Figure 6.3: Dynamic background spectrum relative to its median for several days, measured with a Tunka Rex antenna station in Karlsruhe. Variations in the galactic background are visible as broad stripes with a period of about one day. Their observation indicates the sensitivity of the antenna for galactic radio background.

the detection threshold in the Tunka valley is lower than in Karlsruhe.

The underlying uncorrelated broadband noise in both traces is about the same. Since the band of the antenna was chosen to avoid human-used frequencies, the noise should be caused mainly by the galactic radio background and system noise. Since Karlsruhe and the Tunka valley are roughly located at the same latitude, the same portions of the galactic plane are observed, and consequently, the galactic radio background is approximately equal.

To test if the uncorrelated broadband noise is indeed galactic radio background, it was observed on a longer time scale. For this, an automated data-acquisition system from commercially available parts was setup to record one trace per minute for several days. Traces of 20 µs length were recorded with an oscilloscope of the type Picoscope 6402C with a sampling rate of 1.25 GHz.

Two measurements were taken, for 7 days from April 18th on and for 11 days from August 1st on in 2013. In Fig. 6.3, the dynamical variation of the spectrum relative to the median of the second measurement is shown. Long term variations with a period of roughly 24 h can be seen in the form of broad vertical stripes. They could either be attributed to galactic noise, varying with a period of a sidereal day, 23 h56 min, or to environmental and human variations, following the 24 h day-night period.

To determine the origin of the periodic variation in a simple way, i.e, without modeling the galactic background in detail, the long lever of the two measurements can be exploited to reach the required sensitivity for distinguishing the two periods. While day-night correlated effects will remain its phase within the 105 days, the sidereal period will have accumulated a phase shift of 420 min relative to UTC time. A sine function was fitted to the 65 MHz line of the amplitude variation to determine its phase. The phase was found to have changed by 432±10 min, consistent with the expectations of the sidereal day.

This hints towards the galactic noise hypothesis, and therefore, to the sensitivity of the antenna up to the level of the galactic radio background. Since this background ultimately limits the amplitude based detection of radio signals, an antenna type with higher gain will add only little further sensitivity to the radio signal from air showers. This is quantitatively discussed in Sec. 6.4.

Thus, contrary to results from prior works [93], the SALLA turns out to be not strongly limited in the detection of radio signal from air showers by its sensitivity. Because the SALLA features many advantages, like ruggedness, a uniform sky coverage, and low dependence on ground conditions, it is a suitable antenna for the radio detection of cosmic rays and should also be considered for application in future radio experiments.

6.2 Signal identification

For the identification of radio signal from air showers in the recorded traces, the signal window and threshold for the signal-to-noise ratio are determined.

Signal window

The signal window is the time interval in the trace in which the signal is encountered. Tunka-Rex operates in slave mode with Tunka-133, i.e., data from the antenna stations is exclusively recorded together with Tunka-133 data, whenever Tunka-133 is triggered. The trigger conditions require 3 PMTs above a signal threshold and whenever this is fulfilled, traces from the whole cluster are recorded, centered around the trigger time of the third PMT in chronological order [98]. Thus, the trigger time is always in the center of the recorded trace, at a relative time of $1024 \cdot 5\,\mathrm{ns}/2 = 2560\,\mathrm{ns}$.

The relative position of the antenna signal in the raw traces is determined by the relative time between the shower-front arrival at the third PMT and at the antenna, and propagation times of the signal from the PMTs and antennas to the data-acquisition boards in the cluster centers. While the shower-front arrival depends on the shower geometry, the signal propagation causes a constant time offset. Thus, there will be a constant time offset Δt between the antenna signal and the trigger time, plus a variation δt.

Δt is determined as the mean time between antenna signal and trigger time. This depends on the difference of propagation times between signal from PMTs and antennas. Propagation times for the signal chain components of the antenna station are known to a precision of about 2 ns from the electronics calibration. Because the antenna station

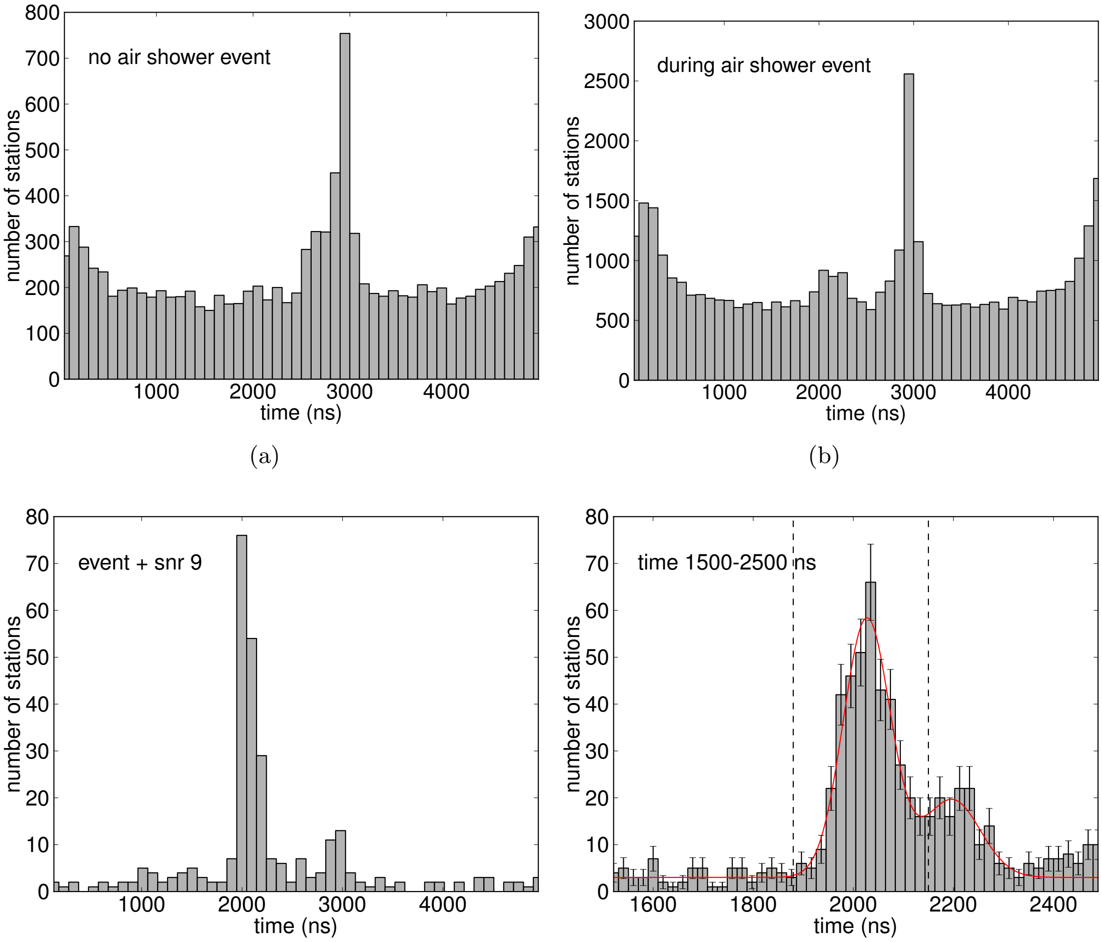

(a) (b)

(c) (d)

Figure 6.4: Time distribution of the highest signal peaks in recorded traces (a) when there was no air-shower event, (b) during high energy-events, (c) as b, but with signal-to-noise ratio above 9, (d) as c, but in the interval 2000±500 ns. The time window of the signal is determined from a fit to the distribution in d, and indicated by the dashed lines. The second bump observed around 2200 ns is from afterpulses of unknown origin and is cut.

response is inverted during signal reconstruction, the radio signal is corrected for these delays and they are effectively set to zero. The time delay of the PMT signal on the other hand is only partially known: it is at least 400 ns due to the travel of the PMT signal through 80 m coaxial cable, plus some unknown constant for the response of the PMT electronics.

δt is the variation in individual relative propagation times, due to fluctuations in PMT electronics and cable length, and varying geometrical delays from the relative time of shower-front arrival. Since the maximum distance of a PMT to the antenna of the same cluster is around 80 m, the geometrical delay is at most 200 ns for zenith angles below 50°, as considered for the standard reconstruction, and 250 ns for inclined showers with zenith angles up to 70°.

Due to the unknown delays of PMT electronics and its variations, a phenomenological approach was chosen for the determination of the signal window. For that purpose, the distribution of the highest peaks in subsets of recorded traces was determined, shown in Fig. 6.4. First, in (a), the whole trace is checked when there was no successfully reconstructed air-shower event by Tunka-133, i.e., it is likely a background event. The distribution has a peak around 3000 ns, which is correlated with the trigger time, but not with air showers. Additionally, peaks at the edges of the trace are visible. Their origin is unknown and they are not evaluated for air-shower reconstruction. In (b), a similar distribution is shown when there was a successfully reconstructed air shower by Tunka-133. Besides the peak at 3000 ns, a second one around 2000 ns appears, but buried under a floor of background. To purify the sample, a minimum signal-to-noise ratio of 9 is required with the resulting distribution shown in (c). The peak around 2000 ns is clearly visible now. It is attributed to the air-shower signal.

Finally, the window is restricted to 2000±500 ns, resulting in the distribution shown in (d). A double bump structure appears with a main bump around 2000 ns and a second, smaller bump around 2200 ns. Checking for several events antennas with the signal in the second bump, it is found that these antennas often feature a another, weaker signal peak in the region of the main bump, too. Moreover, in events with many antennas, the pulses from the second bump are often outliers in the plane wave fit of arrival times, while the corresponding signal peak from the main bump in the same trace would fit better. Therefore, the signal pulses in the second bump are classified as afterpulses which are correlated with the air-shower signal, but the real air-shower signal appears earlier in the trace, in the region of the main bump. The signal peaks shortly after the signal window in the 3rd and 4th trace of Fig. 4.6 are possibly such afterpulses. Consequently, the signals from the second bump need to be excluded for analysis.

To determine a time window, two Gaussian distributions are fitted to the double bump and their parameters are evaluated. The main bump is found to be centered around 2030 ns with a width of 50 ns. The second bump is centered around 2200 ns with a width of 50 ns. To contain most air showers signals, the base for the signal window is chosen to be the center of the main bump plus 3 standard deviations. Since the second bump needs to be excluded, the right bound is then moved to the center of the second bump minus one standard deviation. This is a compromise between excluding afterpulses and

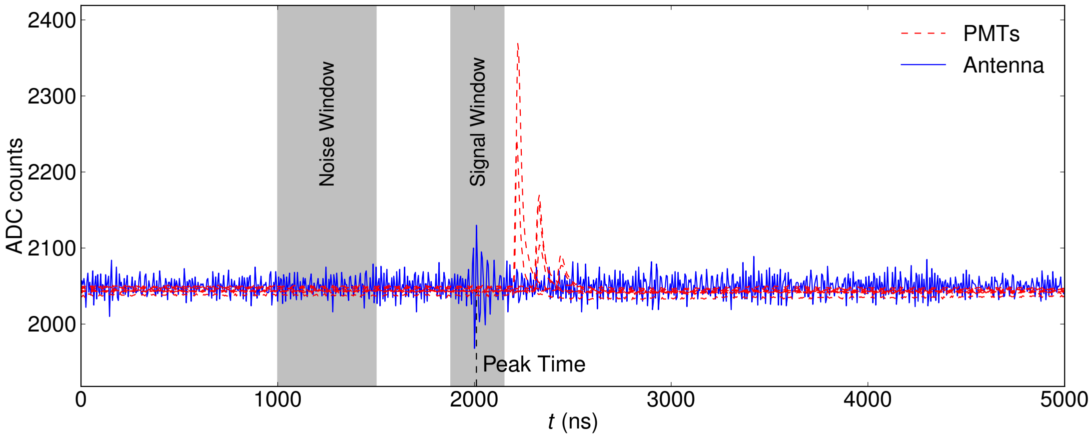

Figure 6.5: Traces from one antenna channel and the PMTs of Tunka-133 cluster during an air-shower event. Because of longer cabling, the shower signal of the PMTs is visible after the antenna signal. Signal and noise windows used in the radio analysis are indicated.

keeping signal peaks. Thus, the signal window ranges from 1880 to 2150 ns with a width of 270 ns. According to the distribution, which was fit to the main bump, this window contains 99% of the signal peaks.

Following a similar approach for the inclined showers with zenith angles above 50°, a signal window from 1850 to 2200 ns is found with a width of 350 ns. The higher width is caused by the increased geometrical delays.

Signal-to-noise cut

To further purify the antenna selection, a simple threshold cut can be applied, requiring the signal to exceed the noise floor by a certain extent, i.e., a cut on the signal-to-noise ratio. Therefore, measures for noise and signal have to be defined. As seen in Fig. 6.4, (a) the distribution of peaks in the trace for pure background is uniform, except for the edges and the bump around 3000 ns. These regions should be avoided for determining the noise level.

The noise N_{rms} is the root-mean-square of a 500 ns long portion of the trace before the signal window, from 1000 to 1500 ns. An example trace of an antenna station and PMTs from an air shower event with indicated noise and signal windows is shown in Fig. 6.5). The signal S is the maximum of a Hilbert envelope (instantaneous amplitude) in the signal window. The Hilbert envelope is used in order to have a well defined, smooth peak, independent of sampling and phase of the oscillating, bandlimited signal. While the signal is treated in terms of amplitude, the signal-to-noise ratio SNR is for historical reasons calculated in terms of power

$$\mathrm{SNR} = S^2/N_{\mathrm{rms}}^2. \tag{6.1}$$

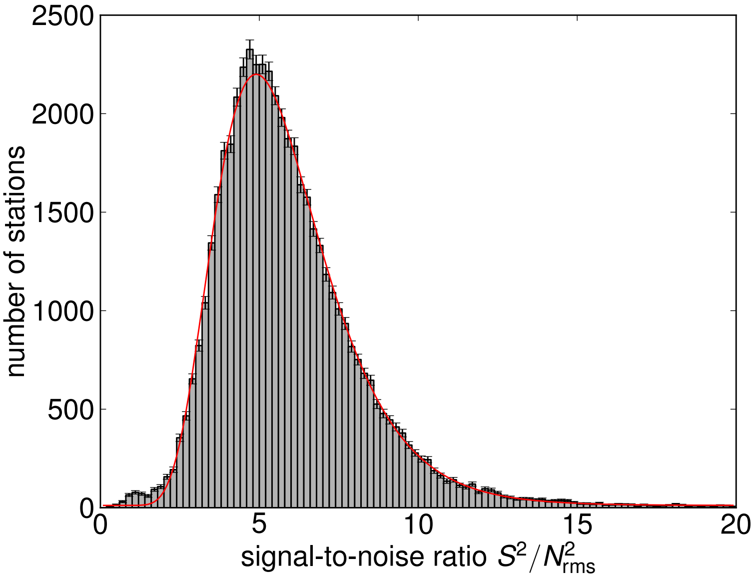

Figure 6.6: Distribution of the peak signal-to-noise ratio in the signal window for the first 200 recorded traces per day without air-shower events during the first measurement season (2012/2013). It follows approximately a log-normal distribution, from which cuts are determined on a statistical basis. A small excess at the lower end is caused by occasional failures of amplifiers.

The SNR from the first 200 recorded traces for each night in the whole first season (2012/2013) is shown in Fig. 6.6. The distribution is approximately described by a log-normal distribution, with a little excess in the low SNR region due to occasional technical problems of single antenna stations (which are cut for the standard reconstruction). The mean SNR from the fit to the distribution is 5.8. There are no significant, systematic differences between SNR distributions of different antennas, days, or for the second measurement season.

For the standard reconstruction a minimum SNR of 10 was chosen to reject approximately 95% of noise pulses for each antenna. Due to the low event statistics, i.e., around 100 air-shower events per season above threshold, this cut is chosen loosely, in favor of efficiency. The probability to include a false positive signal over the 25 stations of the whole array is around 70%. However, if two consecutive stations do not pass the SNR cut, all stations further away from the shower core are discarded for the standard reconstruction. Consequently, only two stations have to stay below threshold for all others to be excluded. So the probability to include a false positive signal shrinks to a moderate 10% and is lowered further by subsequent quality cuts.

For the inclined analysis, i.e., for events with zenith angles above 50°, the signal window is wider. Therefore, to obtain a similar background rejection as for the standard analysis, a minimum SNR cut of 12 is required.

6.3 Standard reconstruction

With the obtained signal window and thresholds for background rejection, a standard reconstruction can be defined as a benchmark for further analyses. The starting point is the raw Tunka-133 data: Whenever the trigger conditions of Tunka-133 are fulfilled for one of the 25 clusters, ADC traces for all 7 PMTs of that cluster and the corresponding Tunka-Rex antenna station are recorded with the trigger time as time stamp. This data is stored on disk at the Tunka site and brought to KIT in Karlsruhe, Germany. There it is analyzed with the radio part of the Auger Offline software framework, developed by the Pierre Auger Collaboration [96, 109].

First, the data from the multiple, autonomously triggered clusters during an event have to be identified by coincident triggers and merged. With an array diameter of 2 km, an air shower moving at the speed of light crosses the whole array in at most 6.7 µs. Therefore, events of clusters occurring within 7 µs are merged to event candidates. For the standard reconstruction only the subset of event candidates is considered, for which Tunka-133 successfully reconstructed an air-shower event with a zenith angle $\theta \leq 50°$. Thus, information from a full reconstruction by Tunka-133 is available for these events, including geometry, energy and atmospheric depth of the shower maximum.

Traces of the two antenna channels of each antenna station, so far still given in terms of ADC units, are converted to voltage according to the ADC specifications (Sec. 5.3). By Fourier transforming the traces, the amplitude spectra are obtained. As discussed in Sec. 6.1, narrowband interferences, occurring each 5 MHz, are removed by suppressing the corresponding bins and their direct neighbors with a digital, rectangular band-stop filter of 0.2 MHz width. The resulting amplitudes are corrected for the lost bandwidth by enhancing the remaining spectrum by 3.4%, according to the fraction of bandwidth cut. Additionally, the spectrum is digitally band-pass filtered to 35 to 76 MHz. The lower limit of 35 MHz is chosen in order to suppress a broadband interference (see Sec. 6.1). The upper limit of 76 MHz is the edge of the realized band (see Sec. 5.3) for the filter amplifier. Maintaining frequencies suppressed by the filter amplifier would artificially enhance noise in the trace after the inversion of the hardware response.

Then, the traces are upsampled by a factor of 4. This means that the signal is interpolated to increase the sampling density fourfold beyond the sampling of the recorded trace. This is possible according to the Nyquist–Shannon sampling theorem [107], since the used sampling rate of 200 MHz conserves the full information of signals bandlimited to less than 100 MHz. For Tunka-Rex this condition is fulfilled, since the signal is bandlimited to 35-76 MHz.

The next steps aim to invert the hardware response and reconstruct the electric field vector of the incoming signal. Following Sec. 5.1, the amplitude spectra of the traces are divided point-wise by the respective response of the analog electronics chain, determined in Sec. 5.3. The resulting traces represent the signal in terms of the open-circuit voltage of the antenna. The response function of the antenna, determined in Sec. 5.5, depends on the incoming direction of the radio signal, which is assumed to be identical to the incoming direction of the air shower [89]. For the incoming direction of the air shower, the reconstructed value by Tunka-133 is used. The voltage vector of Eq. 5.4 is assembled using the amplitude spectra of the open-circuit voltage traces from both channels frequency-wise as its elements. By inverting $\mathcal{H}$, Eq. 5.4 can be solved for the electric field vector, which is given along the spherical base vectors $\vec{e}_\theta, \vec{e}_\varphi$ (because the vector effective length was determined in these coordinates). $\vec{e}_r$ is always zero, as it points along the assumed direction of propagation for the radio signal. This assumption enables the reconstruction of the 3 components of the electric field vector with measurements from two channels.

By Fourier transforming the resulting spectra back, the trace in terms of electric field strength is obtained. However, a physical interpretation of the trace is only valid for the air shower's radio signal, because its incoming direction was used for reconstruction. Thus, in noise segments of the trace the reconstructed electric field strength becomes meaningless and only where the radio signal dominates, the obtained values maintain its sense. Minimum requirements for the radio signal exceeding the background level are ensured in the following steps.

After obtaining traces with electric field strengths from all antennas in a candidate event, noise level N_rms, signal S and signal-to-noise ratio SNR are determined, following the procedure described in Sec. 6.2. Then, the antennas are ordered by distance to the shower axis in shower coordinates. Antennas with SNR below 10 are discarded and if two consecutive antennas fail the SNR criterion, all further antennas are discarded. This way occasional false positive signals from antennas far from the shower core, where most antennas are located, are rejected. For the remaining antennas, the signal amplitude S is corrected for the noise bias as explained in Sec. 5.7.

For the standard analysis 3 antennas passing all prior cuts are required, enabling an independent reconstruction of the incoming direction with a plane shower front model. To further reject events with false positive signals, the reconstructed direction from Tunka-Rex is required to agree with the one reconstructed by Tunka-133 within 5°. Results from the direction reconstruction of an example event are depicted in Figs. 4.6 and 4.7.

6.3.1 Inclined air showers

Tunka-133 is designed for the detection of vertical air-showers with zenith angles $\theta \leq 50°$, and only these event are considered for the standard reconstruction. However, in principle it can also detect inclined events with $\theta > 50°$. Light with such high inclinations is partially reflected from the bins holding the PMTs before being detected. Thus, the efficiency and reconstruction quality suffer. The data was never thoroughly analyzed and only the shower geometry is reconstructed from Tunka-133 measurements, i.e., the incoming direction and rough position of the shower core, but neither energy nor depth of the shower maximum. The radio technique, on the other hand benefits from high inclinations. The high geomagnetic angles enhance the signal, the footprint increases due to projection effects and the signal suffers little attenuation in the atmosphere.

To reconstruct inclined air showers, the parameters of the standard reconstruction

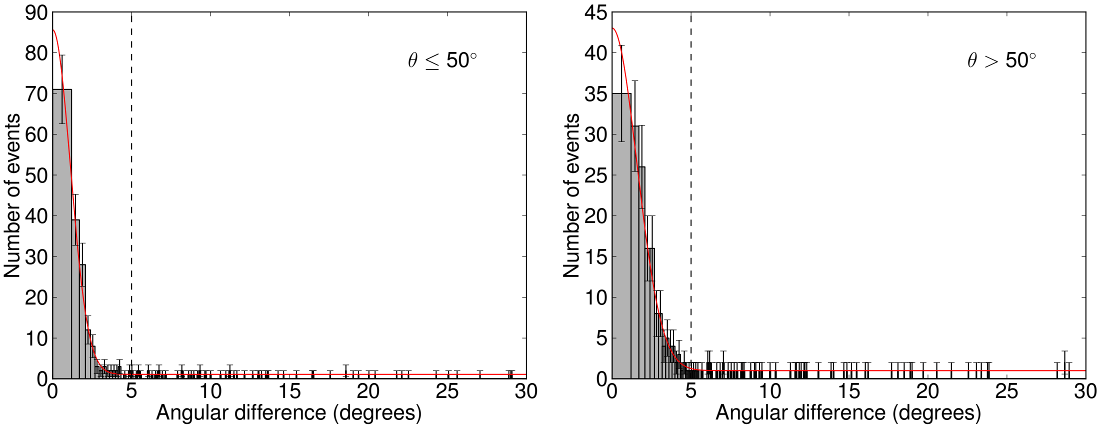

(a) (b)

Figure 6.7: Deviations of the reconstructed incoming direction of air showers between Tunka-Rex and Tunka-133 (a) for vertical showers ($\theta \leq 50°$) and (b) for inclined showers ($\theta > 50°$). The bin width is variable to account for the increasing phase space towards higher deviations. The peak at low deviations can be attributed to the combined angular resolution of Tunka-Rex and Tunka-133 of 1.1°. Events with deviations above 5° are rejected for the standard reconstruction.

have to be slightly adapted: the signal window is increased to a width of 350 ns, to account for the higher geometrical delays, and the minimum signal-to-noise ratio is set to 12, due to the wider signal window. Furthermore, antennas after two consecutive silent stations are kept, because of the rough core estimate from Tunka-133.

In 2015, the interior of the metal bins was painted black to suppress reflections. Thus, the detection of inclined events is only possible for previously taken measurements, or maybe for future measurements when triggered by Tunka-Grande, whose zenith angle range is not yet known.

6.3.2 Measurements from 2012-2014

The standard reconstruction can now be applied to data of the first two measurement seasons 2012/2013 and 2013/2014 with their respective detector setups. Data of the third season, 2014/2015, mostly suffered from technical problems with the time synchronization of Tunka-133 and is not used for the present analysis.

To investigate the angular resolution of Tunka-Rex, all events with a direction reconstruction from Tunka-Rex are evaluated, irrespective of their deviation from the Tunka-133 reconstruction. This results in 117 vertical events in the first season, and 132 in the second season. In Fig. 6.7, the difference of the direction reconstruction of Tunka-Rex versus Tunka-133 is shown. The peak at low angles can be attributed to the angular

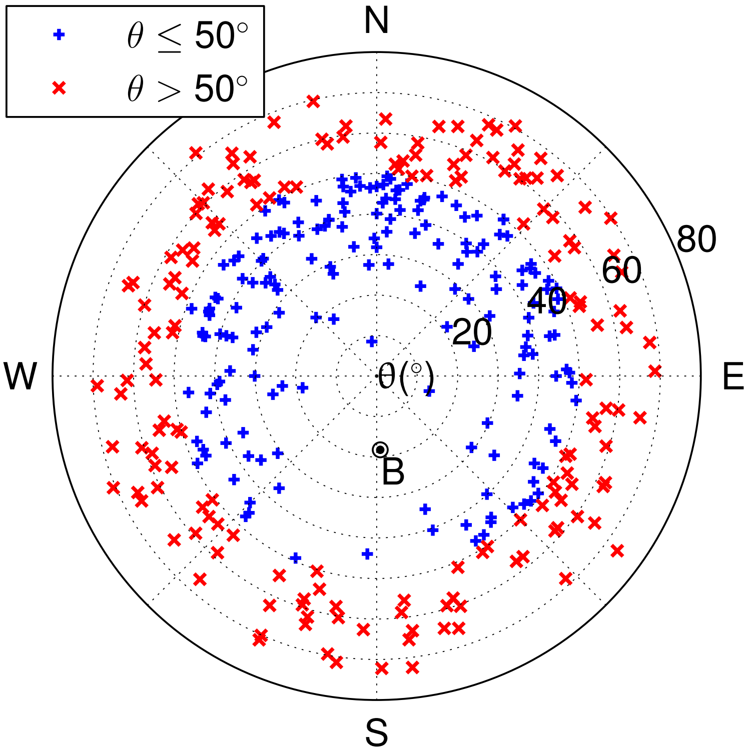

Figure 6.8: Distribution of Tunka-Rex events on the sky. Due to the geomagnetic emission mechanism of the radio signal, the detection threshold is higher for events with incoming directions close to the Earth's magnetic field B. For inclined events ($\theta > 50°$) the energy threshold of Tunka-Rex is lower due to high geomagnetic angles and geometric projection effects, but efficiency and reconstruction quality of Tunka-133 suffer.

resolution of Tunka-Rex. Fitting a one sided Gaussian with offset to the distribution yields a combined angular resolution of Tunka-Rex and Tunka-133 of $1.1° \pm 0.05°$, with a negligible contribution of 0.3° from Tunka-133.

Additionally, 114 and 124 inclined events are found in the first and second season, respectively, which are also shown in Fig. 6.7. The angular resolution for these events changes only marginally to 1.4° ±0.14°. Both distributions, for vertical and inclined events, are overlayed with a floor of events extending to high angular deviations. They usually have an outlier in the plane wave fit, distorting the direction reconstruction and are cut if the deviation is above 5°.

After the cut on the angular deviation, 90 and 87 vertical, and 85 and 82 inclined events remain from the first and second season, respectively. Additional events can possibly be recovered, e.g., by tuning the signal window to the incoming direction, additionally selecting antennas by further signatures of the signal, like the polarization, or releasing the selection criteria. In Sec. 7.1 it is investigated, how an energy reconstruction can be performed with a single antenna station. This reduces the required number of antennas with signal from 3 to 1 and increases event statistics by more than three times.

In Fig. 6.8, the distribution of the events on the sky is shown. An underdense region is visible around the direction of the Earth's magnetic field, causing a north-south asymmetry. Such an effect is expected from a geomagnetic emission mechanism, because the radio-signal strength depends on the geomagnetic angle, which causes a similar effect for the energy threshold, . This was observed before by multiple radio experiments [121, 122, 123, 83].

To test the significance of the underdense region, an equal distribution is assumed. Dividing the sky into two halves, simple Poisson statistics are obtained for the event numbers. Looking at the vertical events, with zenith angles $\theta \leq 50°$, the total event number is 177, with 49 in the Southern Hemisphere and 128 in the Northern Hemisphere. With an expectation value of 88.5 per hemisphere, the probability to observe this or a higher asymmetry is of the order 10^{-10}. For the Eastern and Western Hemispheres, with 87 and 90 events, respectively, the probability is 32%. Thus, a clear north-south asymmetry is observed, which is not consistent with statistical fluctuations.

Besides the dependence on the geomagnetic angle, there is also a zenith-angle dependence of the energy threshold. This is visible on the opposing side of the Earth's magnetic field, at higher geomagnetic angles. While in the southern half significant event numbers are obtained around $\alpha = 20°$ (zenith $\theta = 40°$), in the northern half this corresponds to the almost empty region around $\theta = 0°$. The energy thresholds, including influences of both, geomagnetic and zenith angle, are modeled in Sec. 6.4.

6.3.3 Lateral distribution function of the radio signal

To combine the information of signals S of all radio antennas in an event for the reconstruction of air-shower parameters, a model is fit to the radio signal. Measured model parameters are then correlated with properties of air showers. The function describing the amplitude of the radio signal in shower coordinates is traditionally called the lateral distribution function (LDF).

The model developed for Tunka-Rex is an extended exponential LDF model. It includes a correction for the azimuthal asymmetry of the LDF, caused by the interference of radio emission due to the geomagnetic and the Askaryan effects. Details can be found in Ref. [124].

To correct for the azimuthal asymmetry, the mean contribution of the Askaryan effect to the signal is modeled with the sole parameter $\varepsilon = 0.085$. ε was determined from air-shower simulations, and is the mean of the signal amplitude from the Askaryan effect relative to the geomagnetic effect for a maximum geomagnetic angle of $\alpha = 90°$ (between the Earth's magnetic field $\vec{B}$ and the shower axis $\vec{v}$). The measured signal in each antenna $S_{\mathrm{meas}}(\phi, r)$ at the distance from the shower axis r and angle ϕ, between

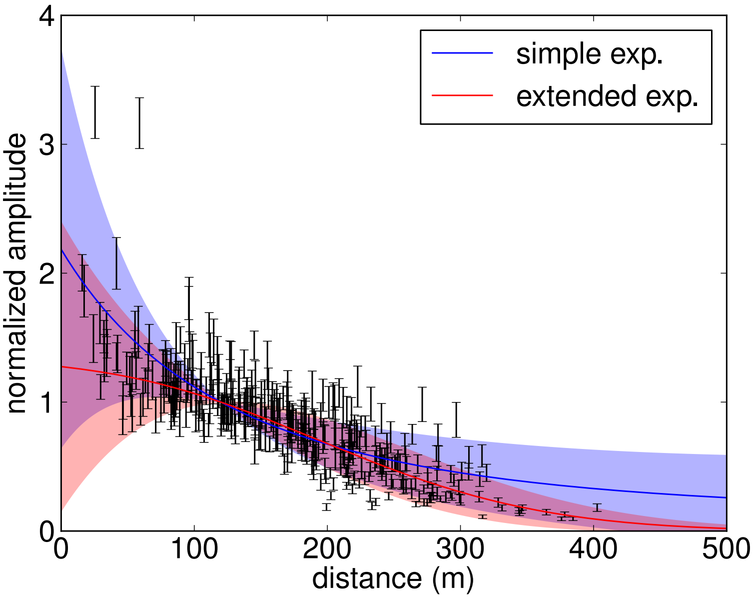

Figure 6.9: All amplitudes from events of the standard reconstruction during the first measurement season. To compare the shape of the lateral distribution, the amplitudes are normalized to the amplitude at 120 m, reconstructed with a simple exponential LDF model. Additionally, the mean and spread of the points from all LDF fits of the respective events are shown for an extended and simple exponential model, normalized to the respective reconstructed amplitude at120 m.

the antenna and $\vec{v} \times \vec{B}$, is then corrected for the asymmetry and geomagnetic angle with

$$S(r) = \frac{S_{\text{meas}}(\phi, r)}{\sqrt{\varepsilon^2 + 2\varepsilon \cos\phi \sin\alpha + \sin^2\alpha}}. \tag{6.2}$$

The obtained, corrected amplitude is approximately symmetric around the shower axis and independent of the geomagnetic angle α. It represents the expected, geomagnetic signal component for a maximum geomagnetic angle of $\alpha = 90°$. A radially symmetric, extended exponential LDF is fit to the corrected radio amplitudes in shower coordinates

$$S(r) = S_{r_0} \cdot \exp(a_1(r - r_0) + a_2(r - r_0)^2). \tag{6.3}$$

The air-shower energy E and depth of the shower maximum X_{max} can be reconstructed from parameters of the LDF as described in Ref. [124]. 2 of the 4 parameters were determined with air-shower simulations: r_0 is set to 120 m in order to maximize the precision of the energy reconstruction with S_{r_0}. a_2 is parametrized in terms of zenith angle θ and energy E. The remaining parameters S_{120} (S_{r_0} for $r_0 = 120$ m) and a_1 are obtained from a fit of the LDF to the measured signal amplitudes and used for the reconstruction of E and X_{max}. The energy E, needed to determine a_2 is preliminary estimated using a simple exponential LDF.

However, as shown in Sec. 7.1, the extended exponential LDF model improves the energy reconstruction only marginally relative to a simple exponential one of the form

$$S(r) = S_{r_0} \cdot \exp(-\eta(r - r_0)). \tag{6.4}$$

In Fig. 6.9, all amplitude measurements of the first two seasons are shown, normalized to S_{120}, determined with a simple exponential LDF. Additionally, the mean and standard deviation of the points from all LDFs of the respective events, for the simple and the extended exponential models are shown, normalized to the respective S_{120} of the models. Due to the normalization all LDFs are identical at a distance of 120 m. In the range between distances of 50 to 300 m both models give similar results. Only for measurements very close and far from the core, where typically only few antennas are located and pass the signal threshold, the models differ significantly.

Therefore, both LDF models can be used to fit the high-signal region and reconstruct the primary energy with similar precision, as shown in Sec. 7.1. The extended LDF model becomes more important for the reconstruction of the depth of the shower maximum X_{max}. On the one hand, stations with signal far from 120 m are required to be sensitive to the LDF slope. One the other hand, if stations too far away are included in the fit, the slope of the exponential model is distorted and looses sensitivity. Decent results can be reached for the reconstruction of X_{max} with the exponential model by requiring an antenna station with signal between $r = 200\,\mathrm{m}$ and $r = 300\,\mathrm{m}$ [125]. However, using the extended exponential model, the far region can be included in the fit without loosing sensitivity [85].

6.4 Energy thresholds and efficiency

The efficiency describes the fraction of events satisfying certain conditions, e.g. passing quality cuts. An efficiency below 1 often comes with the risk of selection biases and reduced exposure. The high duty cycle of the radio technique is one of its main advantages. However, its benefits might be canceled by a low efficiency, because event statistics are acquired via the exposure, which also depends on efficiency. Directly connected to the efficiency are detection thresholds, which describe where efficiency starts rising above zero or saturating. The goal of the study described in this section is to develop a generally applicable model for the efficiency and detection thresholds of radio detectors for air showers and investigate it in detail for Tunka-Rex.

The efficiency depends on the selection criteria and usually has to be traded against purity. To model the efficiency, the standard reconstruction is used as a benchmark. It requires 3 stations above a signal-to-noise ratio (SNR) of 10, which can be transformed to a threshold for the signal amplitude S_{th} with the definition of the SNR (see Eq. 6.1)

$$S_{\mathrm{th}} = \sqrt{10} N_{\mathrm{rms}}. \tag{6.5}$$

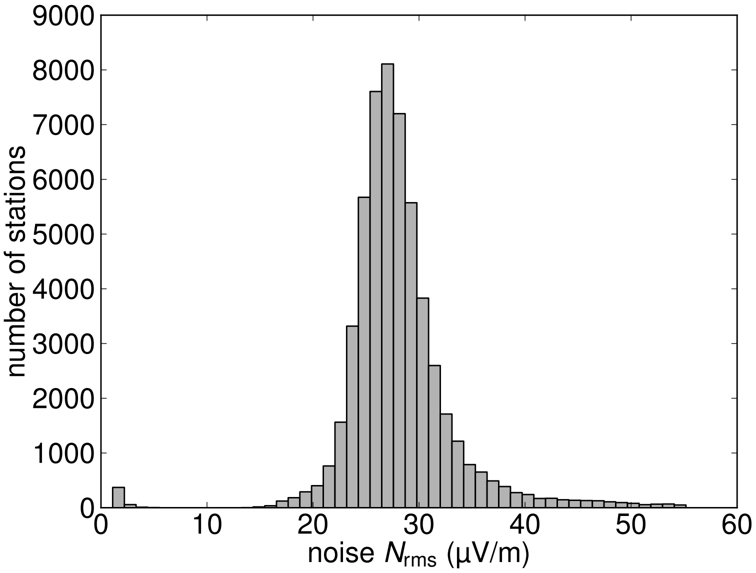

Figure 6.10: Root mean square in the noise window from the first 200 event of each day during the first measurement season. The distribution is stable over different antennas and time. The little excess at low values occurs due to occasional failures of amplifiers.

The mean noise level N_{rms}, depicted in Fig. 6.10, is 28 µV/m. Therefore, the threshold for the signal amplitude in a single antenna station is about 90 µV/m.

The region where the radio signal is expected to surpass this threshold is described by the LDF. In Sec. 6.3.3 it is argued, that a simple exponential function (see Eq. 6.4), which has 2 parameters, is a suitable radio LDF for the high signal region ($r \lesssim 200\,\mathrm{m}$). As evident from the LDFs of all events of the first season, shown in Fig. 6.9, the LDF is to first order defined by the energy estimator S_{120} alone. Especially in the intermediate region, between 50 m and 300 m distance, where most antennas with signal are located, the obtained amplitudes are with an accuracy of about 20% described by a LDF with the mean slope. This is also exploited in the model presented here.

To estimate the efficiency, the area around the shower axis with signal above threshold on ground, i.e., projected on the detector plane, is defined as

$$A_{\mathrm{th}} = \frac{\pi r_{\mathrm{th}}^2}{\cos\theta}. \tag{6.6}$$

With the distance r_{th} in shower coordinates, within which the expected signal surpasses the detection threshold, obtained from Eqs. 6.5 and 6.4

$$r_{\mathrm{th}} = r_0 + \frac{1}{\eta}\ln\frac{S_{120}}{S_{\mathrm{th}}}. \tag{6.7}$$

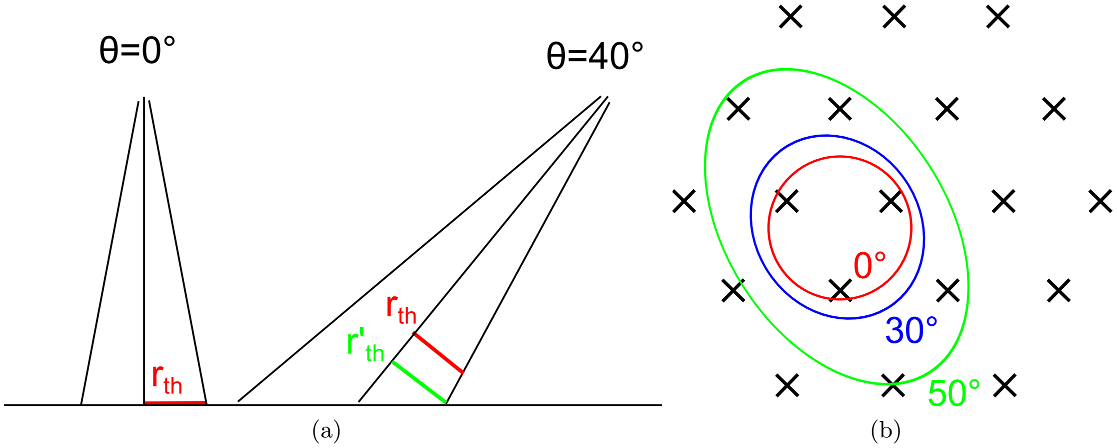

(a) (b)

Figure 6.11: (a) Projection effect for the footprint of the radio signal due to inclination. Because the shower development moves further away from the detector, the signal laterally spreads out further until reaching the detector. This is partially countered by the simultaneously declining signal strength. (b) Footprint of the radio signal from a $10^{17.5}$ eV shower, assuming a constant geomagnetic angle of 18° (like for vertical showers). With increasing inclinations, the footprint covers progressively larger areas.

As stated in Sec. 6.3.3, S_{120}, reconstructed by Tunka-Rex, corresponds to the expected maximum signal contribution from the geomagnetic effect. To obtain the actually expected signal, its dependence on the geomagnetic angle α is reintroduced by multiplying S_{120} with $\sin\alpha$. The small azimuthal asymmetry of the LDF, caused by the Askaryan effect and neglected so far, becomes important for small geomagnetic angles, below 10°. Its average contribution ε of 8.5% [124], relative to S_{120}, is added to the estimated expected signal in quadrature, to take its impact on the mean signal amplitude into account. Thus, both effects, geomagnetic and Askaryan, are taken into account by substituting S_{120} with S^{α}_{120}

$$S^{\alpha}_{120} = S_{120} \cdot \sqrt{\sin^2\alpha + \varepsilon^2}. \tag{6.8}$$

Additionally, S_{120} can be expressed in terms of energy via [126]

$$E = \kappa \cdot S_{120}, \tag{6.9}$$

with $\kappa = 884\,\frac{\mathrm{EeV}}{\mathrm{V/m}}$.

While Eq. 6.6 takes the projection of the footprint on the detector plane into account, there are further effects due to inclination: the air-shower development progressively gains distance to the detector with higher inclination. This causes a second projection effect, due to the prolonged longitudinal propagation of the radio signal, illustrated in Fig. 6.11 (a).

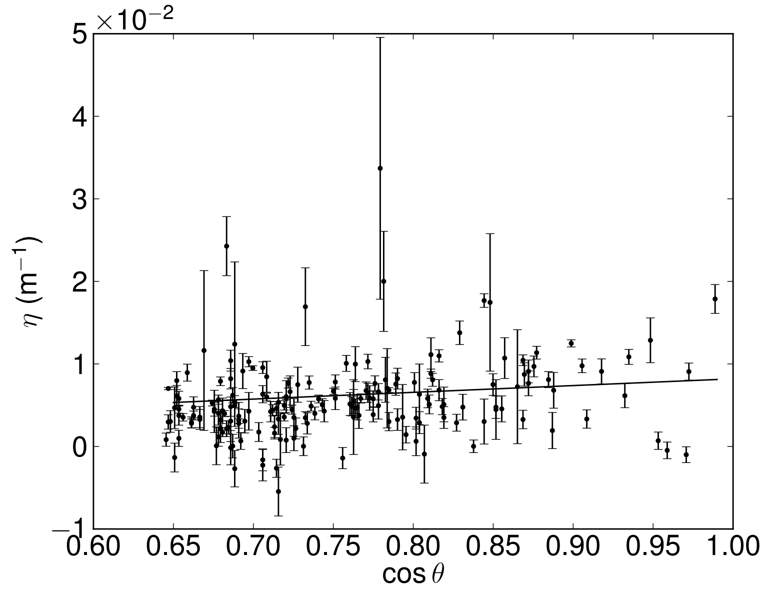

Figure 6.12: Slope η of a simple exponential radio LDF fit for events of the standard reconstruction of the first two measurement seasons 2012/2013 and 2013/2014. For small zenith angles ($\theta \leq 50°$), it rises approximately proportional to $\cos\theta$, like the geometrical distance to the shower maximum.

This projection is one reason, why the LDF slope is sensitive to the atmospheric depth of the shower maximum, or more precisely speaking, to the distance of the detector to the shower maximum. Assuming the air shower to be a point source, the projection corresponds to a transformation of every point of the vertical LDF to the coordinates $r' = \frac{r}{\cos\theta}$ with the zenith angle θ. Thus, the new LDF, now with the reference distance $r'_0 = \frac{r_0}{\cos\theta}$, has the slope $\eta' = \eta \cdot \cos\theta$. As for any exponential function, the slope is invariant under a change of the reference distance. Thus, η as a function of zenith angle can be described with

$$\eta(\theta) = \eta_0 \cdot \cos\theta. \tag{6.10}$$

The slope η of a simple exponential LDF for the events of the standard reconstruction from the first two seasons (2012-2014) is depicted in Fig. 6.12. From a fit, $\eta_0 = 8.2 \cdot 10^{-3}\,\mathrm{m}^{-1}$ is determined. Determining the average slope parameter η_0 from measurements, implicitly tunes the analysis to the average X_{max} observed by Tunka-Rex.

Additionally, conserving the energy contained in the air shower footprint, the amplitudes after projection drop proportionally to $\cos\theta$. However, when obtaining the energy estimator of the projected LDF ${S_{r_0}}'$, the projected LDF is evaluated at the original reference distance $r_0 = 120\,\mathrm{m}$, rather than r'_0

$${S_{r_0}}'(\theta) = S_{r_0}(r' = r_0) \cdot \cos\theta = S_{r_0} \cos\theta \exp(-\eta_0 r_0 (\cos\theta - 1)). \tag{6.11}$$

Since r_0 is always smaller than r'_0, the distance where the projected LDF is evaluated corresponds to a smaller distance in the original coordinates. Because the LDF rises towards smaller distances, the original decline of the amplitude with increasing inclination, proportional to $\cos\theta$, is partially countered for the energy estimator S_{r_0}.

Between zenith angles of 0° to 50°, the correction term of S_{120} (with $r_0 = 120\,\mathrm{m}$) for Tunka-Rex is between 1 and 0.9, below the sensitivity of the detector to this parameter. Thus, the variation of S_{120} with zenith angle can be neglected for the energy estimation, as well as for modeling energy thresholds and efficiency.

Although valid up to zenith angles of 50°, these approximations neglect the change in shower development connected to higher inclinations, as well as the significant drop in sensitivity of the SALLA above zenith angles of 70°, and thus should not be extrapolated to very high zenith angles.

Finally, substituting S_{120} in Eq. 6.7 with S^{α}_{120} from Eq. 6.8 and inserting Eqs. 6.9 and 6.10, r_{th}, the distance in shower coordinates within which the expected signal is above detection threshold, becomes

$$r_{\mathrm{th}}(E,\theta,\alpha) = r_0 + \frac{1}{\eta_0 \cos\theta} \ln \frac{E_{\mathrm{th}} \cdot \sqrt{\sin^2\alpha + \varepsilon^2}}{\kappa S_{\mathrm{th}}} \tag{6.12}$$

The parameters of this model are r_0, η_0, ε, κ and S_{th}. They depend on the observed energy range, the magnetic field and observation depth of the experimental site, and instrumental properties like the antenna sensitivity and the bandwidth. The parameters in this section are specific for Tunka-Rex and were partly determined from measurements and partly from CoREAS simulations. They are summarized in Tab. 6.1.

Table 6.1: Parameters for Eq. 6.12, determined for Tunka-Rex, which might need to be changed for other experiments. They were partly measured and partly determined from CoREAS simulations.

Parameter	Value	Origin
r_0 reference distance	120 m	Simulation
η_0 LDF slope	$8.2{\cdot}10^{-3}\,\mathrm{m}^{-1}$	Measurement
ε charge-excess contribution	0.085	Simulation
κ radio signal strength	$884\,\frac{\mathrm{EeV}}{\mathrm{V/m}}$	Simulation
S_{th} detection threshold	90 µV/m	Measurement

Solving Eq. 6.12 for E_{th}, the thresholds for different selection criteria, also involving several antenna stations, can be derived from geometric properties of the footprint and the detector. For example the standard reconstruction requires 3 antenna stations with distances to the shower axis $r < r_{\mathrm{th}}$. The resulting dependencies of the detection thresholds are further elaborated in the following sections.

Regular hexagonal grid

The simplest approximation to describe the detector geometry of Tunka-Rex is a regular hexagonal grid with an antenna spacing of 200 m. For vertical air showers, the footprint of radio signal above threshold, according to Eq. 6.12, is described by a circle. The smallest circle containing 3 antennas, as required for the standard analysis, has a radius of 115 m. The geomagnetic angle at the Tunka site for vertical air showers is 18°. Solving Eq. 6.12 for the energy, a threshold energy of $10^{17.4}$ eV is obtained to detect vertical air showers anywhere on the grid. If the circle radius is larger than the antenna distance of 200 m, it cannot be placed on the grid without covering 3 antennas. Thus, full efficiency is reached at $r_{\mathrm{th}} = 200\,\mathrm{m}$, or $E_{\mathrm{th}} = 10^{17.7}\,\mathrm{eV}$ for vertical showers.

For inclined air showers, with zenith angle θ, the footprint becomes an ellipse (see Fig. 6.11), with minor axis $a = r_{\mathrm{th}}$ and major axis $b = r_{\mathrm{th}} \cdot \cos^{-1}\theta$. For a constant geomagnetic angle, the area covered by the footprint (see Eq. 6.6) quickly rises with inclination, like $\cos^{-3}\theta$. Thus, inclined air showers will generally have lower energy thresholds than vertical ones, except for incoming directions with small geomagnetic angles.

To determine the threshold energy also for inclined air showers, without taking each possible trigger geometry into account, the uniformity of the regular hexagonal grid is exploited. Positions on the grid where the footprint covers 3 antennas will start to appear when the covered area A_{th} approaches A_1, the area of a unitary cell containing a single antenna: When moving the edge of the unitary cell on the contained antenna, it will necessarily touch neighboring antennas. Since 3 times the area of the unitary cell contains on average 3 antennas, full efficiency will be reached when the A_{th} approaches $A_3 = 3A_1$. A unitary cell containing one antenna is a hexagon whose sides are the median lines between two antennas with distance $d = 200\,\mathrm{m}$. One side of the hexagon has then the length $a_{\mathrm{hex}} = \frac{d}{\sqrt{3}}$ and the area is $A_1 = 0.042\,\mathrm{km}^2$.

The threshold energy requiring the footprint of the radio signal above threshold to cover on average N antennas is obtained with the condition $A_{th} = N \cdot A_1$, combining Eq. 6.6 and 6.12 and solving it for the energy

$$E_{\mathrm{th}} = \frac{\kappa S_{\mathrm{th}}}{\sqrt{\sin^2\alpha + \varepsilon^2}} \cdot \exp\left(\eta_0 \cos\theta \cdot \left(\sqrt{N A_1 \cos\theta}/\sqrt{\pi} - r_0\right)\right). \tag{6.13}$$

In Fig. 6.13 the energy thresholds for $N = \{0, 1, 3, 5\}$ are shown as a function of zenith angle θ for minimum and maximum geomagnetic angles at the respective zenith angle. The $N = 0$ line indicates the threshold for the signal to exceed the single antenna threshold in at least one point anywhere in the array. It marks an absolute energy barrier for Tunka-Rex slightly below $10^{16.7}$ eV.

With the standard analysis, the detector becomes sensitive for $N = 1$, around $10^{16.9}$ eV for maximum geomagnetic angles, and reaches full efficiency for $N = 3$, at energies between 10^{17} eV and $10^{18.2}$ eV, strongly dependent on the incoming direction of the air shower. Above $10^{18.2}$ eV, the charge excess emission from the Askaryan effect alone

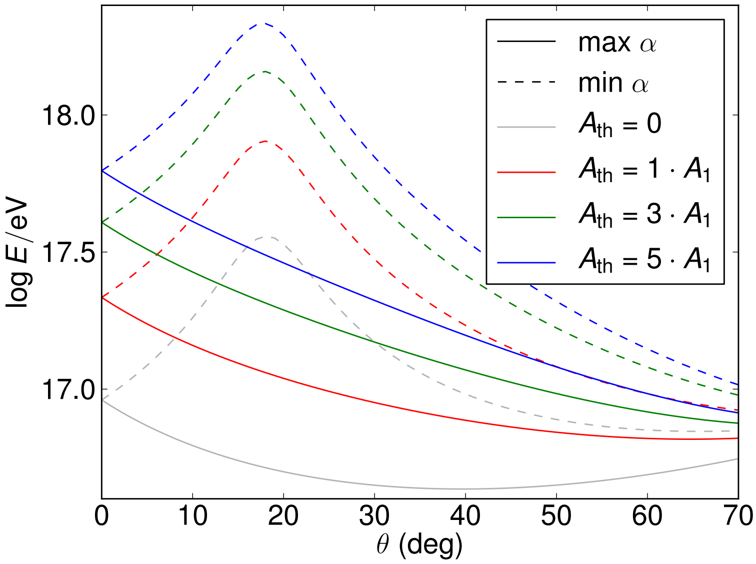

Figure 6.13: Modeled threshold energies versus the zenith angle θ for minimum and maximum geomagnetic angle α at the respective zenith angle. The different lines indicate the energy at which the signal threshold is exceeded in at least on point anywhere in the array, or in 1,3 and 5 antennas on average.

suffices to reach full efficiency for 3 antennas, even for showers parallel to the magnetic field.

Real Tunka-Rex geometry

The actual geometry of Tunka-Rex is not a perfect, regular hexagonal grid, and especially at the border regions of the array the uniform model will not hold well. To take the impact of these factors into account, the geometric problem describing the trigger conditions is solved numerically, with the 2013 layout of the Tunka-Rex array. From the solutions, threshold energies can be calculated with Eq. 6.12. The method is described in App. D, here only the results will be discussed.

Expectedly, the regular hexagonal grid describes the inner regions of the detector well, where boundary effects can be ignored. As predicted for the standard analysis by the model, Tunka-Rex becomes sensitive at $A_{\text{th}} = A_1$. In the inner detector, for shower cores within 350 m from the center of the array an efficiency of 90% is reached for $A_{\text{th}} = 3A_1$. However, including the boundary region, for shower cores within 500 m from the center of the array, the requirement increases to $A_{\text{th}} = 5A_1$. The resulting thresholds for these requirements are shown in Fig. 6.13.

In Fig. 6.14, the threshold energies for the standard reconstruction, requiring three antennas, are shown as a function of the shower core position, for vertical and 50° inclined events. The energy threshold for vertical showers is around $10^{17.4}$ eV, declining

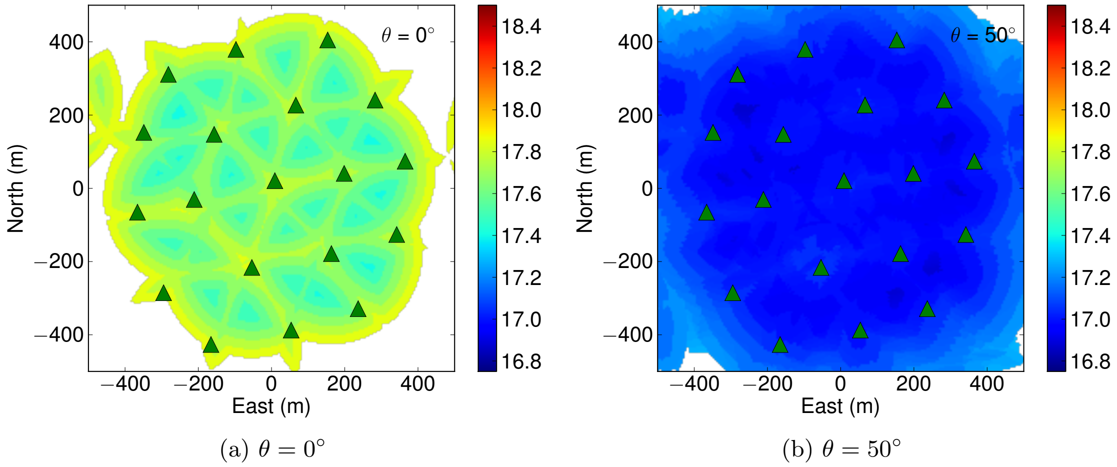

(a) $\theta = 0°$

(b) $\theta = 50°$

Figure 6.14: Threshold energies of Tunka-Rex for zenith angles of $\theta = 0°$ and $\theta = 50°$ for detection in at least 3 antennas, depending on core position. Projection effects enlarge the footprint for higher inclinations, enabling detection at lower thresholds.

below 10^{17} eV for a zenith angle of 50°.

In Fig. 6.15, the threshold energies depending on the incoming direction of the air shower are shown. Besides the clear pattern due to the geomagnetic angle, also the weaker effect of the zenith angle is visible on the opposite side of the magnetic field, especially for the thresholds for the 90%-efficiency. Thus, the low efficiency in the standard analysis at zenith angles below 30° is caused by a mixture of the nearly vertical magnetic field and the small projection of the shower footprint for air showers with small zenith angles.

Comparison to real data

To test how well the model describes the measurement, the Tunka-133 data set of the first two seasons (2012-2014) is compared to the Tunka-Rex event selection of the standard reconstruction. In Fig. 6.16, energy and zenith angle of Tunka-133 events and Tunka-Rex events with shower cores within 500 m from the center of the array are shown. Moreover, estimates for detection thresholds with maximum and minimum geomagnetic angles for the respective zenith angle are indicated.

Mostly consistent with the model, sensitivity starts around the lower boundary and almost all events are detected above the upper boundary. However, there are 4 Tunka-Rex events below the predicted minimum energy and 3 non-detected above the energy for 90% efficiency. These events were checked individually: the 3 events not detected are all from the first season, close to the boundary of the detector and the two missing antennas in 2012/2013. These two holes effectively increase the detection threshold, especially towards the border. This is further discussed in App. D.2.

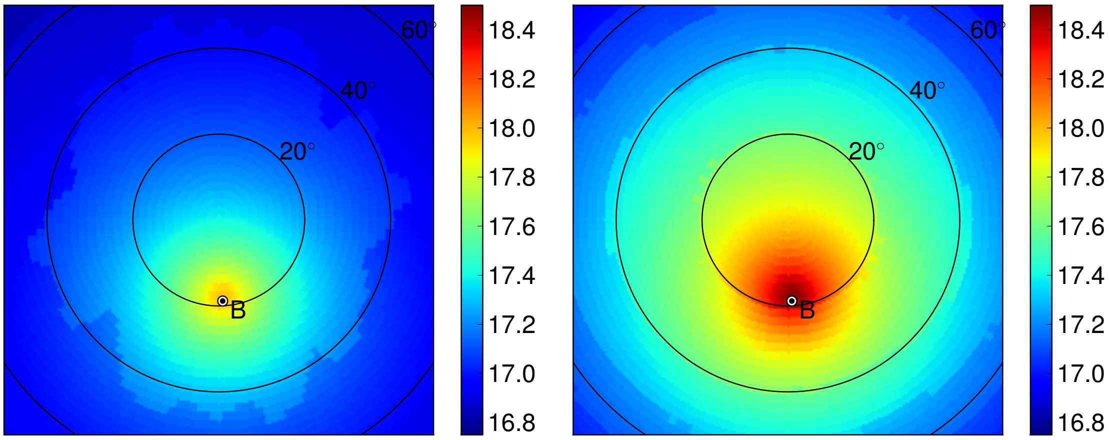

(a)

(b)

Figure 6.15: Calculated threshold energy for the standard cuts (see Sec. 6.3), depending on incoming direction, for (a) first detection and (b) 90% efficiency.

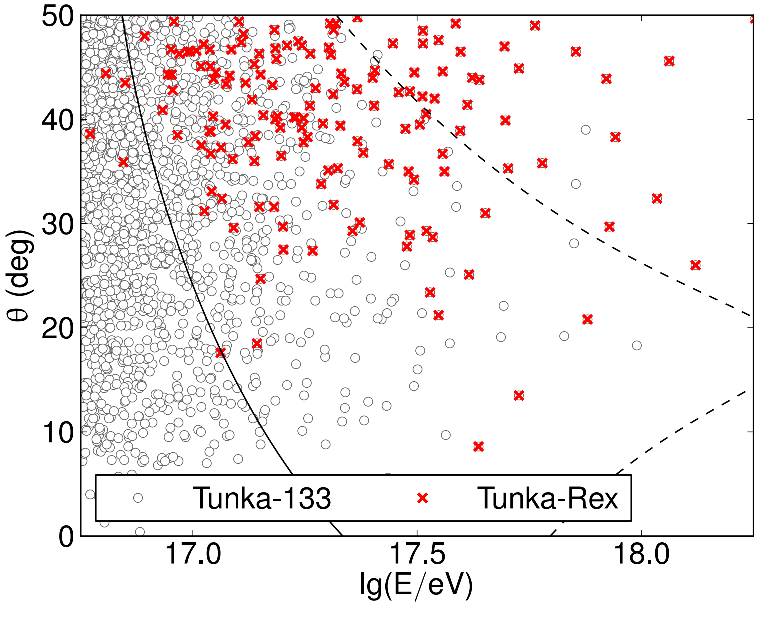

Figure 6.16: Tunka-133 and Tunka-Rex events of the standard analysis for the first two measurement seasons 2012-2014, with cores within 500 m of array center. The continuous line marks the predicted start of sensitivity, the dashed line marks the predicted boundary line for 90% efficiency.

The 4 events below the lower threshold have expected signals below threshold, but surpassed the signal-to-noise cut due to fluctuations. This is because of the static, mean signal threshold for the model, which biases the minimum threshold slightly, by about $\Delta \lg E_{\mathrm{th}}/eV = 0.1$.

Different antenna types

The SALLA antenna was considered for other experiments as well, but discarded due to its low gain, disregarding its other advantages, like ruggedness, low ground dependence and good zenith coverage [93]. However, as showed in Sec. 6.1.1, it is sensitive to the galactic radio background. Because the galactic radio background ultimately limits the detection thresholds for radio signals, the gain might not be as decisive as initially thought.

With Eq. 6.13, the impact of a higher gain antenna on the energy threshold can be quantified. An antenna with a higher gain increases the relative contribution of received signal and background relative to the system noise. Estimations from Ref. [95], confirmed in Sec. 6.1, attribute about half the total noise power in the recorded traces of the Tunka-Rex antenna station to system noise. Thus, the other half is attributed to galactic radio background.

Typical choices for alternative antennas have a gain which is about 10 dB higher [110]. While the galactic background remains also for an alternative antenna, one half of the noise N_{rms}^2 in terms of power would be suppressed by a factor of ten in its relative contribution. This effectively reduces the noise to $N'^2 = (\frac{1}{2} + \frac{1}{2} \cdot \frac{1}{10})N_{\mathrm{rms}}^2 = \frac{11}{20}N_{\mathrm{rms}}^2$. Such a decrease would also decrease the detection threshold S_{th} (see Eq. 6.5) with a minimum SNR of 10 from 90 µV/m to 65 µV/m. According to Eq. 6.13, the energy threshold is proportional to S_{th}, and will therefore decrease by about 30%, or 0.15 in $\lg E$.

As a side note, compared to other experiments, using antennas with higher gain, the effect on the energy threshold is additionally countered by the relative high magnetic field in the Tunka valley. The magnetic field is 20% weaker in central Europe, where LOPES [62], CODALEMA [63] and LOFAR [64] are located, and 60% weaker in Argentina, at the AERA [65] site.

Consequently, the gain is not a very limiting factor for the detection threshold of Tunka-Rex and the SALLA should not be discarded prematurely for future antenna arrays.

Conclusion

The model described in this section enables the determination of detection thresholds with respect to energy and event geometry. It has been developed for Tunka-Rex and was successfully tested versus data. To tune it for other experiments, the parameters from Tab. 6.1 have to be determined accordingly.

Contrary to most air-shower detection techniques, a radio detector benefits from being located further away from the air shower, e.g., for events at higher zenith angles. Within the given limits, this can be understood with simple geometric projections.

The energy threshold of Tunka-Rex is around $10^{16.9}$ eV and cannot be pushed significantly below $10^{16.7}$ eV due to the limit given by the galactic background. In particular, an antenna with higher gain would lower the energy threshold only marginally. Depending on how much the effective detector area and phase space is cropped, full efficiency can be reached between 10^{17} eV and $10^{18.2}$ eV. These thresholds are needed for an unbiased measurement of comic-ray properties, as planned in the next stage of Tunka-Rex.

The obtained thresholds are based on averages over multiple shower geometries. However, the model can also be used to cut the detector area dynamically, depending on the incoming direction and energy of an air shower, if a first reconstruction iteration is available from a host or auxiliary cosmic-ray detector. Such an event selection maximizes the efficiency. Additionally, because the cut is based on the expected signal, and not on the measured one, a selection bias can be avoided by choosing a conservative threshold. This can for example be achieved by setting the SNR requirement for r_{th} above the actual SNR threshold used for antenna selection.

Such an approach is especially useful, if an analysis is limited by purity, because only events which are expected to be above the detection threshold are selected. This method is demonstrated in Sec. 7.1, where an energy reconstruction with a single antenna station is presented.

7 The radio amplitude as an absolute energy scale

[1] Tunka-Rex measures the radio signal of air showers on an absolute scale. Due to the correlation between radio amplitude and air-shower energy, this enables a measurement of the absolute energy of air showers. Thus, the radio measurement can act as reference for the comparison of energy scales of different experiments, as well as for a cross-check of independent energy calibrations from other techniques.

The aim of this chapter is to demonstrate the capabilities of a radio detector for determining the absolute energy scale. First, a simplified energy reconstruction is introduced, which requires only a single antenna station. This enables an energy reconstruction with minimum detection thresholds. Next, the measured amplitude scale of Tunka-Rex is compared to CoREAS simulations, which is a benchmark for models of radio emission from air showers. Finally, the radio-amplitude scales of Tunka-Rex and LOPES are compared in order to compare the energy scales of the host experiments Tunka-133 and KASCADE-Grande.

7.1 Simplified energy reconstruction

The energy of an air shower E can be determined from the amplitude of the radio signal $S(r)$, described by the lateral distribution function of radio amplitudes (LDF). As discussed in Sec. 6.3.3, the radio amplitude at a fixed reference distance r_0 can be used as an energy estimator

$$E = \frac{S_{r_0}}{k}. \tag{7.1}$$

The calibration constant k describes the expected signal per energy at the distance to the shower axis r_0. The distance with maximum energy precision was found to be $r_0 = 120\,\mathrm{m}$ for Tunka-Rex [124]. Since the average antenna spacing of Tunka-Rex in shower coordinates is close to the optimal distance for energy estimation, there are usually antennas close to this distance. Therefore, the signal at $r_0 = 120\,\mathrm{m}$ is often interpolated from close-by measurements, which results in an energy estimation that is insensitive to details of the chosen LDF model. Thus, the approach for energy estimation can be further simplified.

---

[1] Publication of parts of this chapter is planned.

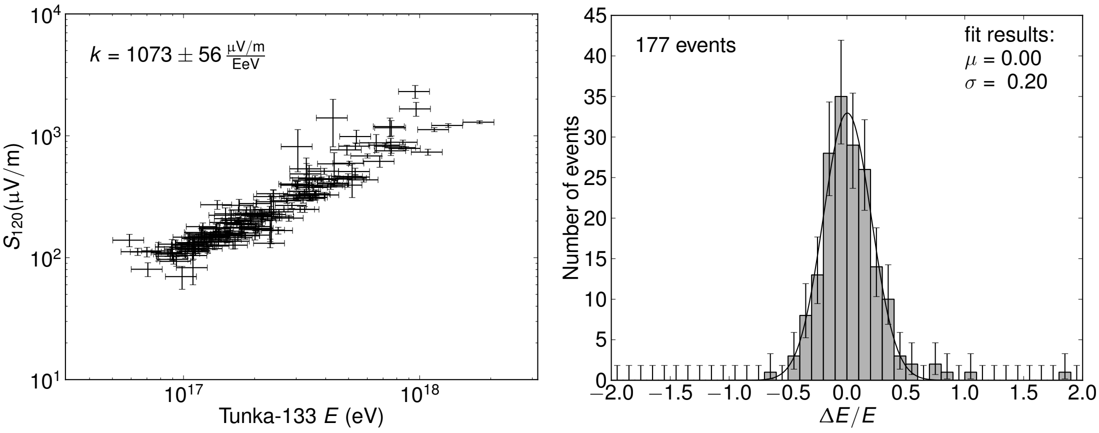

(a) (b)

Figure 7.1: (a) The reconstructed amplitude of the radio signal S_{120} at 120 m distance to the shower axis, corrected for the geomagnetic angle, correlates with the shower energy reconstructed by Tunka-133. (b) The residuals of this energy estimator are roughly Gaussian distributed with a standard deviation of 20%. This can be interpreted as the combined energy resolution of Tunka-Rex and Tunka-133.

Simple exponential LDF

In Sec. 6.3.3, it is demonstrated that a simple exponential LDF model, as in Eq. 6.4, is a good approximation for the distribution of asymmetry-corrected radio amplitudes. To determine the energy with a simple exponential LDF model, this model is fit to the distribution of radio amplitudes in the data set of the standard reconstruction (see Sec. 6.3). The correlation between S_{120} obtained from a simple exponential LDF and the energy reconstructed by Tunka-133 is depicted in Fig. 7.1. By fitting a normal distribution to the residuals of energy estimates from radio and air-Cherenkov measurements, the combined resolution of Tunka-Rex and Tunka-133 can be estimated from the obtained standard deviation. Assuming no correlation between the two energy estimators, the combined resolution is $20 \pm 2\%$ with a calibration constant of $k = 1073 \pm 56\,\frac{\mu\text{V/m}}{\text{EeV}}$. For the inner, dense core, i.e., for events within 500 m of the array center, it even increases to $17 \pm 2\%$. The same resolution, $17 \pm 2\%$, is obtained with the more complicated, extended LDF model, which requires parameter tuning to simulations or one additional antenna with signal [85]. Consequently, for the purpose of energy reconstruction with a sparse array, a simple exponential LDF is sufficient.

There are 5 outliers beyond the borders of Fig. 7.1 (a), which also appear in the standard reconstruction. One of these events is very far from the inner core (800 m), and thus, has a huge fitting error on S_{120} due to extensive extrapolation. Although far in terms of relative energy, it is only 1.2 sigma away from the calibration curve. Another

4 points are below $10^{16.5}$ eV and are probably false positive events because of the high number of trials at low energies. In the considered Tunka-133 data set of the first two seasons, out of 108207 events with an energy above 10^{16} eV, 108 pure background events are expected to pass the SNR cuts. They will mostly appear at low energies, due to the steep energy spectrum of cosmic rays. On average, 97% of the 108 events are deselected because of their random direction not fitting within 5° to the Tunka-133 reconstruction. This results in $3^{+2.9}_{-1.6}$ expected false-positive events, which is in agreement with the 4 events obtained at low energies.

Single antenna station

As discussed in Sec. 6.3.3, the energy estimator S_{120} represents the reconstructed electrical field, corrected for asymmetry and geomagnetic angle, at a distance of 120 m from the shower axis. If an antenna happens to be located directly at this distance, in principle no further measurements are required to determine the energy estimator. Using antennas further away from that distance introduces an additional uncertainty on the measurement. Still, since the resulting energy estimator is determined by a single antenna, the effective area of the detector can be increased and the energy threshold lowered. Naturally, such a method is only applicable in a hybrid detection system, where another detector proves triggering and geometry reconstruction. This information can be utilized for the energy reconstruction with a single antenna.

The measured signal at the antenna position systematically changes with increasing distance from the reference distance r_0, as described by the radio LDF. The simple exponential function (Eq. 6.4) is used for the extrapolation of the measured, asymmetry-corrected signal of an antenna station $S^{1\mathrm{A}}_{\mathrm{meas}}$ from the distance to the shower axis r to $r_0 = 120\,\mathrm{m}$

$$S^{1\mathrm{A}}_{120} = S^{1\mathrm{A}}_{\mathrm{meas}} \cdot \exp(\eta(r - 120\,\mathrm{m})). \tag{7.2}$$

With a single antenna station, the slope η cannot be fitted, therefore, the parametrization $\eta = \eta_0 \cdot \cos\theta$ from Eq. 6.10, with $\eta_0 = 8.2 \cdot 10^{-3}\,\mathrm{m}^{-1}$, as determined in Sec. 6.4, is used to obtain it as a function of zenith angle θ of the air shower. Although it varies from shower to shower typically on the order of $\sigma_\eta = 0.3 \cdot 10^{-2}\,\mathrm{m}^1$, the exact value of η_0 in the high-signal region, close to 120 m, does not limit the accuracy of $S^{1\mathrm{A}}_{120}$ for most events. With $\Delta r = r - 120\,\mathrm{m}$, the error on the extrapolated signal σ_{tot} is estimated by Gaussian error propagation from the contribution of the measurement uncertainty in the antenna station σ_{m}, and a contribution from the extrapolation

$$\sigma_{\mathrm{tot}} = \exp(\eta\Delta r) \cdot \sqrt{\sigma_{\mathrm{m}}^2 + (S^{1\mathrm{A}}_{\mathrm{meas}} \cdot \Delta r \cdot \sigma_\eta)^2} \tag{7.3}$$

σ_{m} arises mainly due to noise and is propagated according to the extrapolation procedure. The second contribution originates from the shower-to-shower fluctuations of η_0. Both contributions rise with increasing extrapolation distance Δr, with the second one rising faster. In Fig. 7.2 the measured signals with extrapolation and estimated error are

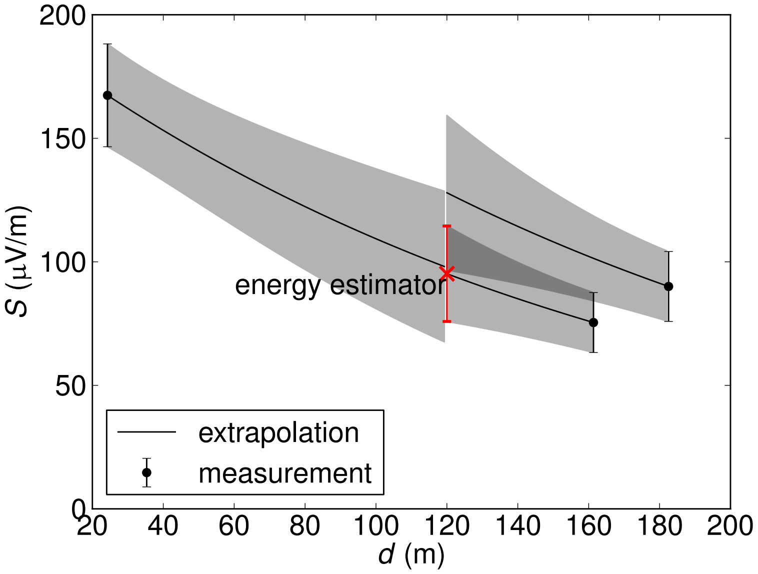

Figure 7.2: Example event from the standard reconstruction for the energy estimation with a single antenna. The energy estimator (red cross) is the signal at a distance of 120 m from the shower axis, which is extrapolated with a simple exponential function from a single measurement. If multiple antennas are available the one with the smallest uncertainty is chosen.

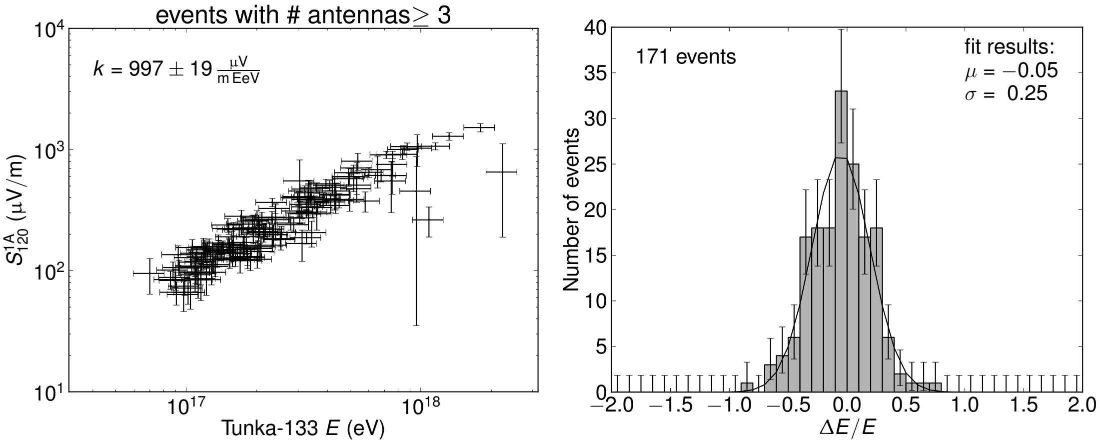

(a)

(b)

Figure 7.3: (a) Extrapolated electrical field from a single antenna station S^{1A}_{120} versus Tunka-133 shower energy for events of the standard reconstruction during the first two seasons (2012-2014). (b) Relative deviation of energies, reconstructed by Tunka-133 and Tunka-Rex.

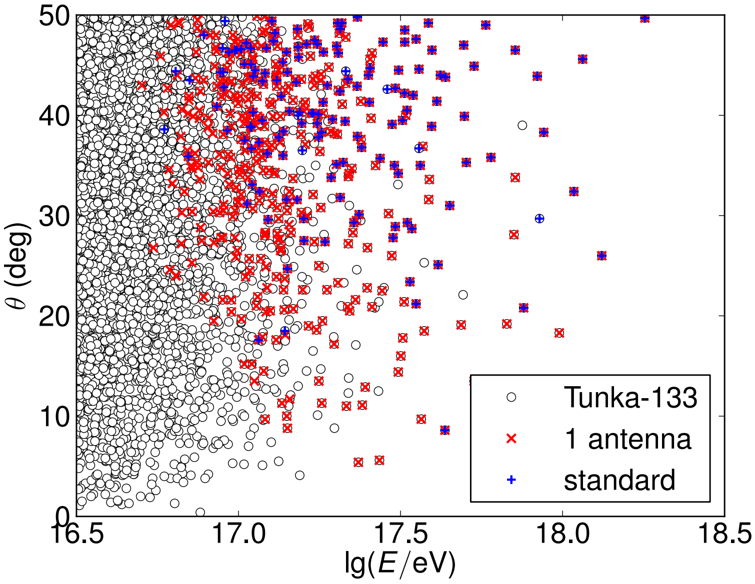

Figure 7.4: (a) Tunka-133 and Tunka-Rex events of the standard analysis and single antenna analysis for the first two measurement seasons 2012-2014. Only events with shower cores within 500 m from the array center are shown. The single antenna analysis enables radio measurements at lower energies and zenith angles. Tunka-133 and Tunka-Rex standard events are identical to Fig. 6.16.

shown for an example event with 3 antenna stations of the data set from the standard reconstruction.

To prove the method and the validity of the approximations, the method was first tested on the data set obtained from the standard reconstruction, comprised of events with comparatively high reconstruction quality, high purity and at least 3 antennas. For the shower core and the incoming direction, which is needed for signal reconstruction, the reconstructed values from Tunka-133 were used. From all available antennas passing SNR ≥ 10, the one with minimum estimated uncertainty according to Eq.7.3 was chosen. If an antenna did not pass the SNR threshold, all antennas further away were ignored.

In Fig.7.3 (a) the estimated radio amplitude $S_{120}^{1\mathrm{A}}$ versus energy from Tunka-133 is shown and in (b) the distribution of relative deviation of the energy estimator. The event selection contains 6 events less than the standard selection. All 6 events are very close to the detection threshold: Two of these events have no signal in the closest antenna station, possibly due to noise fluctuations, and therefore, all further stations were discarded. The remaining 4 events have 3 stations passing the SNR cut, but the expected signal in all antennas is below the threshold. The antennas in these events closely failed the cut on r_{th}, and probably passed the SNR cut due to noise fluctuations. The calibration constant, i.e., the signal amplitude per energy from Eq. 7.1, is $k = 997 \pm 19\,\frac{\mathrm{\mu V/m}}{\mathrm{EeV}}$. It

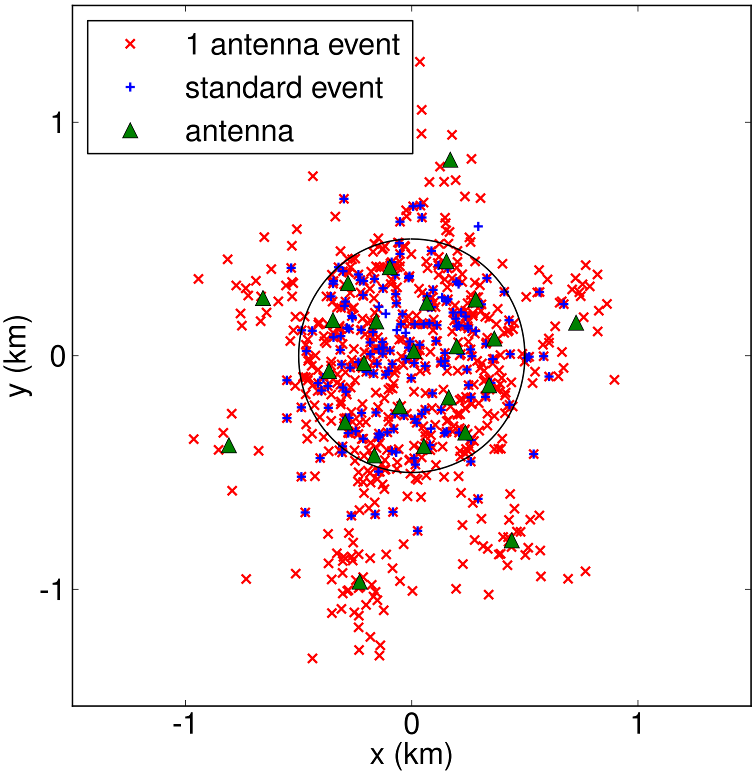

Figure 7.5: Core distribution of events from the standard analysis and single-antenna analysis. The circle indicates 500 m distance from the array center. The single-antenna analysis extends the effective detector area beyond the borders of the central, dense array, where standard event numbers decline. Thus, it enlarges the effective detector area, also increasing event statistics for the high energies.

differs only marginally from the one obtained with the standard reconstruction with the simple exponential LDF. Thus, there is no significant, additional selection bias due to the single-adntenna method. From a Gaussian fit to the residuals, a combined precision for the energy reconstruction of Tunka-Rex and Tunka-133 of $25 \pm 2\%$ is obtained, slightly worse than the 20% when using at least 3 antennas.

Coming back to the full Tunka-133 data set the main problem of the single antenna analysis is the purity of the event selection. The requirement for coincidences of at least 3 antennas heavily suppressed the occurrence of false-positive events in the standard reconstruction. Therefore, a geometric cut is introduced, to select only antennas expected to pass the single-antenna threshold of $\mathrm{SNR} = 10$. According to the threshold model, developed in Sec. 6.4, only antennas with distances from the shower axis below r_{th} (see Eq. 6.12) are selected. Energy, geomagnetic angle and zenith angle needed for the cut are taken from the Tunka-133 reconstruction. This requirement is an energy dependent

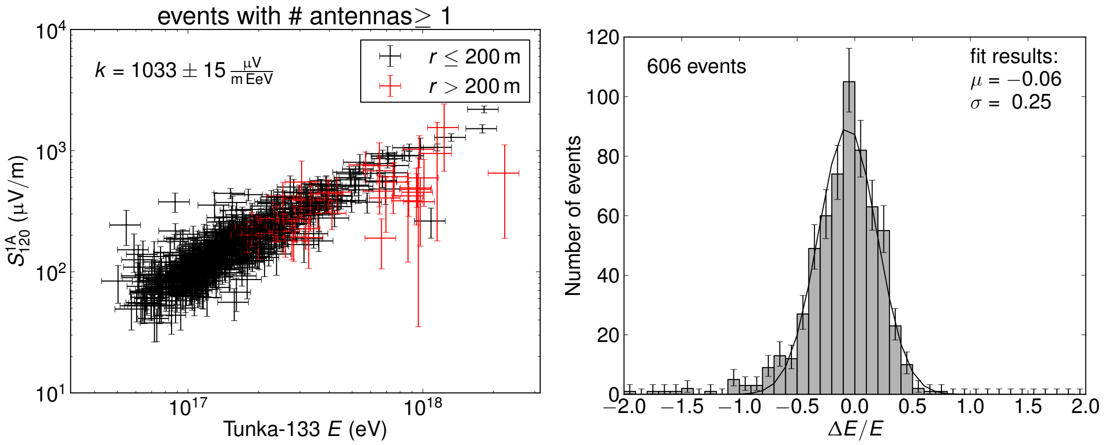

(a) (b)

Figure 7.6: (a) Single-antenna energy estimator versus Tunka-133 shower energy, also for events with only one or two antennas with signal. Events expected to surpass the radio detection threshold are preselected using the energy and shower geometry reconstructed by Tunka-133. From a fit to (b), the relative deviation of the energy reconstructed with Tunka-133 and Tunka-Rex, a combined energy precision of 25% is obtained for antennas closer than 200 m.

cut on zenith angle, geomagnetic angle and effective detector area.

649 events are obtained for the single antenna analysis from the first two measurement seasons (2012-2014), more than three times as many as for the standard reconstruction. In Fig. 7.4, the resulting event selection is shown as a function of energy and zenith angle, for both, the events from Tunka-133 and the Tunka-Rex standard selection, but only for events located within 500 m from the array center. The energy threshold decreased to $10^{16.7}$ eV, and significant event numbers are detected also at zenith angles below 30°.

In Fig. 7.5, the shower core distribution of standard and single antenna events is shown. While the standard event number declines already towards the borders of the central, dense array, the single antenna events extend further, according to r_{th} typically by 100-200 m. Even at very far distances, around the outer stations, where no standard events pass the threshold, significant event numbers are obtained. This is especially important for the very high energies, because the sparser outer array greatly extends the effective detector area for these events.

In Fig. 7.6, the resulting energy estimator as a function of Tunka-133 energy and its residuals is shown. While the estimator generally follows the Tunka-133 energy, there are some outliers caused by events far from the central array. This might be a consequence of the exponential LDF model, which overestimates signal amplitudes far from the core (see Sec. 6.3.3), which is a problem that can be solved, e.g., by applying a different LDF model. Alternatively, restraining the maximum antenna distance to the shower axis to 200 m, these events can be deselected. For this subset of 606 events with a maximum distance of 200 m, the following results are obtained: The calibration constant is $k = 1033 \pm 15 \, \frac{\mu\mathrm{V/m}}{\mathrm{EeV}}$. Compared to the standard reconstruction with a simple exponential LDF, k is only marginally different. This indicates that there is no significant, additional selection bias due to the single-antenna method. The combined precision of Tunka-Rex and Tunka-133 is 25 ± 1%. Assuming the energy estimator of Tunka-133 to have a precision of 15% [8] with fluctuations fully independent of $S_{120}^{1\mathrm{A}}$, an energy resolution of 20% can be reached for Tunka-Rex with $S_{120}^{1\mathrm{A}}$.

This method is especially useful if the host experiment has an energy resolution worse than 20%, or if the energy reconstruction of the host experiment features large systematic uncertainties, e.g., due to a dependence on the primary particle type. This is, for example, the case for many cosmic-ray detectors based on scintillators [90]. In particular, the method might be useful for a combined analysis of Tunka-Rex and Tunka-Grande in the next seasons.

7.2 Comparison of Tunka-Rex measurements to CoREAS simulations

[2] While there are many different simulation codes for the radio emission from air showers, the latest generation of models starts to converge, and generally agrees on the order of magnitude of radio emission [67]. Still, the models were subject to significant changes in the last decade, e.g., by reevaluation of important factors for the radio emission like the refractive index of air [76, 73]. With absolute calibrated radio experiments, such as Tunka-Rex, these models can be tested.

However, even in the latest generation of radio experiments, discrepancies remained between different calibrated radio experiments: While LOPES, calibrated in the last decade, seemed to agree with the REAS 3.11 plug-in for the CORSIKA simulation code for air showers, AERA confirmed the upgraded CoREAS 1.0 simulation, which is directly implemented in CORSIKA. Simulations from these two software packages predicted radio amplitudes which differed by a factor of 2 [78, 79].

Using the recalibrated reference source of LOPES, this discrepancy was resolved in the context of this work by providing a common calibration scale for Tunka-Rex, LOPES and LOFAR. The old calibration of LOPES was found to be performed under wrong assumptions, and the update brought LOPES measurements of the radio signal into agreement with CoREAS simulations within uncertainties [1].

A similar test was also performed for Tunka-Rex. For this purpose, an available CoREAS simulation data set of high-energy events of the first season was used [120]. The simulations were performed with CoREAS [73] and the hadronic interaction model QGSJET-II.04 [127], using geometry and energy from the Tunka-133 reconstruction as input. The depth of the shower maximum cannot be set as a parameter in the simulations, but emerges from other parameters and random fluctuations. To select simulations

---

[2] Parts of this section have been published in Ref. [66]

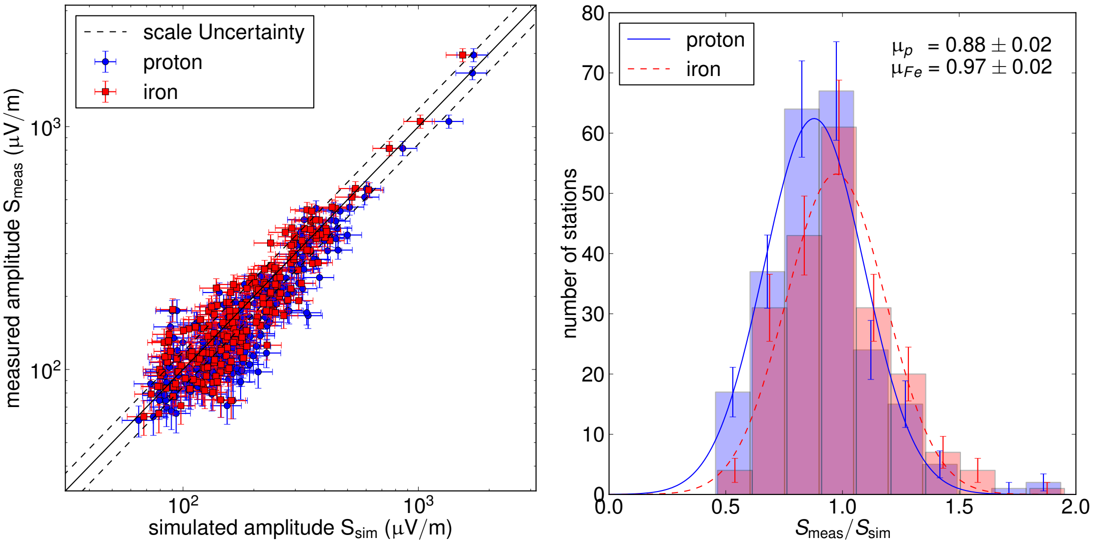

(a)

(b)

Figure 7.7: (a) Reconstructed amplitudes from Tunka-Rex versus predictions from air-shower simulations with CoREAS. Horizontal error bars indicate the energy uncertainty from Tunka-133, while vertical ones indicate measurement uncertainties on the amplitudes due to background. (b) Distribution of the amplitude ratio for proton and iron primary particles. An uncertainty of 17% on the mean arises from the calibration.

with depths of shower maximum similar to the measured showers, a quick and rough presimulation with CONEX [128] was performed to find random seeds resulting in the atmospheric depth of the shower maximum deviating by not more than 30 g/cm^2 from the Tunka-133 reconstruction.

370 and 426 simulation were performed for proton and iron primary particles respectively. These simulations underwent a detector simulation, that includes the system response of the antenna station and digitization. Then, measured background was added in terms of ADC counts. The simulated events were reconstructed with the standard reconstruction algorithm. Only events passing all selection criteria of the standard reconstruction were considered. So both, the measured and the simulated event had to pass all selection criteria. 53 proton and 46 iron events survived, with a total of 232 and 202 antenna stations above threshold, respectively.

The measurement of each individual antenna can be compared with its simulated counterpart. Results are shown in Fig. 7.7. Measurement and simulation generally follow each other on average, which indicates an agreement of the two. By fitting a normal distribution to the ratio of measured to simulated amplitudes, a mean of 0.88±0.08 for proton and 0.97±0.02 for iron is obtained. This deviates by less than the scale un-

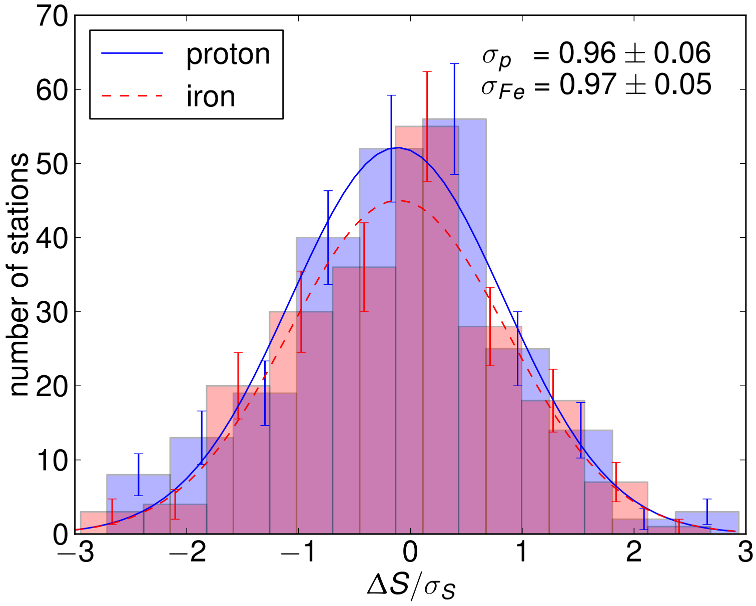

Figure 7.8: Deviation of amplitudes measured with Tunka-Rex and simulated with CoREAS, for proton and iron primaries, divided by the estimated uncertainty (data set as in Fig. 7.7). Data was scaled according to the mean ratio from Fig. 7.7 to fit to the simulation on average. The resulting distribution is compatible with a standard normal distribution, which indicates an agreement between estimated uncertainties and observed spread.

certainty of 17% from 1, confirming CoREAS simulations within uncertainties. Other uncertainties average out over multiple events and antennas. They consist of the measurement uncertainties due to noise, a 15% uncertainty from the Tunka-133 energy resolution and antenna-to-antenna and event-to-event fluctuations of Tunka-Rex of 13% (cf. table 5.1). In Fig. 7.8, the distribution of deviations between data and simulation, in normalized to the estimated uncertainty is shown, after the data was scaled according to the mean ratio. The resulting distribution is approximately a standard normal distribution, which means that the observed spread is as expected from the individual measurement uncertainties.

7.3 Comparison of energy scales via radio measurements

There are several calibrated experiments currently operating in the 30-80 MHz frequency band: Tunka-Rex, LOPES, LOFAR and AERA. Their amplitudes are comparable on an absolute scale. Tunka-Rex, LOPES and LOFAR were even calibrated with the same reference source in the scope of this work. As such, they can be compared to each other without the dominating 16% calibration uncertainty of the reference source.

LOFAR has not published a measurement of the amplitude scale yet. AERA published a measurement of the radio signal scale, but it is based on an integration over a two dimensional LDF parametrization. This recently published method [86] significantly differs from Tunka-Rex techniques, and therefore, cannot be compared in the framework of the current analysis.

The LOPES collaboration published a calibrated measurement of radio amplitudes versus energy [84]. Furthermore, as discussed in Sec. 5.6, the amplitude scale of LOPES is consistent with Tunka-Rex, because the same reference source was used for calibration. Thus, LOPES and Tunka-Rex were chosen to explore the capabilities of the radio technique for the comparison of absolute energy scales.

The reconstructed signal of LOPES was bandlimited to 43 to 74 MHz, and only the signal in the east-west aligned antenna was evaluated. To check it versus Tunka-Rex, the results of LOPES were revised with the updated calibration [129]: a simple exponential function (see Eq. 6.4) was used as the LDF model to reconstruct the amplitude at a distance of 100 m from the shower axis, normalized to $\sin\alpha$, with the geomagnetic angle α. The event selection included 125 events with zenith angles between 30° and 45°, which fell into the KASCADE field, but with the energy reconstruction of KASCADE-Grande [3]. A median of $24.1\,\frac{\mu\mathrm{V/m}}{\mathrm{EeV\,MHz}}$ was obtained for the signal amplitude per energy, dominated by events close to 10^{17} eV. In the LOPES experiment, amplitudes are given normalized to the effective bandwidth of 31 MHz. Thus, to obtain actual measured amplitudes, the signal has to be multiplied by 31 MHz, resulting in $k_{100}^{\mathrm{LOPES}} = 747\,\frac{\mu\mathrm{V/m}}{\mathrm{EeV}}$ for the amplitude per energy. To account for the difference in magnetic field, this value is divided by 47 μT, the magnetic field strength at the LOPES site: $\kappa_{\mathrm{LOPES}} = 15.9\,\frac{\mu\mathrm{V/m}}{\mu\mathrm{T\ EeV}}$.

For comparison, a similar analysis of the signal was performed with Tunka-Rex data: The signal was bandlimited to 43-74 MHz and the reconstructed east-west component, normalized to $\sin\alpha$, was evaluated. Other selection criteria were left as in the standard reconstruction (see Sec. 6.3), resulting in events with zenith angles predominantly between 30° and 50°. The amplitude at 100 m distance was reconstructed with a simple exponential LDF (see Eq. 6.4) and normalized to $\sin\alpha$. The resulting amplitude versus energy is shown in Fig. 7.9. The median of the obtained amplitude per energy is $k_{100}^{\mathrm{TRex}} = 856 \pm 20\,\frac{\mu\mathrm{V/m}}{\mathrm{EeV}}$. Thus, normalizing to the magnetic field strength of 60 μT results in $\kappa_{\mathrm{TRex}} = 14.27 \pm 0.33\,\frac{\mu\mathrm{V/m}}{\mu\mathrm{T\ EeV}}$.

To compare the obtained values to each other, the difference in observation depth between Tunka-Rex and LOPES has to be taken into account. LOPES was located at a vertical observation depth of $1022\,\mathrm{g/cm}^2$, while Tunka-Rex is at $955\,\mathrm{g/cm}^2$. To estimate the magnitude of the impact on the signal strength, Eq. 6.11, introduced in Sec. 6.4, from the geometrical projection model of the radio footprint is used. A vertical shower for LOPES is at the same observation depth as a 22° inclined shower at Tunka. For the more inclined showers, the difference in zenith angle shrinks: for zenith angles of 30° and 45°, the corresponding angles for Tunka are 36° and 49°, with a 2% and

---

[3] The energy reconstruction of KASCADE-Grande is not tuned to this event selection, which might cause additional systematic uncertainties on the order of 10%.

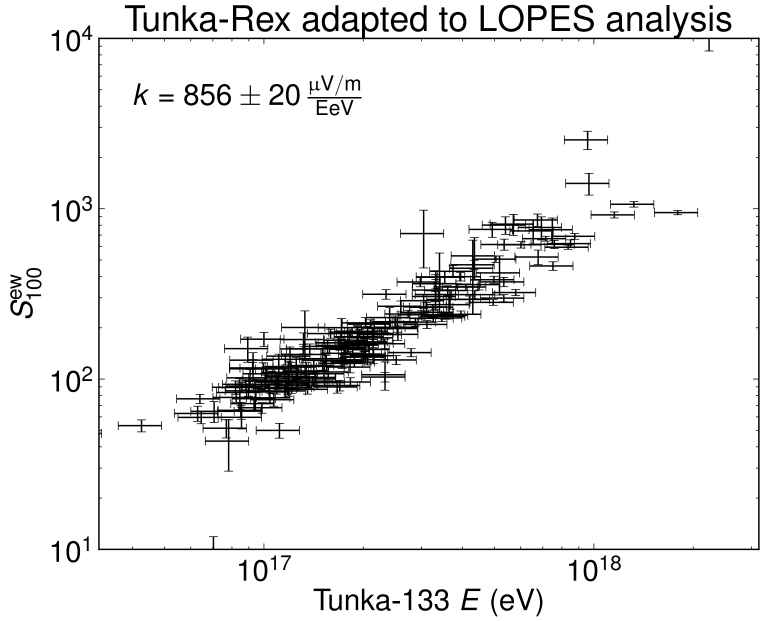

Figure 7.9: Energy estimator resembling the method of the LOPES experiment: the amplitude of the east-west component of the radio signal at 100 m distance from the shower axis is reconstructed with an exponential radio LDF model. The signal is bandlimited to 43-74 MHz.

3% expected deviation of the amplitude at ground, respectively. Overall, the expected average deviation between LOPES amplitudes at zenith angles between 30° and 45° and Tunka-Rex amplitudes at zenith angles between 30° and 50°, is 3%, which is below the statistical significance of the measurement. Consequently, the obtained coefficients κ_{TRex} and κ_{LOPES} can be directly compared to each other.

The reconstructed energy E_{m} from either experiment may have a systematic shift compared to the real energy E_{real}. As such, the measured coefficient κ_{m} deviates from the real on κ_{real}

$$\kappa_{\mathrm{m}} = \frac{E_{\mathrm{real}}}{E_{\mathrm{m}}} \cdot \kappa_{\mathrm{real}} \tag{7.4}$$

Thus, the energy scales of Tunka-Rex and LOPES and their hosts, KASCADE-Grande and Tunka-133, can be compared using the radio measurements of κ_{m}

$$f_{\mathrm{amp}} = \frac{E_{\mathrm{KG}}}{E_{\mathrm{T133}}} = \frac{\kappa_{\mathrm{TRex}}}{\kappa_{\mathrm{LOPES}}}. \tag{7.5}$$

The resulting ratio of reconstructed energies is $f_{\mathrm{amp}} = 0.90 \pm 0.08$. Uncertainties arise due to the measurement (each around 3%), 7% from the calibration, and 3% from the difference in observation depth, all added in quadrature.

Another way to compare LOPES to Tunka-Rex is by using CoREAS simulations as a benchmark. The simulation take the difference in magnetic field and observation depth

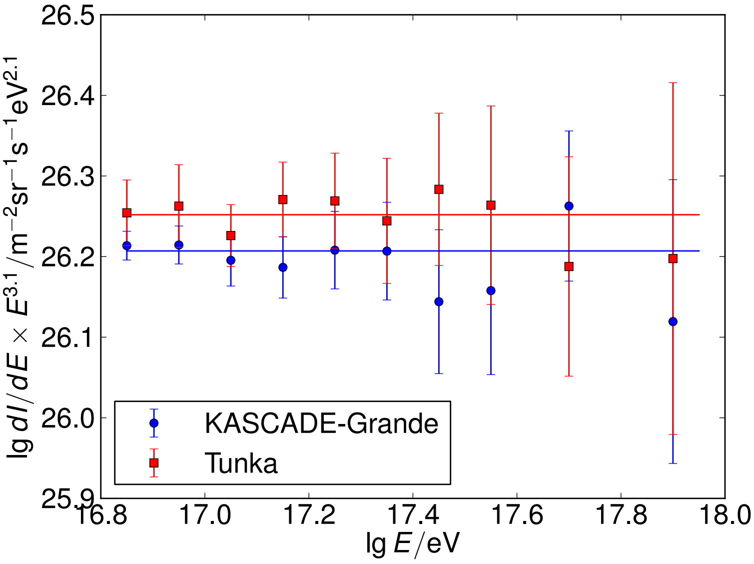

Figure 7.10: Energy spectra of cosmic rays from KASCADE-Grande [130] and Tunka-133 [8] in the energy range also observed by Tunka-Rex. With a systematic increase of KASCADE-Grande energies by 4%, the scales of both spectra, defined by a fit to a power law with spectral index 3.1 (horizontal lines), can be brought to match.

into account. The LOPES collaboration reported the mean ratio between measured and simulated amplitudes at 100 m to be $F^{\mathrm{p}}_{\mathrm{LOPES}} = 0.98$ for proton and $F^{\mathrm{Fe}}_{\mathrm{LOPES}} = 1.09$ for iron primaries [1]. With Tunka-Rex measurements, a ratio of $F^{\mathrm{p}}_{\mathrm{TRex}} = 0.88 \pm 0.02$ for proton and $F^{\mathrm{Fe}}_{\mathrm{TRex}} = 0.97 \pm 0.02$ for iron primaries was obtained (cf. Fig. 7.7). A systematic shift in energy propagates to the simulations, which use the energy reconstructed by the host experiment as input:

$$F = \frac{E_{\mathrm{real}}}{E_{\mathrm{m}}} \cdot F_{\mathrm{real}} \tag{7.6}$$

A possible constant scale mismatch between CoREAS and nature F_{real} cancels out, because Tunka-Rex and LOPES are compared to the same version of CoREAS. Thus, the derived ratio of energy scales is

$$f^{\mathrm{sim}} = \frac{E_{\mathrm{KG}}}{E_{\mathrm{T133}}} = \frac{F_{\mathrm{TRex}}}{F_{\mathrm{LOPES}}}. \tag{7.7}$$

The obtained ratios of scales are $f^{\mathrm{p}}_{\mathrm{sim}} = 0.90 \pm 0.10$ and $f^{\mathrm{Fe}}_{\mathrm{sim}} = 0.89 \pm 0.10$. The uncertainties include the statistical uncertainty of 2%, 7% from the calibration, and 5% from the method, all of which are added in quadrature. The uncertainties of the method arise because the ratio F_{TRex} varies by around 5%, depending on details of analysis, such

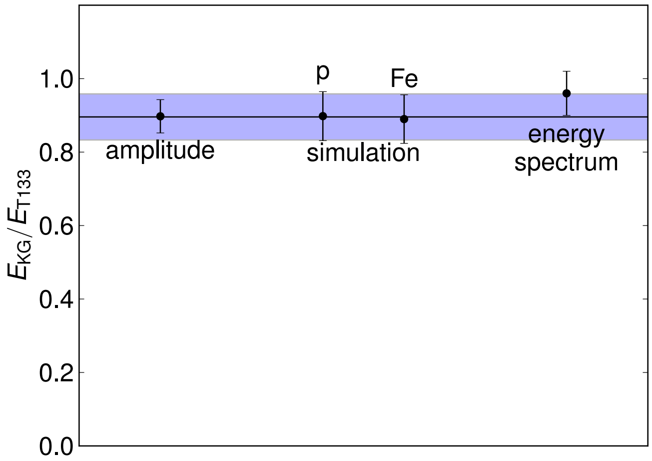

Figure 7.11: Results from the comparison of energy scales between the experiments Tunka-Rex and LOPES. The blue band indicates the scale uncertainty of the amplitude calibration, which is correlated for all radio measurements. The energy scales are compared via amplitude measurements directly, as well as via the relative deviation of amplitudes to CoREAS simulations with proton and iron primaries, and offsets in the energy spectra.

as bandwidth and chosen LDF model, which were not matched in this analysis. Further systematic uncertainties might apply from a zenith angle dependence of F_{LOPES} [131], but were not investigated closer in this analysis.

Overall, it can be concluded that the accuracy of the comparison can reach around 10%, if systematic uncertainties of the analyses can be resolved, which are not constitutional to the method. No significant deviation was found with both methods, thereby confirming the consistency of the energy scales of KASCADE-Grande and Tunka-133 to an accuracy of about 10%.

To cross-check this claim, published energy spectra of KASCADE-Grande [130] and Tunka-133 [8] were compared in the energy range $10^{16.8}$ eV to 10^{18} eV. They are shown in Fig. 7.10. Assuming a simple, constant energy shift between the two experiments, and given that both experiments measure the same cosmic-ray spectrum, the spectra can be brought to match by shifting the KASCADE-Grande energy upwards by 4%, i.e., $f_{\mathrm{spec}} = 0.96 \pm 0.06$. The deviation is not statistically significant, and thus, confirms the result obtained by the radio measurements: the energy scales of KASCADE-Grande and Tunka-133 are consistent and differ at most marginally, on the order of 10%. The obtained results are summarized in Fig. 7.11.

This analysis shows how energy scales of different air-shower experiments can be independently checked against each other by using an accurately calibrated radio detector. The radio measurements can be used, in turn, to calibrate air-shower detectors or to combine and compare data from different experiments on a common energy scale.

8 Conclusion

In this work, the Tunka-Rex experiment was calibrated in order to obtain a measurement of the absolute amplitude scale of the radio emission from cosmic-ray air showers. This lead to the development of new methods for the competitive application of the radio technique in cosmic-ray physics.

The Tunka-Rex experiment is a radio detector for cosmic-ray air showers close to Lake Baikal in Siberia, Russia. It was deployed in 2012, during the time frame of this work, and started operation in the same year. Its host experiment, Tunka-133, is an air-Cherenkov detector for air showers, providing trigger and a precise reconstruction of cosmic-ray events. The goal of Tunka-Rex was to advance methods and understanding of the radio-detection technique and to demonstrate its benefits and limitations when operated in combination with an established detection method.

The determination of the absolute scale of radio emission with a calibrated antenna array has been pursuit for a long time. The antenna calibration turned out to be a key issue in this effort. High-frequency electronics as well as antennas are very sensitive to details of the measurement. Thus, it is very challenging to attain well defined calibration conditions. Tunka-Rex has acquired an absolute amplitude calibration to an accuracy of 22%. Furthermore, in a collaborative effort, Tunka-Rex, LOPES and LOFAR were calibrated consistently, with significant contributions to all three campaigns in the scope of this thesis.

The measurement of radio emission close to its threshold of around $10^{17}\,\mathrm{eV}$ is a challenging problem experienced by all radio experiments since none of them operate at significantly higher energies. Tunka-Rex demonstrated that this challenge can be approached with modern methods of signal processing and exemplarily showed how background and signal thresholds can be treated. Its simple design demonstrated the feasibility and advantages of an economic detector. For example, the advantages of the SALLA antenna, which are its simple, rugged design, and low dependence on ground conditions, outweigh the slightly increased threshold due to its comparatively low gain.

One of the main advantages of the radio technique is its high duty cycle of almost 100%. Until now it appeared that the high duty cycle is partially countered by a low efficiency and complex acceptance of the detector. This problem was investigated by developing a model to describe the non-trivial, geometry-dependent thresholds and testing the model with Tunka-Rex data. It was found that Tunka-Rex becomes fully efficient between 10^{17} eV and $10^{18.2}$ eV, depending on the arrival direction of the shower. With the standard event selection, events with energies above $10^{17.5}\,\mathrm{eV}$ and high zenith angles can be used for physics analyses. With the presented model, air showers can be selected dynamically with additional information from the host experiment. Thus, the threshold can, in principle, be lowered close to 10^{17} eV.

Furthermore, a method was developed to reconstruct the air-shower energy using signal from a single antenna station only. With an energy precision of better than 25% it is only marginally worse than the standard method, which has a resolution of about 20% and requires at least 3 antennas. With these reduced requirements, the energy threshold is pushed below 10^{17} eV and the acceptance is increased, thus providing 3 times higher statistics. Together with the spectral-slope method [132] for the reconstruction of the depth of shower maximum, this might enable an air-shower reconstruction with the radio technique based on a single antenna station. Thus, this method potentially reduces the costs for a radio extension by a factor of 3.

A theoretical understanding and modeling of the signal is elementary for any application of the radio technique. In the 2000s, differences between models for radio emission from air showers, as well as order-of-magnitude changes from version to version were still common. However, in the last years, the models converged and now agree on the amplitude scale. Utilizing the calibrated air-shower measurements of Tunka-Rex, it was shown that radio signals from measured air showers agree to air-shower simulations with the CoREAS simulation code to an accuracy of 17%. This result can be used as a benchmark for other models and confirms the current understanding of radio emission in air showers to this accuracy level.

Furthermore, with the absolute measure of the radio signal, energy scales of different experiments can be checked and compared independently. For experiments calibrated with the same reference source, this comparison yields an accuracy of about 10%. Comparing the amplitude scales of the radio experiments Tunka-Rex and LOPES, it was shown that the energy scales of their hosts, Tunka-133 and KASCADE-Grande, are consistent to 10%. This reduces systematic uncertainties when comparing or combining data of different experiments.

The future plans for Tunka-Rex are to contribute to scientifically relevant cosmic-ray measurements, e.g., for the depth of the shower maximum as a function of energy. This will be achieved by combining Tunka-Rex with Tunka-Grande, the scintillator extension of Tunka-133. From the measurement season of 2015/2016 on, Tunka-Rex will be triggered also during daytime by Tunka-Grande, thereby exploiting the full potential of its high duty cycle. With this setup, Tunka-Rex can be used to explore the capabilities of a combination between a scintillator array and a radio array. The radio array can enhance the energy resolution and provide additional composition discrimination. In particular, Tunka-Grande will be calibrated on the energy scale provided by Tunka-Rex.

As other detector types perform better for triggering, the future of the radio technique remains in hybrid detection systems. Since single detection systems are already exploited to their limits, further results are almost exclusively obtained by combining multiple detectors. The radio technique is a promising candidate for a part of such a system at a low price. With growing understanding of the radio-signal scale, its potential use in cosmic-ray measurements can finally be exploited. Given the accuracy, also reached by Tunka-Rex, radio measurements provide an option for energy calibration of all detectors on a common, absolute scale.

A Supplementary calibration measurements

A.1 Temperature dependence of the filter amplifier

The temperature dependence of one filter amplifiers was measured together with the temperature dependence of one low-noise amplifier and one 29.9 m RG213 cable. The procedure is explained in Sec. 5.7. During Tunka-Rex measurements, the filter amplifiers are usually heated to 18 to 25 °C inside the cluster centers of Tunka-133. Thus, the temperature dependence of the filter amplifier can currently be neglected for signal reconstruction. In case this changes for future applications, the measurement results are shown in Fig. A.1. The gain rises systematically by about 0.3 dB over the whole band, when decreasing the temperature from 20 to -30 °C. The phase remains stable over the whole temperature range.

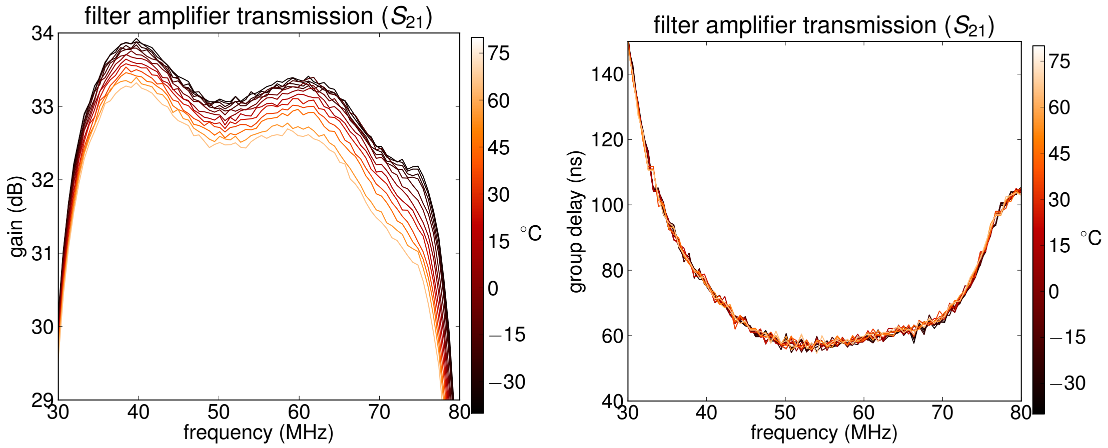

(a)

(b)

Figure A.1: Temperature dependence of (a) the gain and (b) the group delay of the forward response for the filter amplifier. Usually the filter amplifiers are located inside heated electronics boxes, with a temperature between 18 and 25 °C.

A.2 Vector effective length from the antenna calibration

The remaining calibration measurements for the antenna station at different zenith angles, not shown in Sec. 5.5, are depicted in Fig. A.2. The full calibration procedure is explained in Sec. 5.5.

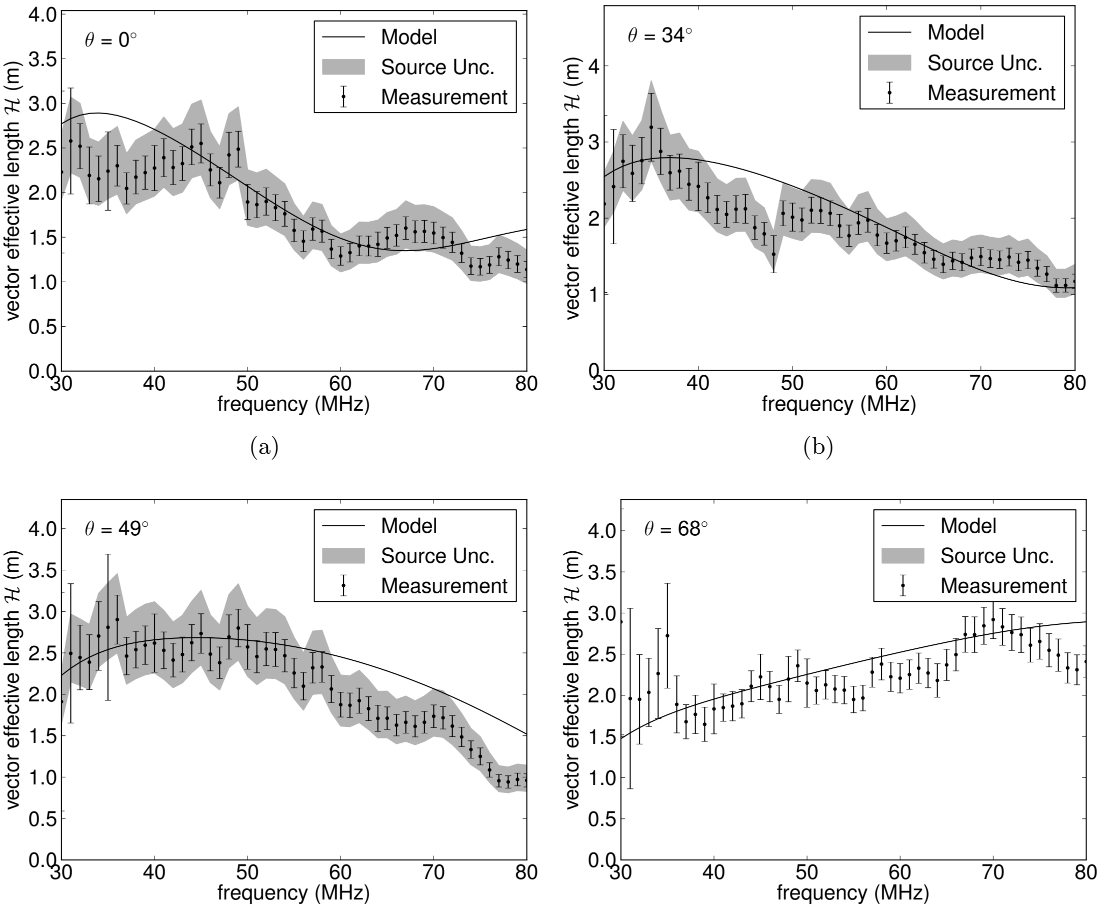

(a) (b)

(c) (d)

Figure A.2: Calibration results for the absolute value of the vector effective length $\mathcal{H}$ of the SALLA at zenith angles of (a) 0°, (b) 34°, (c) 49° and (d) 68°.

B Configuration for NEC2 antenna simulations of the SALLA

For the simulation of the SALLA with the 4NEC2 antenna-simulation code [115], the field of an excited, conductive arc of 0.6 m radius at a height of 2.33 m (lowest segment) is simulated. The lowest element is loaded with a parallel 390 Ω resistance and a 3.3 μH inductivity. The selected ground originates from the preconfigured selection in 4NEC2 with the name ”marshy”, corresponding to a relative dielectric constant of 12 and a conductivity of 8 mS/m. The arc is excited at the highest segment with a current source of 1 A amplitude. The configuration file is:

```
CM SALLA
CM
CE
GA 1 100 0.6 -270 90 0.005
GM 0 0 0 0 0 0 0 2.33 1
GE 1
LD 1 1 50 50 390 0.0000033 0
GN 2 0 0 0 12 0.008
EK
EX 6 1 1 0 1 0 0
FR 0 0 0 0 50 0
WG salla_geom
EN
```

The elements of the configuration stand for:
CM comment
GA adds an arc of wires
GM moves the arc to the proper height above ground
LD adds a load
GN defines the ground
EX defines the source of excitation
FR specifies the frequency, but is ignored in the frequency sweep mode used for this simulation
EK extended thin-wire kernel for simulating non-infinite thin wires
CE GE and EN mark the end of input sections

C Calibration sheet of the reference source VSQ1000

On the following pages, a scan of the calibration sheet for the reference source VSQ1000 by Teseq is attached. This is the reference source, which was used for the calibration of the Tunka-Rex antenna station, described in Sec. 5.5.

Certificate N° Zertifikat Nr.	**A021060/057**	Page Seite	**1**	of von	**5**	pages Seiten

Customer Kunde	**KIT** **Karslsruher Institut für Technologie** **76344 Eggenstein-Leopoldshafen**	Order N°, date Auftrags-Nr., Datum	**254/20588347/** **IKP/GFB** **29.01.2015**

Certificate of Calibration - Kalibrierzertifikat

Object Gegenstand	**Reference Radiation Source**
Manufacturer Hersteller	**SCHAFFNER**
Model Typ	**VSQ 1000 consisting of RSG 1000 ; DPA 4000**
Serial N° Serien-Nr.	**20563; 18138**
Remarks Bemerkungen	**special Frequency range 30-100 MHz; 1 MHz Step; Free Space**
Date of calibration Datum der Kalibrierung	**03 February 2015**

This calibration certificate documents the traceability to national standards, which realize the physical units of measurements (SI).
Dieses Kalibrierzertifikat dokumentiert die Rückführbarkeit auf nationale Normale zur Darstellung der physikalischen Einheiten (SI).

The measurements, the uncertainties with confidence probability and calibration methods are given on the following pages and are part of the certificate.
Messresultate, Messunsicherheiten mit Vertrauensbereich und Messverfahren sind auf den folgenden Seiten aufgeführt und sind Teil des Zertifikates.

Place and date Ort und Datum	The Calibration Laboratory Die Kalibrierstelle	Person in charge Bearbeiter
Berlin, 23 February 2015	.... U. Karsten	.... T. Görl

This certificate shall not be published or reproduced other than in full.
Der Inhalt dieses Zertifikates darf nur in vollständiger Form veröffentlicht oder weitergegeben werden.
Calibration in line with EN ISO/IEC 17025 specifications

Calibration method:	The calibration method is defined in the VSQ 1000 calibration instruction. (see 1.1.)
Calibration equipment:	The entire equipment is connected to the respective primary laboratory and therefore directly traceable to national and international standards.
Uncertainty of measurements:	The reported expanded uncertainty of measurement is stated as the standard uncertainty of measurement multiplied by the coverage factor k = 2, which for a normal distribution corresponds to a coverage probability of approximately 95 %.
Validity :	This certificate is valid only if the VSQ 1000 is in use according to the standard.

Uncertainty of measurements

Electrical Field Strength	30 MHz ... 100 MHz	2.5dB

Calibration equipment

Device	Type	Serial number	Next calibration / Traceability / Certificate N° / Date
EMI Measuring Receiver	SMR 4518	016	02.2017 / D-K-15033-01-00 / 4231 / 02.2015
SAC	SAC3+	10107	05.2016 / UKAS 0392 / CS0434 / 05.2013
Antenna	VBA6106A	29750	12.2016 / UKAS 0392 / CA8003 / 12.2014

Calibration environment:	Room temperature	**22**	°C	± 1 °C
	Relative humidity	**45**	%	± 5 %

1. Description of the calibration method

1.1. Emission measurement of the VSQ in the SAC3+

The emission measurement will done in a standard 3m SAC (with reflectiv ground).
The results will recalculated to a 10m free field.

Note!
The reference point for the measurement is the middle point of the dipole antenna.

VSQ settings:

Frequency range : 1 MHz

Receiver settings:

Frequency range : 30 MHz to 100 MHz
Step size : 1 MHz
Bandwidth : 9 kHz
Detector : AV 20 ms

Details about the object under calibration

2. Calibration results

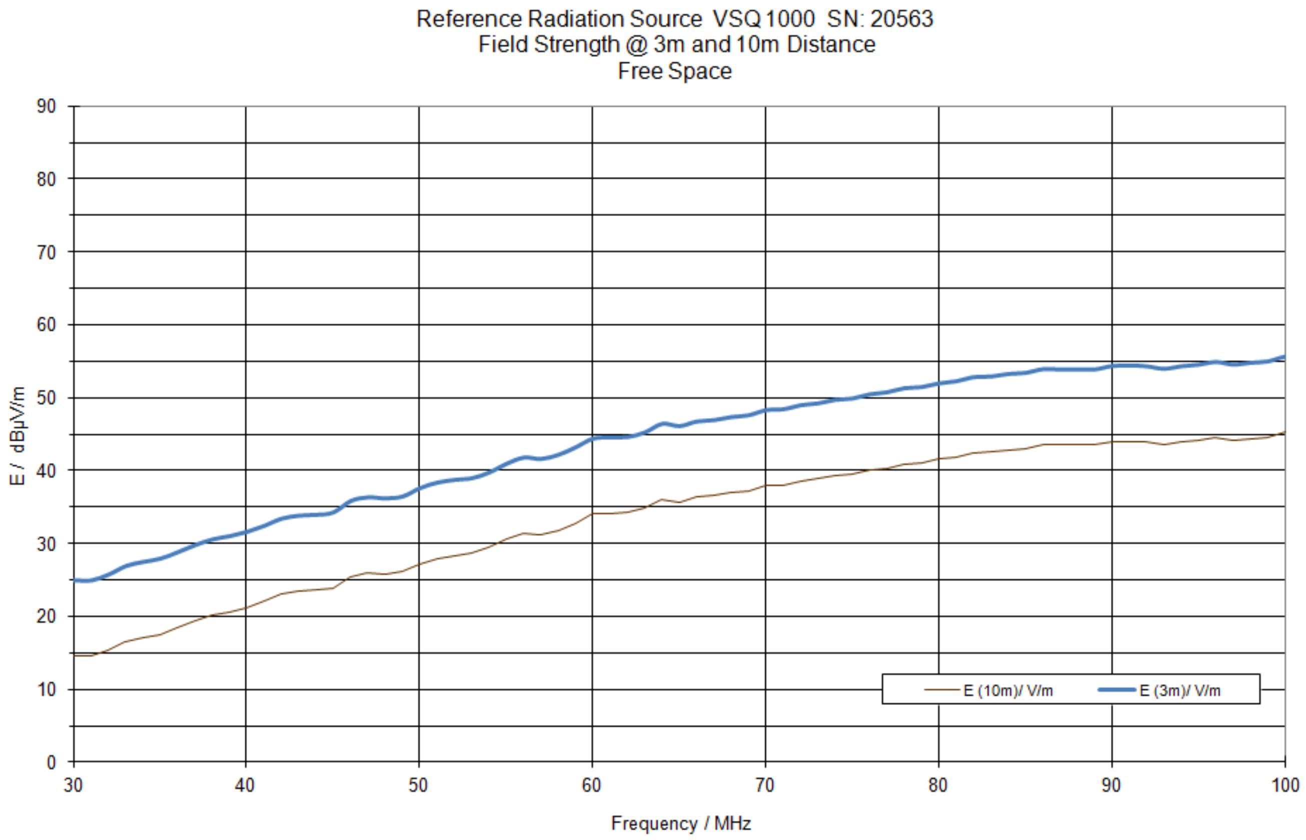

Frequency / MHz	E (3m) / dBµV/m	E (10m) / dBµV/m
30	25.0	14.6
31	25.0	14.6
32	25.8	15.4
33	27.0	16.6
34	27.6	17.1
35	28.0	17.6
36	28.9	18.4
37	29.9	19.4
38	30.7	20.2
39	31.1	20.6
40	31.7	21.2
41	32.5	22.1
42	33.5	23.0
43	33.9	23.5
44	34.0	23.6
45	34.4	23.9
46	35.9	25.5
47	36.4	26.0
48	36.3	25.8
49	36.5	26.1
50	37.7	27.2
51	38.4	28.0
52	38.8	28.4
53	39.0	28.6
54	39.8	29.4
55	41.0	30.6
56	41.9	31.4
57	41.7	31.2
58	42.2	31.8
59	43.3	32.8
60	44.5	34.0
61	44.6	34.2
62	44.7	34.2
63	45.3	34.9
64	46.5	36.0
65	46.2	35.7

Frequency / MHz	E (3m) / dBµV/m	E (10m) / dBµV/m
66	46.8	36.4
67	47.0	36.6
68	47.4	37.0
69	47.7	37.2
70	48.4	37.9
71	48.5	38.0
72	49.0	38.6
73	49.3	38.8
74	49.8	39.3
75	50.0	39.5
76	50.5	40.1
77	50.8	40.4
78	51.4	40.9
79	51.5	41.1
80	52.0	41.6
81	52.3	41.9
82	52.9	42.4
83	53.0	42.5
84	53.3	42.9
85	53.5	43.0
86	54.0	43.5
87	53.9	43.5
88	54.0	43.5
89	53.9	43.5
90	54.4	44.0
91	54.5	44.0
92	54.4	43.9
93	54.0	43.6
94	54.4	43.9
95	54.6	44.1
96	55.0	44.5
97	54.6	44.2
98	54.9	44.4
99	55.0	44.6
100	55.7	45.2
101	55.7	45.2

D Numerical solution for the energy thresholds and efficiency

D.1 Method

The model for the efficiency and thresholds of Tunka-Rex, developed in Sec. 6.4 was solved numerically to implement the non-idealized detector geometry. Therefore, a regular grid, with 5 m spacing in x and y direction, was superimposed on a map of the Tunka-Rex detector. The grid represents possible shower-core positions. In each point of the grid, the shower footprint of radio signal above threshold is described by the area of an ellipse with minor axes $a = r_{\mathrm{th}}$ (see Eq. 6.12) and major axes $b = r_{\mathrm{th}} \cdot \cos^{-1}\theta$, for zenith angle θ. The orientation of the ellipses is rotated according to the azimuth angle φ. With Eq. 6.12, r_{th} can be solved for the corresponding energy E_{th}. An antenna at the coordinates x_j, y_j, has the distance $\sqrt{\Delta x^2 + \Delta y^2}$ to a point x_i, y_i, with $\Delta x = x_j - x_i$ and $\Delta y = y_j - y_i$. Thus, all antennas located within the ellipse around x_i, y_i, fulfill the condition

$$\left(\frac{\Delta x \cdot \cos(\varphi) + \Delta y \cdot \sin(\varphi)}{r_{\mathrm{th}}}\right)^2 + \left(\frac{\Delta x \cdot \sin(\varphi) - \Delta y \cdot \cos(\varphi)}{r_{\mathrm{th}} \cos^{-1}\theta}\right)^2 < 1. \tag{D.1}$$

For the standard reconstruction, 3 antennas are required. Thus, the grid was scanned for different shower geometries, to determine for each shower geometry where in the array Eq. D.1 if fulfilled by at least 3 antennas . The scanned parameters were 25 to 300 m for r_{th}, 0° to 50° in 10° steps for the zenith angle θ and 10° to 360° for the azimuth angles φ.

First, the problem is analyzed from a purely geometric point of view: the efficiency in a point is defined as the fraction of scanned azimuth angles, at a given r_{th} and zenith angle, which fulfill the trigger condition (3 antennas above threshold). An example of an efficiency distribution is shown in Fig. D.1. The efficiency of the overall detector is defined as the mean of the efficiency of all points in the detector area.

With this calculation, it can be determined, when certain efficiency levels are reached. In Fig. D.2, the efficiency as a function of footprint area for different zenith angles is shown in Fig. D.2. For the inner array, within 350 m to the center, the regular hexagonal grid approximates the trigger behavior well: sensitivity starts around a footprint area of $1A_1$ and 90% efficiency is reached around $3A_1$. Including the borders however, i.e., allowing for core locations up to 500 m distance from the array center, a footprint area around $5A_1$ is required for 90% efficiency.

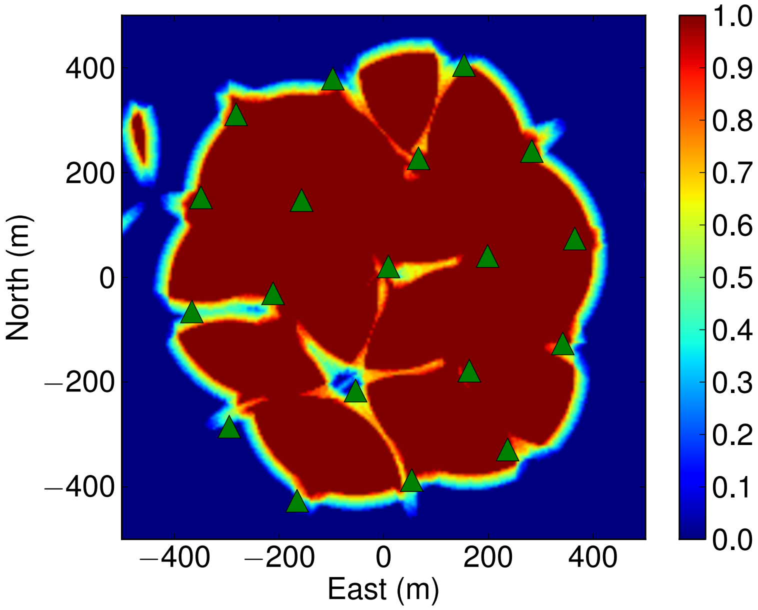

Figure D.1: Efficiency for a zenith angle of $\theta = 30^\circ$ and r_{th} =200 m, corresponding to an energy around $10^{17.5}$ eV (depending on azimuth angle). 3 antennas above threshold are required for a trigger. The small hot spot in the upper left is from the influence of a close outer antenna station in that direction.

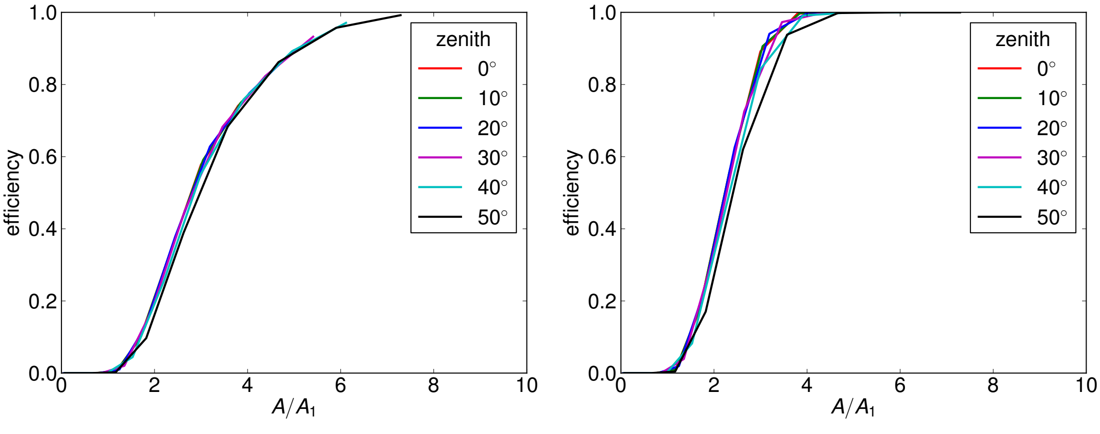

(a)

(b)

Figure D.2: The efficiency as a function of the shower footprint size for detection in at least 3 antennas. The area of the footprint is given in terms of unitary cells A_1 for (a) events on the full array up to 500 m and (b) up to 350 m from the array center. Inclined showers generally have a larger footprint and reach the respective efficiencies at lower energies.

In Sec. 6.4, the same calculations are used to determine, at which minimum energy for a given shower geometry the trigger conditions are fulfilled in at least one point anywhere in the array and in at least 90% of the array (within 500 m).

D.2 Alternative Tunka-Rex geometries

The calculations in Sec. 6.4 were made assuming the complete array of 2013. However, there were two antennas missing in the first season, only installed for the second season in 2013. To investigate the influence of the resulting holes in the array, the corresponding geometry is plugged into the calculation. In Fig. D.3, the energy thresholds for detection are shown. Over the full array, the holes increases the average energy threshold only marginally. The effect on the threshold energy is mainly localized around the holes, with thresholds rising around $\Delta \lg E_{\mathrm{th}}/eV = 0.2$ to 0.3 on average. Especially towards the borders, the increase of the threshold becomes significant, but can be easily avoided during analysis by applying cuts on the evaluated detector area.

In 2014, next to each of the 19 antennas of the central, dense detector another antenna was placed, together with the scintillator stations of Tunka-Grande. From November 2015 on, the scintillator extension triggers the whole array, extending its uptime significantly due to daytime measurements. This new, denser layout has been investigated as well. The results are shown in Fig. D.4. Since the additional antennas stand next to each other, effectively the trigger requirements were lowered, corresponding to a two-antenna trigger of the old layout. The minimum energy stays approximately the same, because the footprint sizes still have to be in the order of the antenna distances of 200 m. The energy thresholds for 90% efficiency are reduced by $\Delta \lg E_{\mathrm{th}}/eV = -0.3$, roughly a factor of 2, due to a reduced influence of irregularities in the array. Furthermore, the effective area reaches out further, especially increasing the sensitivity to far events, towards a distance of 500 m to the array center.

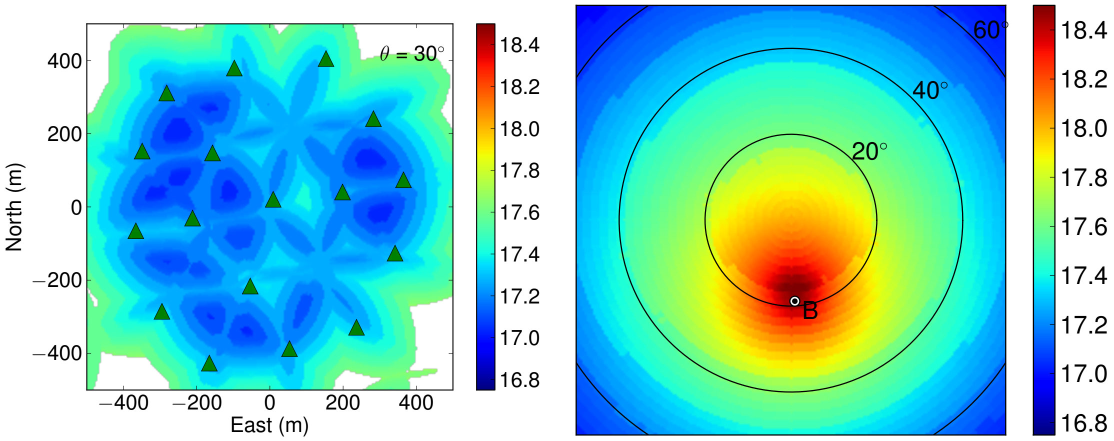

(a)

(b)

Figure D.3: Threshold energy for a 3 antenna trigger of the 2012 setup of Tunka-Rex, with 2 antennas missing in the array (a) for a zenith angle of 30° and random azimuth angle as a function of shower-core position, and (b) for 90% efficiency (within 500 m of the array center) with the standard cuts, as a function of the incoming direction.

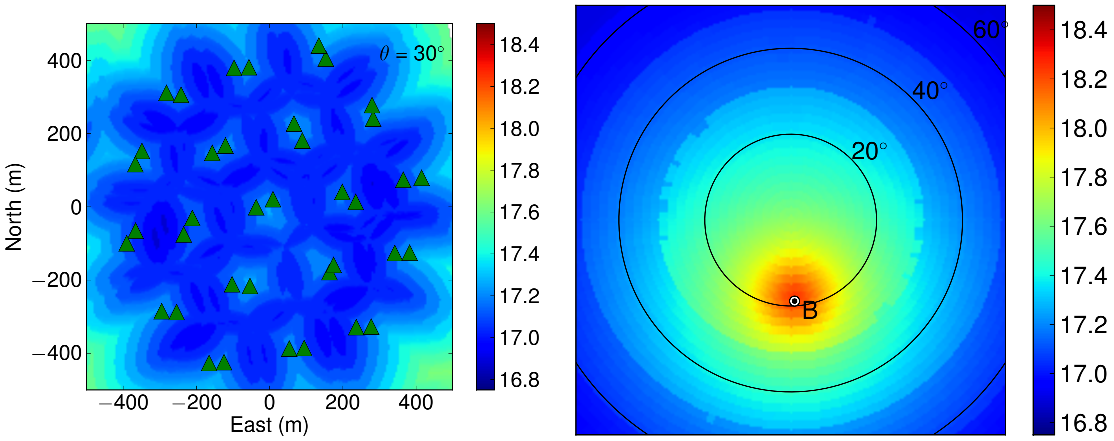

(a)

(b)

Figure D.4: Threshold energy of the 2015 setup of Tunka-Rex, with two antennas at each former cluster (a) for a zenith angle of 30° and random azimuth angle as a function of shower-core position, and (b) for 90% efficiency (within 500 m of the array center) with the standard cuts, as a function of the incoming direction.

Bibliography

[1] W. D. Apel et al. (LOPES Collaboration et al.). Improved absolute calibration of LOPES measurements and its impact on the comparison with REAS 3.11 and CoREAS simulations. *Astroparticle Physics*, 75:72–74, 2016, doi:10.1016/j.astropartphys.2015.09.002.

[2] A. Nelles et al. (LOFAR Collaboration et al.). Calibrating the absolute amplitude scale for air showers measured at LOFAR. *Journal of Instrumentation*, 10(11):P11005, 2015, doi:10.1088/1748-0221/10/11/P11005.

[3] V. F. Hess. Beobachtungen der durchdringenden Strahlung bei sieben Freiballonfahrten. *Phys. Z.*, 13:1084, 1912.

[4] P. Maestro. Cosmic rays: direct measurements. *Proceedings of Science*, (PoS(ICRC2015)016), 2015. Proceedings of the 34th ICRC, The Hague, The Netherlands.

[5] P. Auger, P. Ehrenfest, R. Maze, et al. Extensive Cosmic-Ray Showers. *Reviews of Modern Physics*, 11:288–291, 1939.

[6] J. Linsley. Evidence for a Primary Cosmic-Ray Particle with Energy 10^{20} eV. *Physical Review Letters*, 10(4):146–148, 1963, doi:10.1103/PhysRevLett.10.146.

[7] V. Verzi. Cosmic rays: air showers from low to high energies. *Proceedings of Science*, (PoS(ICRC2015)015), 2015. Proceedings of the 34th ICRC, The Hague, The Netherlands.

[8] V.V. Prosin et al. (Tunka-133 Collaboration). Tunka-133: Results of 3 year operation. *Nucl. Instr. and Meth. A*, 756:94–101, 2014, doi:10.1016/j.nima.2013.09.018.

[9] J. Abraham et al. (Pierre Auger Collaboration). Measurement of the energy spectrum of cosmic rays above 10^{18} eV using the Pierre Auger Observatory. *Phys. Lett.*, B685:239–246, 2010, doi:10.1016/j.physletb.2010.02.013.

[10] P. Tinyakov et al. (Telescope Array Collaboration). Latest results from the Telescope Array. *Nucl. Instr. and Meth. A*, 742:29–34, 2014, doi:10.1016/j.nima.2013.10.067.

[11] T. Antoni et al. (KASCADE Collaboration). KASCADE measurements of energy spectra for elemental groups of cosmic rays: Results and open problems. *Astroparticle Physics*, 24:1–25, 2005, doi:10.1016/j.astropartphys.2005.04.001.

[12] M. G. Aartsen, et al. (IceCube Collaboration). Measurement of the cosmic ray energy spectrum with IceTop-73. *Phys. Rev. D*, 88:042004, Aug 2013, doi:10.1103/PhysRevD.88.042004.

[13] W. D. Apel et al. (KASCADE-Grande Collaboration). Kneelike structure in the spectrum of the heavy component of cosmic rays observed with KASCADE-Grande. *Phys. Rev. Lett.*, 107:171104, 2011, doi:10.1103/PhysRevLett.107.171104.

[14] K. Greisen. End to the Cosmic-Ray Spectrum? *Physical Review Letters*, 16:748–750, 1966.

[15] G. T. Zatsepin and V. A. Kuzmin. Upper limit of the spectrum of cosmic rays. *ZhETF Pis ma Redaktsiiu*, 4(3):114–117, 1966.

[16] D. Allard, E. Parizot, A. V. Olinto, et al. UHE nuclei propagation and the interpretation of the ankle in the cosmic-ray spectrum. *Astronomy & Astrophysics*, 443(3):L29–L32, 2005, doi:10.1051/0004-6361:200500199.

[17] R. Engel. Relations between high-energy particle and cosmic-ray physics. *Proceedings of Science*, (PoS(ICRC2015)007), 2015. Proceedings of the 34th ICRC, The Hague, The Netherlands.

[18] J. Blümer, R. Engel, and J. R. Hörandel. Cosmic rays from the knee to the highest energies. *Progress in Particle and Nuclear Physics*, 63:293–338, 2009, doi:10.1016/j.ppnp.2009.05.002.

[19] Karl-Heinz Kampert and Michael Unger. Measurements of the Cosmic Ray Composition with Air Shower Experiments. *Astroparticle Physics*, 35:660–678, 2012, doi:10.1016/j.astropartphys.2012.02.004.

[20] V. V. Prosin et al. (Tunka-133 Collaboration). Primary CR energy spectrum and mass composition by the data of Tunka-133 array. *EPJ Web Conf.*, 99:04002, 2015, doi:10.1051/epjconf/20159904002.

[21] M. M. Shapiro and R. Silberberg. Lifetime of cosmic rays. *Acta Phys. Hung.*, 29S1:485–490, 1970.

[22] B. F. Rauch et al. - TIGER Collaboration. Cosmic Ray origin in OB Associations and Preferential Acceleration of Refractory Elements: Evidence from Abundances of Elements $_{26}$Fe through $_{34}$Se. *Astrophysical Journal*, 697:2083–2088, 2009, doi:10.1088/0004-637X/697/2/2083.

[23] W. D. Apel et al. (KASCADE-Grande Collaboration). Ankle-like Feature in the Energy Spectrum of Light Elements of Cosmic Rays Observed with KASCADE-Grande. *Phys. Rev.*, D87:081101, 2013, doi:10.1103/PhysRevD.87.081101.

[24] M. Unger. Report of the Working Group on the Composition of Ultra-High Energy Cosmic Rays. *Proceedings of Science*, (PoS(ICRC2015)307), 2015. Proceedings of the 34th ICRC, The Hague, The Netherlands.

[25] J. Abraham et al. (Pierre Auger Collaboration). Correlation of the highest energy cosmic rays with nearby extragalactic objects. *Science*, 318:938–943, 2007, doi:10.1126/science.1151124.

[26] E. Fermi. On the Origin of Cosmic Radiation. *Physical Review*, 75(8):1169, 1949.

[27] W. Axford et al. In *Proceedings of the 15th ICRC, Plovidv, Bulgaria*, volume 11, page 132, 1977.

[28] A. M. Hillas. The Origin of Ultra-High-Energy Cosmic Rays. *Annual Review of Astronomy and Astrophysics*, 22:425–444, 1984, doi:10.1146/annurev.aa.22.090184.002233.

[29] A. M. Hillas. Can diffusive shock acceleration in supernova remnants account for high-energy galactic cosmic rays? *J. Phys.*, G31:R95–R131, 2005, doi:10.1088/0954-3899/31/5/R02.

[30] D. Caprioli. Cosmic-ray acceleration and propagation. *Proceedings of Science*, (PoS(ICRC2015)008), 2015. Proceedings of the 34th ICRC, The Hague, The Netherlands.

[31] F. Aharonian et al. - H.E.S.S. Collaboration. Primary particle acceleration above 100 TeV in the shell-type supernova remnant RX J1713.7-3946h deep HESS observations. *Astronomy & Astrophysics*, 464(1):235–243, 2007, doi:10.1051/0004-6361:20066381.

[32] Ralph Engel, Dieter Heck, and Tanguy Pierog. Extensive air showers and hadronic interactions at high energy. *Annual Review of Nuclear and Particle Science*, 61(1):467–489, 2011, doi:10.1146/annurev.nucl.012809.104544.

[33] Lyndon Evans and Philip Bryant. LHC Machine. *Journal of Instrumentation*, 3:S08001, 2008, doi:10.1088/1748-0221/3/08/S08001.

[34] W. Heitler. *The Quantum Theory of Radiation.* Oxford University Press, Oxford, third ed. edition, 1954.

[35] J. Matthews. A Heitler model of extensive air showers. *Astroparticle Physics*, 22(5-6):387–397, January 2005.

[36] A. Aab et al. (Pierre Auger Collaboration). Muons in air showers at the Pierre Auger Observatory: Mean number in highly inclined events. *Phys. Rev.*, D91(3):032003, 2015, doi:10.1103/PhysRevD.91.059901, 10.1103/PhysRevD.91.032003.

[37] N. M. Budnev et al. TAIGA the Tunka Advanced Instrument for cosmic ray physics and Gamma Astronomy - present status and perspectives. *Journal of Instrumentation*, 9(09):C09021, 2014, doi:10.1088/1748-0221/9/09/C09021.

[38] W. D. Apel et al. (KASCADE-Grande Collaboration). The KASCADE-Grande experiment. *Nucl. Instr. and Meth. A*, 620:202–216, 2010, doi:10.1016/j.nima.2010.03.147.

[39] M. Amenomori et al. (Tibet ASγ Collaboration). Search for gamma rays above 100 TeV from the crab nebula with the TIBET air shower array and the 100 m^2 muon detector. *Astrophysical Journal*, 813(2):98, 2015, doi:10.1088/0004-637X/813/2/98.

[40] T. Abu-Zayyad et al. (Telescope Array Collaboration). The surface detector array of the Telescope Array experiment. *Nucl. Instr. and Meth. A*, 689:87–97, 2013, doi:10.1016/j.nima.2012.05.079.

[41] M. A. Lawrence, R. J. O. Reid, and A. A. Watson. The Cosmic ray energy spectrum above 4x10**17-eV as measured by the Haverah Park array. *J. Phys.*, G17:733–757, 1991, doi:10.1088/0954-3899/17/5/019.

[42] R. Abbasi et al. (IceCube Collaboration). IceTop: The surface component of IceCube. *Nucl. Instr. and Meth. A*, 700:188–220, 2013, doi:10.1016/j.nima.2012.10.067.

[43] J. Abraham et al. (Pierre Auger Collaboration). Trigger and aperture of the surface detector array of the Pierre Auger Observatory. *Nucl. Instr. and Meth. A*, 613:29–39, 2010, doi:10.1016/j.nima.2009.11.018.

[44] T. Antoni et al. (KASCADE Collaboration). The Cosmic ray experiment KASCADE. *Nucl. Instr. and Meth. A*, 513:490–510, 2003, doi:10.1016/S0168-9002(03)02076-X.

[45] J. Pretz. Highlights from the High Altitude Water Cherenkov Observatory. *Proceedings of Science*, (PoS(ICRC2015)025), 2015. Proceedings of the 34th ICRC, The Hague, The Netherlands.

[46] R. Abbasi et al. (IceCube Collaboration). Study of Ultra-High Energy Cosmic Ray composition using Telescope Array's Middle Drum detector and surface array in hybrid mode. *Astroparticle Physics*, 64:49–62, 2014, doi:10.1016/j.astropartphys.2014.11.004.

[47] P. Abreu et al. (Pierre Auger Collaboration). Measurement of the Cosmic Ray Energy Spectrum Using Hybrid Events of the Pierre Auger Observatory. *Eur. Phys. J. Plus*, 127:87, 2012, doi:10.1140/epjp/i2012-12087-9.

[48] J. Aleksic et al. (MAGIC Collaboration). Performance of the MAGIC stereo system obtained with Crab Nebula data. *Astroparticle Physics*, 35(7):435 – 448, 2012, doi:10.1016/j.astropartphys.2011.11.007.

[49] J. Bolmont et al. The camera of the fifth H.E.S.S. telescope. Part I: System description. *Nucl. Instr. and Meth. A*, 761:46–57, 2014, doi:10.1016/j.nima.2014.05.093.

[50] A. A. Ivanov, S. P. Knurenko, and I. Ye Sleptsov. Measuring extensive air showers with Cherenkov light detectors of the Yakutsk array: The energy spectrum of cosmic rays. *New J. Phys.*, 11:065008, 2009, doi:10.1088/1367-2630/11/6/065008.

[51] D. J. Bird (HiRes Collaboration). The Cosmic ray energy spectrum observed by the Fly's Eye. *Astrophysical Journal*, 424:491–502, 1994, doi:10.1086/173906.

[52] P. Sokolsky et al. (HiRes Collaboration). Observation of the GZK cutoff by the HiRes Experiment. *Nucl. Phys. B*, 196(0):67 – 73, 2009, doi:10.1016/j.nuclphysbps.2009.09.010.

[53] H. Tokuno et al. (Telescope Array Collaboration). New air fluorescence detectors employed in the Telescope Array experiment. *Nucl. Instr. and Meth. A*, 676:54–65, 2012, doi:10.1016/j.nima.2012.02.044.

[54] P. Necesal et al. (Pierre Auger Collaboration). The Fluorescence Detector of the Pierre Auger Observatory. *J. Phys. Conf. Ser.*, 293:012036, 2011, doi:10.1088/1742-6596/293/1/012036.

[55] J. H. Adams. Space experiment TUS on board the Lomonosov satellite as pathfinder of JEM-EUSO. *Exper. Astron.*, 40(1):315–326, 2015, doi:10.1007/s10686-015-9465-y.

[56] M. Casolino et al. (JEM-EUSO Collaboration). Detecting ultra-high energy cosmic rays from space with unprecedented acceptance: objectives and design of the JEM-EUSO mission. *Astrophysics and Space Sciences Transactions*, 7(4):477–482, 2011, doi:10.5194/astra-7-477-2011.

[57] H.R. Allan. Radio emission from extensive air showers. *Progress in Elementary Particle and Cosmic Ray Physics*, 10:171, 1971.

[58] F. D. Kahn and I. Lerche. Radiation from cosmic ray air showers. In *Proceedings of the Royal Society of London. Series A, Mathematical and Physical Sciences*, volume 289, page 206, 1966.

[59] G. A. Askaryan. Excess negative charge of an electron-photon shower and its coherent radio emission. *Soviet Physics JETP*, 14:441, 1962.

[60] J. V. Jelley, J. H. Fruin, N. A. Porter, et al. Radio Pulses from Extensive Cosmic-Ray Air Showers. *Nature*, 205:327–328, 1965, doi:10.1038/205327a0.

[61] Tim Huege. The renaissance of radio detection of cosmic rays. *Braz. J. Phys.*, 44:520–529, 2014, doi:10.1007/s13538-014-0226-6.

[62] H. Falcke et al. (LOPES Collaboration). Detection and imaging of atmospheric radio flashes from cosmic ray air showers. *Nature*, 435:313–316, 2005, doi:10.1038/nature03614.

[63] D. Ardouin, A. Bellétoile, and D. Charrier et al. Radio-detection signature of high-energy cosmic rays by the codalema experiment. *Nucl. Instr. and Meth. A*, 555(1–2):148 – 163, 2005, doi:10.1016/j.nima.2005.08.096.

[64] M. P. van Haarlem et al. (LOFAR Collaboration). LOFAR: The LOw-Frequency ARray. *Astronomy & Astrophysics*, 556:A2, August 2013, doi:10.1051/0004-6361/201220873.

[65] S. Fliescher for the Pierre Auger Collaboration. Radio detection of cosmic ray induced air showers at the Pierre Auger Observatory. *Nucl. Instr. and Meth. A*, 662(Supplement 1):S124 – S129, 2012, doi:10.1016/j.nima.2010.11.045. ARENA 2010.

[66] P. A. Bezyazeekov et al. (Tunka-Rex Collaboration). Measurement of cosmic-ray air showers with the Tunka Radio Extension (Tunka-Rex). *Nucl. Instr. and Meth. A*, 802:89 – 96, 2015, doi:10.1016/j.nima.2015.08.061.

[67] T. Huege. Theory and simulations of air shower radio emission. *AIP Conference Proceedings*, 1535:121, 2013, doi:10.1063/1.4807533.

[68] Clancy W. James, Heino Falcke, Tim Huege, and Marianne Ludwig. General description of electromagnetic radiation processes based on instantaneous charge acceleration in "endpoints". *Phys. Rev. E*, 84:056602, Nov 2011, doi:10.1103/PhysRevE.84.056602.

[69] Jaime Alvarez-Muniz, Washington R. Carvalho, Jr., and Enrique Zas. Monte Carlo simulations of radio pulses in atmospheric showers using ZHAireS. *Astroparticle Physics*, 35:325–341, 2012, doi:10.1016/j.astropartphys.2011.10.005.

[70] A. Nelles et al. (LOFAR Collaboration). Measuring a Cherenkov ring in the radio emission from air showers at 110–190 MHz with LOFAR. *Astroparticle Physics*, 65:11–21, 2014, doi:10.1016/j.astropartphys.2014.11.006.

[71] S. Hoover et al. (ANITA Collaboration). Observation of Ultra-high-energy Cosmic Rays with the ANITA Balloon-borne Radio Interferometer. *Phys. Rev. Lett.*, 105:151101, 2010, doi:10.1103/PhysRevLett.105.151101.

[72] R. Šmída et al. (CROME Collaboration). First Experimental Characterization of Microwave Emission from Cosmic Ray Air Showers. *Phys. Rev. Lett.*, 113(22):221101, 2014, doi:10.1103/PhysRevLett.113.221101.

[73] T. Huege, M. Ludwig, and C. W. James. Simulating radio emission from air showers with coreas. *AIP Conference Proceedings*, 1535(1):128–132, 2013, doi:10.1063/1.4807534.

[74] O. Scholten, K. Werner, and F. Rusydi. A Macroscopic Description of Coherent Geo-Magnetic Radiation from Cosmic Ray Air Showers. *Astroparticle Physics*, 29:94–103, 2008, doi:10.1016/j.astropartphys.2007.11.012.

[75] Klaus Werner, Krijn D. de Vries, and Olaf Scholten. A Realistic Treatment of Geomagnetic Cherenkov Radiation from Cosmic Ray Air Showers. *Astroparticle Physics*, 37:5–16, 2012, doi:10.1016/j.astropartphys.2012.07.007.

[76] Marianne Ludwig and Tim Huege. REAS3: Monte Carlo simulations of radio emission from cosmic ray air showers using an 'end-point' formalism. *Astroparticle Physics*, 34:438–446, 2011, doi:10.1016/j.astropartphys.2010.10.012.

[77] D. Heck, J. Knapp, J. N. Capdevielle, et al. CORSIKA: A Monte Carlo Code to Simulate Extensive Air Showers. FZKA Report 6019, Forschungszentrum Karlsruhe, 1998.

[78] W. D. Apel et al. (LOPES Collaboration). Comparing LOPES measurements of air-shower radio emission with REAS 3.11 and CoREAS simulations. *Astroparticle Physics*, 50-52:76–91, 2013, doi:10.1016/j.astropartphys.2013.09.003.

[79] Benjamin Lothar Fuchs. *The lateral distribution of radio signals from cosmic ray air showers.* PhD thesis, Karlsruhe Institute of Technology, 2012. http://digbib.ubka.uni-karlsruhe.de/volltexte/documents/2472780.

[80] ITU (International Telecommunication Union). Radio noise. Recommendation ITU-R P.372-12, ITU, Geneva, Switzerland, 2015.

[81] A. Aab et al. (Pierre Auger Collaboration). Probing the radio emission from air showers with polarization measurements. *Phys. Rev. D*, 89:052002, Mar 2014, doi:10.1103/PhysRevD.89.052002.

[82] P. Lautridou, O. Ravel, A. Rebai, and A. Lecacheux. Some possible interpretations from data of the codalema experiment. *AIP Conference Proceedings*, 1535(1):99–104, 2013, doi:10.1063/1.4807529.

[83] P. Schellart et al. (LOFAR Collaboration). Polarized radio emission from extensive air showers measured with LOFAR. *JCAP*, 1410(10):014, 2014, doi:10.1088/1475-7516/2014/10/014.

[84] W. D. Apel et al. (LOPES Collaboration). Reconstruction of the energy and depth of maximum of cosmic-ray air showers from LOPES radio measurements. *Phys.Rev.*, D90(6):062001, 2014, doi:10.1103/PhysRevD.90.062001.

[85] P. A. Bezyazeekov et al. (Tunka-Rex Collaboration). Radio measurements of the energy and depth of maximum of cosmic-ray air showers by Tunka-Rex. *JCAP*, 1601(01):052, 2016, doi:10.1088/1475-7516/2016/01/052.

[86] A. Aab et al. (Pierre Auger Collaboration). Energy Estimation of Cosmic Rays with the Engineering Radio Array of the Pierre Auger Observatory. *Submitted to: Phys. Rev. D*, 2015. arxiv:1508.04267.

[87] W. D. Apel et al. (LOPES Collaboration). Experimental evidence for the sensitivity of the air-shower radio signal to the longitudinal shower development. *Phys. Rev.*, D85:071101, 2012, doi:10.1103/PhysRevD.85.071101.

[88] F.G. Schröder, T. Asch, L. Bähren, et al. New method for the time calibration of an interferometric radio antenna array. *Nucl. Instr. and Meth. A*, 615(3):277 – 284, 2010, doi:10.1016/j.nima.2010.01.072.

[89] W. D. Apel et al. (LOPES Collaboration). The wavefront of the radio signal emitted by cosmic ray air showers. *JCAP*, 1409(09):025, 2014, doi:10.1088/1475-7516/2014/09/025.

[90] S. Thoudam et al. (LOFAR Collaboration). LORA: A scintillator array for LOFAR to measure extensive air showers. *Nucl. Instr. and Meth. A*, 767:339–346, 2014, doi:10.1016/j.nima.2014.08.021.

[91] A. Nelles et al. (LOFAR Collaboration). A parameterization for the radio emission of air showers as predicted by CoREAS simulations and applied to LOFAR measurements. *Astroparticle Physics*, 60:13–24, 2014, doi:10.1016/j.astropartphys.2014.05.001.

[92] A. Corstanje et al. (LOFAR Collaboration). The shape of the radio wavefront of extensive air showers as measured with LOFAR. *Astroparticle Physics*, 61:22–31, 2015, doi:10.1016/j.astropartphys.2014.06.001.

[93] P. Abreu et al. (Pierre Auger Collaboration). Antennas for the detection of radio emission pulses from cosmic-ray induced air showers at the pierre auger observatory. *Journal of Instrumentation*, 7(10):P10011, 2012.

[94] Qader Dorosti. personal communication.

[95] C. Rühle. *Entwicklung eines schnellen eingebetteten Systems zur Radiodetektion kosmischer Strahlung*. PhD thesis, Karlsruhe Institute of Technology, 2014. http://digbib.ubka.uni-karlsruhe.de/volltexte/documents/3050561.

[96] P. Abreu et al. (Pierre Auger Collaboration). Advanced functionality for radio analysis in the Offline software framework of the Pierre Auger Observatory. *Nucl. Instr. and Meth. A*, 635:92–102, 2011, doi:10.1016/j.nima.2011.01.049.

[97] N. Budnev et al. Tunka-25 Air Shower Cherenkov array: The main results . *Astroparticle Physics*, 50–52:18 – 25, 2013, doi:10.1016/j.astropartphys.2013.09.006.

[98] V. Prosin. personal communication.

[99] N. M. Budnev et al. Data acquisition system for the TUNKA-133 array. In *Astroparticle, particle and space physics, detectors and medical physics applications. Proceedings, 10th Conference, ICATPP 2007, Como, Italy, October 8-12, 2007*, pages 287–291, 2008.

[100] S. Epimakhov. *Exploring cosmic ray origins with ground-based EAS arrays Tunka and HiSCORE.* PhD thesis, University of Hamburg, 2015. https://www.physnet.uni-hamburg.de/services/biblio/dissertation/dissfbPhysik.

[101] E. E. Korosteleva, V. V. Prosin, L. A. Kuzmichev, and G. Navarra. Measurement of cosmic ray primary energy with the atmospheric Cherenkov light technique in extensive air showers. *Nucl.Phys.Proc.Suppl.*, 165:74–80, 2007, doi:10.1016/j.nuclphysbps.2006.11.012.

[102] M. Aglietta et al. (EAS-TOP Collaboration). UHE cosmic ray event reconstruction by the electromagnetic detector of EAS-TOP. *Nucl. Instr. and Meth. A*, 336:310–321, 1993, doi:10.1016/0168-9002(93)91115-4.

[103] T. Abu-Zayyad (HiRes and MIA Collaborations). Evidence for Changing of Cosmic Ray Composition between 10**17-eV and 10**18-eV from Multicomponent Measurements. *Phys. Rev. Lett.*, 84:4276–4279, 2000, doi:10.1103/PhysRevLett.84.4276.

[104] A. Aab et al. (Pierre Auger Collaboration). Depth of maximum of air-shower profiles at the Pierre Auger Observatory. II. Composition implications. *Phys. Rev.*, D90(12):122006, 2014, doi:10.1103/PhysRevD.90.122006.

[105] J. Oertlin. Radio Data Analysis of a Prototype Antenna at the Tunka-133 Experiment. Bachelor Thesis, Karlsruhe Institute of Technology, 2011.

[106] O. Krömer et al. (LOPES Collaboration). New Antenna for Radio Detection of UHECR. In *Proceedings of the 31st ICRC, Lódź, Poland*, number 1232, 2009. http://icrc2009.uni.lodz.pl/proc/html/.

[107] H. Nyquist. Certain Topics in Telegraph Transmission Theory. *American Institute of Electrical Engineers, Transactions of the*, 47(2):617 –644, 1928, doi:10.1109/T-AIEE.1928.5055024.

[108] F. G. Schröder et al. (Tunka-Rex Collaboration). The Tunka Radio Extension (Tunka-Rex): Radio Measurements of Cosmic Rays in Siberia (PISA 2015). In *13th Pisa Meeting on Advanced Detectors: Frontier Detectors for Frontier Physics La Biodola, Isola d'Elba, Livorno, Italy, May 24-30, 2015*, 2015. 10.1016/j.nima.2015.08.075.

[109] The Radio Offline Group (Pierre Auger Collaboration). The radio extension of Auger Offline. Auger internal note GAP-2010-056, 2010.

[110] Stefan Fliescher. *Antenna Devices and Measurement of Radio Emission from Cosmic Ray induced Air Showers at the Pierre Auger Observatory.* PhD thesis, Aachen, Tech. Hochsch., 2011. https://inspirehep.net/record/1388443/files/3998.pdf.

[111] http://www.kabelwissen.de/koaxialkabel/rg_213_u_rg213_coaxialcable-cable/, December 2015.

[112] Lord Rayleigh. On the law of reciprocity in diffuse reflection. *Phil. Mag. series 5*, 49:324–325, 1900.

[113] C.A. Balanis. *Antenna Theory: Analysis and Design.* John Wiley & Sons, Inc., Hoboken, New Jersey, 2005.

[114] J.D. Kraus. *Antennas.* McGraw-Hill, Inc., 1988.

[115] G. Burke and A. Poggio. Nec - numerical electromagnetics code for antennas and scattering. Technical report, Lawrence Livermore National Laboratory, Livermore U.S.A., 1977.

[116] S. Nehls, A. Hakenjos, M.J. Arts, et al. Amplitude calibration of a digital radio antenna array for measuring cosmic ray air showers. *Nucl. Instr. and Meth. A*, 589(3):350 – 361, 2008, doi:10.1016/j.nima.2008.02.092.

[117] Matteo Frigo and Steven G. Johnson. The fastest Fourier transform in the west. Technical Report MIT-LCS-TR-728, Massachusetts Institute of Technology, September 1997.

[118] http://rp5.ru/Weather_archive_in_Khayta_Irkutskaya, December 2015.

[119] F. G. Schröder et al. (LOPES Collaboration). On noise treatment in radio measurements of cosmic ray air showers. *Nucl. Instr. and Meth. A*, 662:S238–S241, 2012, doi:10.1016/j.nima.2010.11.009.

[120] D. Kostunin. *Reconstruction of air-shower parameters with a sparse radio array.* PhD thesis, Karlsruhe Institute of Technology, 2015.

[121] D. Ardouin et al. (CODALEMA Collaboration). Geomagnetic origin of the radio emission from cosmic ray induced air showers observed by CODALEMA. *Astroparticle Physics*, 31:192–200, 2009, doi:10.1016/j.astropartphys.2009.01.001.

[122] W. D. Apel et al. (LOPES Collaboration). LOPES-3D, an antenna array for full signal detection of air-shower radio emission. *Nucl. Instr. and Meth. A*, 696:100–109, 2012, doi:10.1016/j.nima.2012.08.082.

[123] M. Melissas and Pierre Auger Collaboration. Recent developments at the Auger Engineering Radio Array. In *American Institute of Physics Conference Series*, volume 1535 of *American Institute of Physics Conference Series*, pages 63–67, 2013.

[124] D. Kostunin, P. A. Bezyazeekov, R. Hiller, F. G. Schröder, V. Lenok, and E. Levinson. Reconstruction of air-shower parameters for large-scale radio detectors using the lateral distribution. *Astroparticle Physics*, 74:79–86, 2016, doi:10.1016/j.astropartphys.2015.10.004.

[125] D. Kostunin. personal communication.

[126] D. Kostunin et al. (Tunka-Rex Collaboration). The Tunka Radio Extension: reconstruction of energy and shower maximum of the first year data (ICRC 2015). *Proceedings of Science*, (PoS(ICRC2015)285), 2015. Proceedings of the 34th ICRC, The Hague, The Netherlands.

[127] Sergey Ostapchenko. Monte Carlo treatment of hadronic interactions in enhanced Pomeron scheme: I. QGSJET-II model. *Phys.Rev.*, D83:014018, 2011, doi:10.1103/PhysRevD.83.014018.

[128] T. Pierog, M.K. Alekseeva, Till Bergmann, V. Chernatkin, R. Engel, et al. First results of fast one-dimensional hybrid simulation of EAS using CONEX. *Nucl.Phys.Proc.Suppl.*, 151:159–162, 2006, doi:10.1016/j.nuclphysbps.2005.07.029.

[129] F.G. Schröder. personal communication.

[130] W. D. Apel et al. (KASCADE-Grande Collaboration). The spectrum of high-energy cosmic rays measured with KASCADE-Grande. *Astroparticle Physics*, 36:183–194, 2012, doi:10.1016/j.astropartphys.2012.05.023.

[131] F.G. Schröder et al. (LOPES Collaboration). New results of the digital radio interferometer lopes. *Proceedings of Science*, (PoS(ICRC2015)317), 2015. Proceedings of the 34th ICRC, The Hague, The Netherlands.

[132] S. Grebe and Pierre Auger Collaboration. Spectral index analysis of the data from the auger engineering radio array. *AIP Conference Proceedings*, 1535(1):73–77, 2013, doi:10.1063/1.4807524.

List of Abbreviations

ADC	analog-to-digital converter
ADF	amplitude distribution function
AERA	Auger Engineering Radio Array
Aires	Air-shower Extended Simulations
ANITA	Antarctic Impulsive Transient Antenna
CODALEMA	Cosmic ray Detection Array with Logarithmic Electromagnetic Antennas
CoREAS	CORSIKA-based Radio Emission from Air Showers
CORSIKA	Cosmic Ray Simulations for KASCADE
CROME	Cosmic-Ray Observation via Microwave Emission
DAQ	data acquisition
dB	decibel, logarithmic relative power, (+20 dB corresponds to a factor 10 in amplitude and factor 100 in power)
EVA	Electric fields, using a Variable index of refraction in Air shower simulations code
FFTW	Fastest Fourier Transform in the West
GPS	Global Positioning System
GZK	Greisen – Zatsepin – Kuzmin [cut-off]
HiSCORE	Hundred*i Square-km Cosmic Origin Explorer
IACT	Imaging atmosphere(air)-Cherenkov Telescope
JEM-EUSO	Japanese Experiment Module – Extreme Universe Space Observatory
KASCADE	Karlsruhe Shower Core and Array Detector
KIT	Karlsruhe Institute of Technology

LDF	lateral distribution function
LNA	low-noise amplifier
LOFAR	Low-Frequency Array
LOPES	LOFAR Prototype Station
LPDA	Logarithmic Periodic Dipole Antenna
MGMR	Macroscopic model of Geomagnetic Radiation
PMT	Photomultiplier tube
QGSJET	Quark-Gluon String JET [model]
REAS	Radio Emission from Air Showers
RFI	Radio Frequency Interference
rms	Root-mean-square
SALLA	Short aperiodic loaded loop (antenna)
SNR	signal-to-noise ratio
TAIGA	Tunka Advanced Instrument for cosmic-ray physics and Gamma Astronomy
Tunka-Rex	Tunka Radio Extension
UTC	Coordinated Universal Time
ZHAires	ZHS + Aires [model]
ZHS	Zas – Halzen – Stanev [model]

Acknowledgment

There are many people who I have to thank for making this work possible. I would like to take the opportunity to point some of them in the following paragraphs:

I would like to thank my referee, Prof. Johannes Blümer, for giving me the opportunity to work in his institute and Prof. Michael Feindt, for being my co-referee.

Frank Schröder, my supervisor, contributed to literally every aspect of this work and always took the time to help or give advice in all areas. His outstanding organizational skills and professional attitude were a decisive factor for the success of the Tunka-Rex.

Dmitriy Kostunin, who I shared an office with, became a good friend from the first minute of our time at Tunka-Rex. I want to thank him for the enjoyable time we had and the crazy discussions. He taught me that there is always two sides to every coin.

Andreas Haungs, the key scientist of Tunka-Rex, always kept his bright attitude. He helped with political decision, and found solutions to impossible problems. Also, he tirelessly read through my thesis more than once, even during vacation.

Federico Bocci came to KIT to perform the calibration measurements of Tunka-Rex for his bachelor degree. He was an interested, hard-working student, and his careful work was basis for the success of the calibration campaign.

Tunka-Rex were not possible without the help of my Russian colleagues: Nicolai Budnev supported my stays in Russia and welcomed me warm-hearted from the start of Tunka-Rex. Nothing connected to Tunka-133 can be done without Leonid Kuzmichev, who always supported Tunka-Rex. Together with Alexander Pahorukov and Roman Monkhoev they took great care for me during my measurement shift. The Tunka-133 reconstruction was kindly provided for Tunka-Rex by Vasily Prosin. For the most part, Tunka-Rex were not operational without Rashid Mirgazov and Yulia Kazarina taking care for maintenance. They spared no effort to make my stay in Russia pleasant.

Furthermore, I want to thank all my other colleagues from the cosmic-ray group of KIT who made the work very enjoyable and contributed each in their way. David Schmidt spell-checked part of this thesis. The people from the SD floor were always up to interesting discussions, riddles or simply coffee.

Last but not least, I want to thank my family, for its invaluable support: My parents took great care of my daughter during my working hours. Judith Engelhardt had to sacrifice a lot so I could work unhindered. Special thanks go to our daughter Lia, for coming by from time to time and brighten up my mood during the final spurt of work.